

HEAT TRANSFER DISTRIBUTIONS ON THE WALLS OF A NARROW CHANNEL WITH
JET IMPINGEMENT AND CROSS FLOW

by

Osama M. A. Al-aqal

BS, King Abdulaziz University, 1991

MS, University of Pittsburgh, 1999

Submitted to the Graduate Faculty of
the School of Engineering in partial fulfillment
of the requirements for the degree of
Doctor of Philosophy

University of Pittsburgh

2003

UNIVERSITY OF PITTSBURGH

SCHOOL OF ENGINEERING

This dissertation was presented

by

Osama M. A Al-aqal

It was defended on

July 17, 2003

and approved by

Peyman Givi, William Kepler Whiteford Professor, Department of Mechanical Engineering

Laura Schaefer, Assistant Professor, Department of Mechanical Engineering

James L. Chen, Associate Professor, Mechanical Engineering

Dissertation Director: Minking K. Chyu, Leighton Orr Professor, Department of Mechanical Engineering

ABSTRACT

HEAT TRANSFER DISTRIBUTIONS ON THE WALLS OF A NARROW CHANNEL WITH JET IMPINGEMENT AND CROSS FLOW

Osama M. A. Al-aqal, Ph.D.

University of Pittsburgh, 2003

This study investigated the effect of the size of the jets, the number of jets, and jet-to-target plate spacing for the jet-issuing plate and target plate in the presence of a cross flow originating from upstream jets on the heat transfer distribution of the jet and target plates.

Two-dimensional inline arrays of circular jets of air impinging on a heat transfer surface parallel to the jet-issuing plate were considered. The air, after impingement, was constrained to exit in a single direction along a channel formed by the target plate and the jet-issuing plate. The downstream jets were subjected to a cross flow from the upstream jets. Jet distribution was tested according to 3 sets of criteria: 6 rows with 1 hole in each row, 12 rows with 2 holes in each row, and 18 rows with 3 holes in each row. The jet-to-jet spacing for all jet plates was 4 holes in diameter in the spanwise direction and 6.5 holes in diameter in the streamwise direction. Tests were conducted at a Reynolds number between 5,000 and 33,000. The heat transfer measurement used a liquid crystal imaging technique with a 1-dimensional transient conduction model.

ACKNOWLEDGEMENT

First, I would like to express my sincere gratitude and thanks to ALLAH for his guidance throughout this work and for all the blessings he has bestowed upon me.

This study would not have been done without the help of ALLAH, then many people. I would like to express my appreciation to my advisor Dr. Minking Chyu, who oversaw this work from the beginning to the final steps; to Dr. James Chen, Dr. Laura Schaefer, and Dr. Givi, members of my dissertation committee, for their constructive recommendations and encouragement, and to my wife, Tahany for her patience and support as I completed my study.

I also, would like to express my thanks to my mother, father, brothers and sister for their help and caring attitudes.

DEDICATION

This work is dedicated to my mother and father, and my wife Tahany, and children Ghada, Madawi, Mohammad, and Abdulmalik , who supported me with their love, care and prayers.

TABLE OF CONTENTS

	Page
ABSTRACT.....	iii
ACKNOWLEDGEMENT	iv
LIST OF TABLES	ix
LIST OF FIGURES	x
1.0 INTRODUCTION	1
1.1 Impingement Jet.....	2
1.1.1 Configurations of Impinging Jets.....	2
1.1.2 Characteristic Zones in the Impinging Jet	4
1.2 Impingement with Cross-Flow	6
1.3 Problem Statement.....	8
1.4 Objectives	8
1.5 Current Investigation	9
2.0 LITERATURE REVIEW	10
2.1 Introduction.....	10
2.2 Prior Studies.....	11
2.3 Impingement with Cross-Flow	13
2.4 Review of Some Patent Applications	14
2.4.1 Cooling of Gas Turbine Engines.....	14

2.4.2	Cooling of Combustion Chamber and Related Patent	16
2.4.3	Cooling of Turbine Blades and Related Patent.....	16
2.4.4	Heat Exchangers Employing Impinging Jets	17
3.0	THERMOCHROMIC LIQUID CRYSTAL	20
3.1	Introduction.....	20
3.2	Liquid Crystals Background	20
3.3	Properties of TLCs.....	25
3.4	Calibration of TLC.....	28
3.4.1	Experimental Apparatus.....	29
3.4.2	Decomposition of Color.....	31
4.0	HEAT TRANSFER MEASUREMENT USING TLC	35
4.1	Introduction.....	35
4.2	Steady State Liquid Crystal Method	36
4.2	Transient Liquid Crystal Method.....	39
4.3	Comparison Between Steady State and Transient Liquid Crystal Method.....	43
5.0	DESCRIPTION OF EXPERIMENT	46
5.1	Preparation of Test Section.....	46
5.2	Experimental Setup.....	47
5.4	Test Procedure	55
5.5	Data Reduction.....	56
5.6	System Uncertainty Analysis.....	58
6.0	RESULTS AND DISCUSSION	61
6.1	Detailed Local Heat Transfer Coefficient.....	61

6.2 Span-Averaged Nusselt Number Distribution	63
6.3 Overall-Averaged Nusselt Number.....	84
6.4 Row-Resolved Heat Transfer.....	91
6.5 Effect of Number of Holes and Jet-to-Target Spacing	103
7.0 CONCLUSION AND RECOMMENDATIONS	108
7.1 Summary of Thesis Research.....	108
7.2 Future Recommendations	110
BIBLIOGRAPHY.....	113

LIST OF TABLES

	Page
Table 6.1 <i>Comparison of Different Jet-to-Target Spacing for 6-Hole Jet and Target Plate.....</i>	104
Table 6.2 <i>Comparison of Different Jet-to-Target Spacing for 24-Hole Jet and Target</i>	104
Table 6.3 <i>Comparison of Different Jet-to-Target Spacing for 54-Holes Jet and Target</i>	104
Table 6.4 <i>Correlation Equations for 6-Hole Jet and Target Plates</i>	106
Table 6.5 <i>Correlation Equations for 24-Hole Jet and Target Plates</i>	107
Table 6.6 <i>Correlation Equations for 54-Hole Jet and Target Plates</i>	107

LIST OF FIGURES

	Page
Figure 1.1 An impingement jet.....	2
Figure 1.2 a: submerged jet; b: free impinging jet.....	3
Figure 1.3 a: unconfined impinging jet; b: confined impinging jet.....	4
Figure 1.4 Characteristic zones in impinging jets.....	4
Figure 1.5 Areas of influence for the impingement jet array.....	7
Figure 2.1 Cooling in gas turbine engine (Source: Vejrazka, 2002).....	15
Figure 2.2 Cooling of combustion chamber: a-with film cooling, b-without film cooling.....	15
Figure 2.3. Turbine vanes with internal cooling by impinging jets.....	17
Figure 2.4 a- Arrangement of furnace recuperator, b- Heat exchanger with impingement on fins.....	18
Figure 2.5 Heat exchanger module with stacked plate design (CHIC module). U.S. Patent.	19
Figure 2.6 a- CHIC module and OSF module, b- Two CHIC modules. U.S. Patent.	19
Figure 3.1 Molecular structures of TLC.....	24
Figure 3.2 Schematic of the nematic liquid crystal.....	25
Figure 3.3 Calibration test rig.....	29
Figure 3.4 Green intensity vs. temperature of TLC.....	34
Figure 4.1 Schematic of steady state method.....	36
Figure 4.2 Schematic of Transient Liquid Crystal Method.....	39
Figure 5.1 Typical test section in liquid crystal method.....	46

Figure 5.2. Experimental setup of liquid crystal method.....	48
Figure 5.3 Schematic of the test section.	49
Figure 5.4 Schematic of a top view and side view of the test channel.	51
Figure 5.5 Test section of the jet-issuing plate for 54 holes (all dimensions in cm).	52
Figure 5.6 Test Section of the Jet-issuing Plate for 24 holes (all dimensions in cm).	53
Figure 5.7 Test section of the jet-issuing plate for 6 holes (all dimensions in cm).	54
Figure 5.8 Flowchart of data reduction procedure.....	57
Figure 6.1 Local heat transfer coefficient for target plate with 6 hole and $H/D_j = 1.33$	65
Figure 6.2 Span-averaged Nusselt number for target plate with 6 hole and $H/D_j = 1.33$	66
Figure 6.3 Local heat transfer coefficient for target plate with 6 hole and $H/D_j = 2$	66
Figure 6.4. Span-averaged Nusselt number for target plate with 6hole and $H/D_j = 2$	67
Figure 6.5 Local heat transfer coefficient for target plate with 6 hole and $H/D_j = 2.67$	67
Figure 6.6 Span-averaged Nusselt number for target plate with 6 hole and $H/D_j = 2.67$	68
Figure 6.7 Local heat transfer coefficient for target plate with 24 hole and $H/D_j = 2.67$	68
Figure 6.8 Span-averaged Nusselt number for target plate with 24 hole and $H/D_j = 2.67$	69
Figure 6.9 Local heat transfer coefficient for target plate with 24 hole and $H/D_j = 4$	69
Figure 6.10 Span-averaged Nusselt number for target plate with 24 hole and $H/D_j = 4$	70
Figure 6.11 Local heat transfer coefficient for target plate with 24 hole and $H/D_j = 5.33$	70
Figure 6.12 Span-averaged Nusselt number for target plate with 24 hole and $H/D_j = 5.33$	71
Figure 6.13 Local heat transfer coefficient for target plate with 54 hole and $H/D_j = 4$	71
Figure 6.14 Span-averaged Nusselt number for target plate with 54 hole and $H/D_j = 4$	72
Figure 6.15 Local heat transfer coefficient for target plate with 54 hole and $H/D_j = 6$	72
Figure 6.16 Span-averaged Nusselt number for target plate with 54 hole and $H/D_j = 6$	73

Figure 6.17 Local heat transfer coefficient for target plate with 54 hole and $H/D_j = 8$	73
Figure 6.18 Span-averaged Nusselt number for target plate with 54 hole and $H/D_j = 8$	74
Figure 6.19 Local heat transfer coefficient for jet plate with 6 hole and $H/D_j = 1.33$	74
Figure 6.20 Span-averaged Nusselt number for jet plate with 6 hole and $H/D_j = 1.33$	75
Figure 6.21 Local heat transfer coefficient for jet-issuing plate with 6 hole and $H/D_j = 2$	75
Figure 6.22 Span-averaged Nusselt number for jet-issuing plate with 6 hole and $H/D_j = 2$	76
Figure 6.23 Local heat transfer coefficient for jet plate with 6 hole and $H/D_j = 2.67$	76
Figure 6.24 Span-averaged Nusselt number for jet plate with 6 hole and $H/D_j = 2.67$	77
Figure 6.25 Local heat transfer coefficient for jet plate with 24 hole and $H/D_j = 2.67$	77
Figure 6.26 Span-averaged Nusselt number for jet plate with 24 hole and $H/D_j = 2.67$	78
Figure 6.27 Local heat transfer coefficient for jet-issuing plate with 24 hole and $H/D_j = 4$	78
Figure 6.28 Span-averaged Nusselt number for jet plate with 24 hole and $H/D_j = 4$	79
Figure 6.29 Local heat transfer coefficient for jet plate with 24 hole and $H/D_j = 5.33$	79
Figure 6.30 Span-averaged Nusselt number for jet plate with 24 hole and $H/D_j = 5.33$	80
Figure 6.31 Local heat transfer coefficient for jet-issuing plate with 54 hole and $H/D_j = 4$	80
Figure 6.32 Span-averaged Nusselt number for jet plate with 54 hole and $H/D_j = 4$	81
Figure 6.33 Local heat transfer coefficient for jet-issuing plate with 54 hole and $H/D_j = 6$	81
Figure 6.34 Span-averaged Nusselt number for jet plate with 54 hole and $H/D_j = 6$	82
Figure 6.35 Local heat transfer coefficient for jet-issuing plate with 54 hole and $H/D_j = 8$	82
Figure 6.36 Span-averaged Nusselt number for jet plate with 54 hole and $H/D_j = 8$	83
Figure 6.37 Overall-averaged Nusselt number for 24-hole target plate.	83
Figure 6.38 Heat transfer enhancement over developed flow in channel.	85
Figure 6.39 Heat transfer enhancement over developed flow for 6-hole target plate.	88

Figure 6.40 Heat transfer enhancement over developed flow for 24-hole target plate.....	89
Figure 6.41 Heat transfer enhancement over developed flow for 54-hole target plate.....	89
Figure 6.42 Heat transfer enhancement over developed flow for 6-hole jet-issuing plate.	90
Figure 6.43 Heat transfer enhancement over developed flow for 24-hole jet-issuing plate.	90
Figure 6.44 Heat transfer enhancement over developed flow for 54-hole jet-issuing plate.	91
Figure 6.45 Schematic of rows in 54-hole jet-issuing plate.....	92
Figure 6.46 Row-resolved overall heat transfer for 6-hole jet plate with $H/D_j = 1.33$	93
Figure 6.47 Row-resolved overall heat transfer for 6-hole jet plate with $H/D_j = 2$	93
Figure 6.48 Row-resolved overall heat transfer for 6-hole jet plate with $H/D_j = 2.67$	94
Figure 6.49 Row-resolved overall heat transfer for 24-hole jet plate with $H/D_j = 2.67$	94
Figure 6.50. Row-resolved overall heat transfer for 24-hole jet plate with $H/D_j = 4$	95
Figure 6.51 Row-resolved overall heat transfer for 24-hole jet plate with $H/D_j = 5.33$	95
Figure 6.52 Row-resolved overall heat transfer for 54-hole jet plate with $H/D_j = 4$	96
Figure 6.53 Row-resolved overall heat transfer for 54-hole jet plate with $H/D_j = 6$	96
Figure 6.54 Row-resolved overall heat transfer for 54-hole jet plate with $H/D_j = 8$	97
Figure 6.55 Row-resolved overall heat transfer for 6-hole target plate with $H/D_j = 1.33$	97
Figure 6.56 Row-resolved overall heat transfer for 6-hole target plate with $H/D_j = 2$	98
Figure 6.57 Row-resolved overall heat transfer for 6-hole target plate with $H/D_j = 2.67$	98
Figure 6.58 Row-resolved overall heat transfer for 24-hole target plate with $H/D_j = 2.67$	99
Figure 6.59 Row-resolved overall heat transfer for 24-hole target plate with $H/D_j = 4$	99
Figure 6.60 Row-resolved overall heat transfer for 24-hole target plate with $H/D_j = 5.33$	100
Figure 6.61 Row-resolved overall heat transfer for 54-hole target plate with $H/D_j = 4$	100
Figure 6.62 Row-resolved overall heat transfer for 54-hole target plate with $H/D_j = 6$	101

Figure 6.63 Row-resolved overall heat transfer for 54-hole target plate with $H/D_j = 8$ 101

NOMENCLATURE

<u>Symbol</u>	<u>Explanation</u>
A	Cross-section area of test section channel , m ²
A _j	Area of impingement jet hole, m ²
D _j	Impingement jet hole diameter, m
D _h	Hydraulic diameter of the channel, m
h	Local convection heat transfer coefficient, W/m ² -K
H	Jet-to-target plate spacing, m
K	Thermal conductivity of acrylic material, W/m-K
k _{air}	Thermal conductivity of air, W/m-K
<i>m</i>	mass flow rate, g/s
Nu	Nusselt number, $h D_h / k_{air}$
Nu ₀	Fully developed Nusselt number based on the channel hydraulic diameter
n	Number of holes
Pr	Prandtl number
Re _j	Average jet Reynolds number, $\rho V_j D_j / \mu$
Re ₀	Average channel Reynolds number, $\rho \bar{u} D_h / \mu$
Rem	$Re \times (n D_j) / W$
S _x	Stream wise jet-jet spacing, m
S _y	Span wise jet-jet spacing, m
T _i	Initial temperature of test section, °C
T _m	Mainstream temperature of the flow, °C
T _w	Color change temperature of the liquid crystal, red-to-green, °C
T	Time of liquid crystal color change, sec
V _j	Average jet velocity, m/s
\bar{u}	Average channel velocity, m/s
W	Width of the channel, m
X	Axial distance of the impingement surface, m
Y	Span wise distance of the impingement surface, m
Z	Distance between jet plate and target plate, m
Greek Symbols	
α	Thermal diffusivity of acrylic material, m ² /s and also jet inclination Angle (degree)
μ	Fluid dynamic viscosity, pa.s
τ	Time step, sec
Subscript	
i	Initial
j	Jet or index of time step
m	Mainstream
o	Reference
w	Wall

1.0 INTRODUCTION

The use of impingement jets for the cooling of various regions of modern gas turbines is widespread, most especially within the high pressure turbine. Since the cooling effectiveness of impingement jets is very high, this method of cooling provides an efficient means of component heat load management and gives sufficient available pressure head and geometrical space for implementation. Regular arrays of impingement jets are used within turbine airfoils and endwalls to provide relatively uniform and controlled cooling of fairly open internal surface regions. Such regular impingement arrays are generally directed against the target surfaces by the use of sheet metal baffle plates, inserts, or covers that are fixed in position relative to the target surface. These arrangements allow for the design of a wide range of impingement geometries, including in-line, staggered, or arbitrary patterns of jets. In more confined regions of airfoils such as the leading edge or trailing edge, spanwise lines of impingement jets are sometimes used to focus cooling on one primary location of high external heat load like the airfoil's stagnation region. In these cases, impingement jets may be delivered by orifices that have been cast or machined into the internal structural members of the airfoil. There also exist many other applications for individual impingement jets on selected stationary and rotating surfaces. Vane endwalls, blade platforms, and unattached shrouds may all have specific local cooling requirements well suited to the use of individual jet cooling. Impingement jets are also used on rotor disk cavity faces, and in some applications, may provide additional functions of sealing. The use of impingement cooling is not

confined to the turbine components, however, as combustor components such as liners, transition pieces, and splash plates also make good use of both individual and array impingement cooling.

1.1 Impingement Jet

The impinging jet can be defined as a high-velocity coolant mass ejected from a hole or slot that impinges on the heat transfer surface (Fig. 1.1). A characteristic feature of this flow arrangement is an intensive heat transfer rate between the wall and the fluid. It predetermines the fluid jets to be widely used in industrial applications where intensive heat transfer rates are needed, for example for cooling of turbine blades, laser mirrors and electronic components, for paper drying, and so forth.

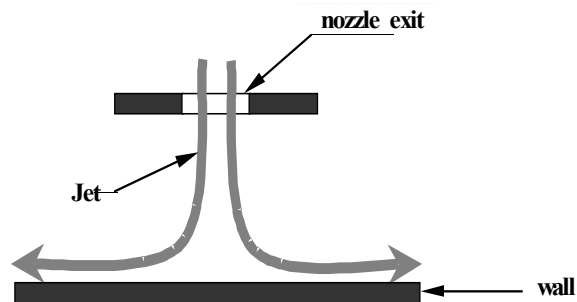


Figure 1.1 An impingement jet.

1.1.1 Configurations of Impinging Jets

We can distinguish two qualitatively different flow configurations: submerged impinging jets and free impinging jets (Fig. 1.2). In the former case, the fluid issuing from the nozzle is of the same nature as the surrounding. In the latter case, the fluids are of a different nature (e.g., a water jet issuing in air). The dynamics of both cases are different. In submerged jets, a shear layer forms at the

interface between the jet and the surrounding fluid. This shear layer is unstable and it generates turbulence. In free jets, this kind of instability is usually not important, and the turbulent motion in the shear layer does not have a substantial effect on the flow.

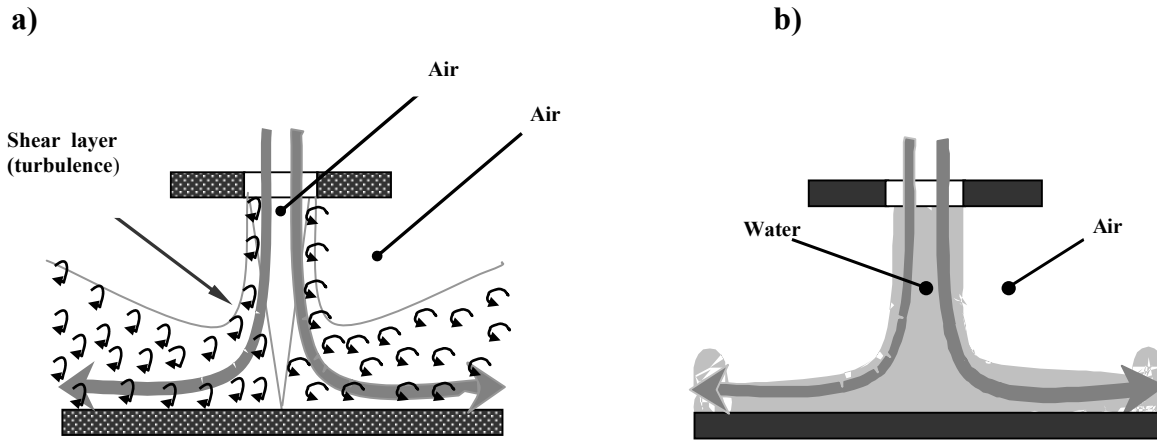


Figure 1.2 a: submerged jet; b: free impinging jet.

In terms of geometry, there are two cases: a planar case with the jet issuing from a slot, and an axisymmetric case with a round nozzle. The dynamics of both cases are different: round jets exhibit formation of axisymmetric vortex rings, which are stretched during their convection along the wall. In plane jets, the vortices are formed as filaments parallel to the slot. They are created on both sides of the jet, either in symmetric or antisymmetric mode. These vortex filaments are not stretched. Many others geometries are also possible--jets issuing from square, rectangular, or elliptical nozzles; oblique jets; and others.

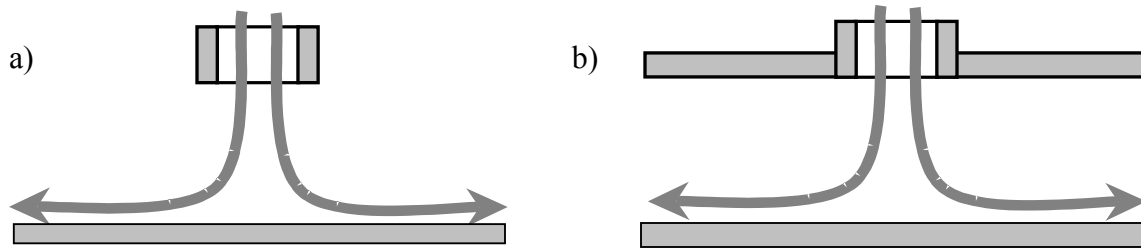


Figure 1.3 a: unconfined impinging jet; b: confined impinging jet

There is a further distinction between unconfined and confined jets (Fig.1.3). Confinement, which is common in industrial applications, causes flow recalculation around the jet. In industrial applications, the cooled surfaces are usually large, and a single jet is usually not sufficient for cooling it. In this case, an array of jets is used. The flow in arrays is rather complex.

1.1.2 Characteristic Zones in the Impinging Jet

The flow field in an impinging jet can be divided into three characteristic regions (Fig.1.4): the jet zone, the stagnation zone, and the wall jet zone.

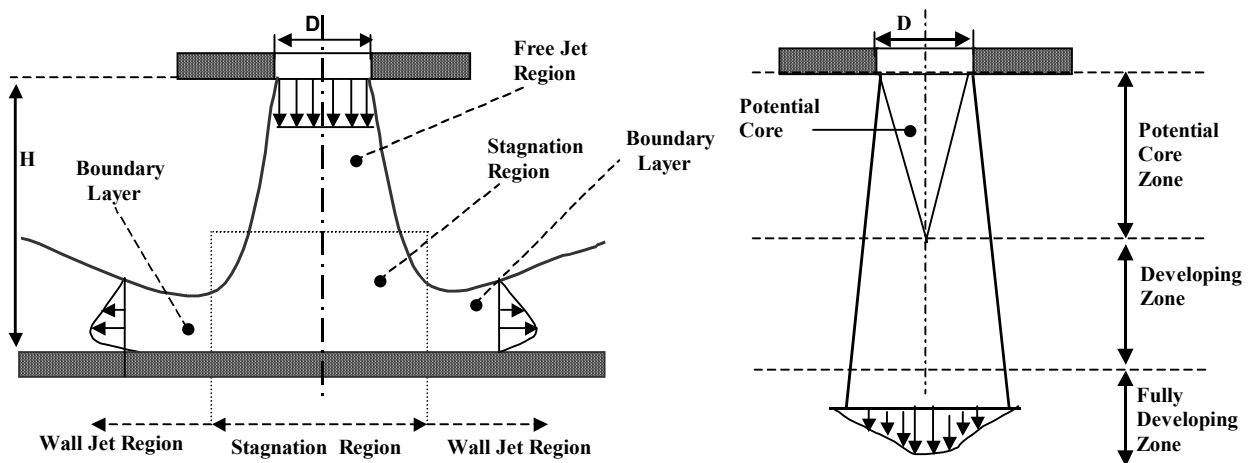


Figure 1.4 Characteristic zones in impinging jets.

The jet zone is situated directly beneath the nozzle. The fluid issuing from the nozzle mixes with the quiescent surrounding fluid and creates a flow field, which is up to a certain distance from the wall identical with the flow field of a submerged nonimpinging jet. The jet flow is undeveloped up to six or seven nozzle diameters from the nozzle lip. Consequently, in most applications, the nozzle-to-plate distance is too small to enable the developed jet flow condition. A shear layer forms around the jet. Its properties depend strongly on the nozzle type. In most situations, except a laminar flow from a tube nozzle, the shear layer is initially relatively thin compared to the nozzle diameter, and therefore its dynamical behavior is similar to that of a plane shear layer. The shear layer thickness becomes comparable with the jet diameter downstream, and the behavior of the layer changes considerably.

The flow issuing from the nozzle is either laminar or turbulent, depending on the nozzle type and the Reynolds number. The initial laminar flow undergoes a turbulent transition. The transition begins in the shear layer, which is unstable. The roll-up of vortices is the first stage of this transition if the jet Reynolds number is moderate. The vortices are convected downstream by the flow and they grow, pair, lose symmetry, and finally break up in eddies. Finally, a turbulent flow is developed. In many practical situations, the nozzle-to-plate spacing is small and the jet is still in a transitional state when it impinges on the wall.

If the velocity profile in the nozzle exit is flat enough, there is a potential core in the center of the jet. The potential core is the flow region, in which the mean velocity is still the same as in the nozzle exit. At that point, the fluid inside the core has not yet transferred its momentum to the surroundings. However, the instantaneous velocity is not constant in the core. The flow is pulsating

due to the velocity induction from the vortices passing in the shear layer. The potential core flow has an inviscid character.

Near the stagnation point, there is a stagnation zone. It is characterized by pressure gradient, which stops the flow in the axial direction and turns it radially outward. The pressure gradient also relaminarizes the flow on its arrival to the stagnation region. The boundary layer around the stagnation point is laminar because of the favorable pressure gradient. The increase of the velocity along the wall keeps the boundary layer thin, and consequently, the heat transfer rates are high.

The wall jet zone is free of gradients of the mean pressure. The flow decelerates and spreads here. The initially laminar boundary layer undergoes a turbulent transition that is induced by the impingement of large eddies created in the jet shear layer. This turbulent transition is believed to increase locally, and the heat transfer rate diminishes progressively.

1.2 Impingement with Cross-Flow

The flow in the impingement channel (i.e., the space enclosing the jet-issuing and impingement plate), differentiates the performance of multiple jets from single jets. The cross-flow in an impingement channel is developed for the most part by the spent jets. This flow is perpendicular to the bulk flow direction of a jet and is therefore called cross-flow. The cross-flow tries to deflect a jet away from its impinging location. If the cross-flow is strong and the jet is sufficiently far from the impingement plate, the cross-flow can deflect the jet away from the impingement surface, thus reducing the effectiveness of the impingement cooling.

It is well known that when a jet discharges at large angle into the cross-flow, there is a complex interaction between the two flows, resulting in the deflection of the jet in the direction of

the cross-flow as shown in Figure 1.5. The jet flow forms a pair of counter-rotating vortices that dominate the flow far downstream. The structure near the jet exit is dominated by ring-like structures, which become distorted with streamwise distance.

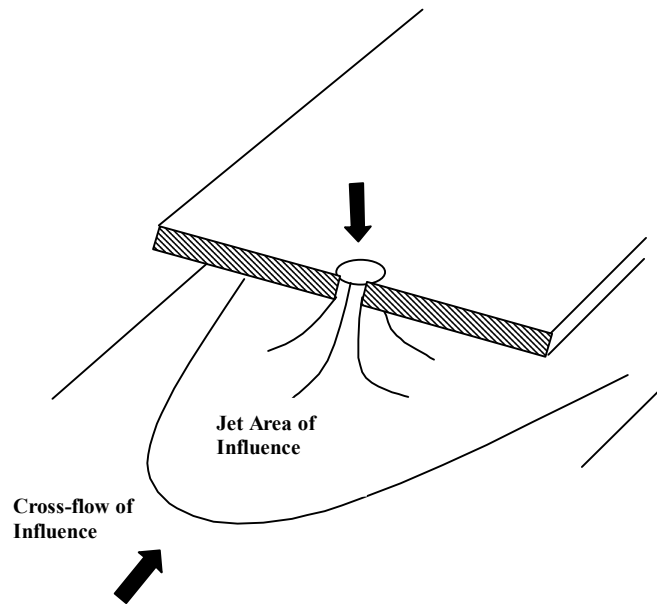


Figure 1.5 Areas of influence for the impingement jet array.

In the jet-cross-flow mixing zone, there are several vortex systems due to interactions that are both stationary and nonstationary in nature and highly three-dimensional in structure. The steady structures include the dominant rolled-up, counter-rotating vortex pair and the horseshoe vortex around the jet exit, and the unsteady structures include the unsteady wake vortex Streetshed immediately downstream of the jet exit and the free jet shear layer vortices. All those vortex structures strongly affect the passive scalar exchange between the flows.

1.3 Problem Statement

A wealth of information exists on the basic cases of individual and array jet impingement heat transfer. This information is widely used within the gas turbine design community for applicable impingement configurations and flow parameters. However, lately, newer and more specific cases of cooling designs require additional information to account for effects on the impingement heat transfer of film coolant extraction, prefilm impingement chamber, compartmentalized or zonal impingement, roughened target surfaces, and confined impingement within various wall structures. The present study investigates the effects of confining and impingement jet arrays within a smooth, stationary channel that is constrained to flow the postimpingement coolant in one direction, without film extraction. Of interest in such geometry is the heat transfer on the target surface or impingement wall. In integral structures of airfoils, end walls, or liners, the total heat transfer distribution is important to the proper assessment of thermal-mechanical loading in the component.

1.4 Objectives

An experimental study of an impingement jet with cross-flow in advanced gas turbines is proposed. The primary objectives are

1. To study the detailed heat transfer coefficient distributions under an array of impinging jets with significant cross-flow effects.

2. To establish an imaging-based experimental system for detailed local heat transfer studies on various participating surfaces.
3. To study the effects of number of jets and geometric parameters on various heat-transfer surfaces.
4. To investigate the effects of jet-to-target spacing ($H = 1.27\text{cm}$, 1.905cm , and 2.54cm), ($H/D = 1 \sim 8$) for the three test sections.
5. To obtain Nu-Re correlations for design applications.

1.5 Current Investigation

There is a general need for a more complete understanding of impingement within confined channels such that specific cases may be designed from a parametric knowledge base. The present study explores heat transfer on both the target and jet issue walls due to jet array impingement within a confined channel. The particular cases studied include one streamwise row of 6 jets, two streamwise rows of 12 jets each, and three streamwise rows of 18 jets each. Each geometry has the same physical jet-issue area. In each case, the exhaust flow is constrained to flow in one direction within the channel. The distance between the jet-issue plate and impingement plate was varied in each case. Transient liquid crystal technique was chosen as a base experimental tool because it provides full coverage of the detailed local heat transfer phenomenon and its potential to be applied on a complicated surface. Its cost effectiveness is yet another preferable factor over other techniques.

2.0 LITERATURE REVIEW

2.1 Introduction

The closed-loop cooling strategy is promising, specially in resolving the conflicting requirements for higher performance and lower emission, in other words, the need for higher inlet temperature and lower combustion temperature. Unfortunately, the cooling flow circuits and manifolding schemes are complicated in this strategy. This is particularly evident while comparing it to vanes and blades of past engines. The complexity is due to the closed-loop cooling requirement for the vane and blade, in combination with exceptionally severe hot side thermal boundary conditions. Closed-loop designs need to accumulate all spent coolant and duct them for useful work elsewhere in the engine cycle. To do this successfully and to generate effective cold-side heat transfer, innovative techniques and designs for coolant manifolding and flow distribution are needed. As such, only limited test and field data are available for the analysis and validation of the cooling design. To date, extrapolation of data and correlation, along with the best engineering judgment philosophy, have been adopted for this purpose. Thus, the vane and blade designs possess significant uncertainty regarding flow distribution and heat transfer effectiveness. Scaled Plexiglas models and testing programs are therefore necessary to quantify performance and eliminate uncertainties for the purpose of validation and improvement of proposed designs.

2.2 Prior Studies

Heat transfer has been investigated primarily for the jet impingement walls of both flat and concave surfaces, for individual jets, lines of jets, and arrays of jets. The heat transfer due to a single axisymmetric jet impinging on a smooth flat plate with free spent air discharge was investigated by Gardon and Coponpue (1962), while Gardon and Akfirat (1966) studied the heat transfer due to a two-dimensional impinging jet in the same situation. These studies determined the basic effects of jet-to-target spacing and jet Reynolds number on stagnation region and radial heat transfer. Each of these studies also demonstrated the interaction effects within sample arrays of jets. Ichimiya (1995) investigated the heat transfer beneath a single axisymmetric jet confined between two plates, both for normal and oblique impingement angles, determining the local and averaged effects of jet angling. The nature of the confinement plates was such that the wall spacing was equal to the jet diameter and the spent flow not confined by side walls. A similar confined jet study was performed by Lin, Chou, and Huang (1997) using a two-dimensional, normal jet and varying the target spacing.

Cases involving the use of a single line of impinging jets have explored the heat transfer within airfoil leading edge regions. Both Metzger and Larson (1986) and Chupp, Helms, McFadden, and Brown (1969) studied the heat transfer within a semicircular concave region with a line of circular jet impinging at the apex. The effects of target spacing, hole spacing, and jet Reynolds number were correlated. Tabakoff and Clevenger (1972) extended this information to include cases of two-dimensional jet impingement as well as jet array impingement within a semicircular concave region. Metzger, Baltzer, & Jenkins (1972) further extended such studies to include the effect of leading edge sharpness. More recently, Metzger and Bunker (1990) showed the detailed local heat transfer distributions due to line jet impingement within leading edge regions, without and with film extraction effects, respectively. Another important extension of this class of impingement was made

by Metzger and Korstad (1972), in which the effects of a cross-flow on a single line of circular jets within a channel were determined. The relative strengths of the jet flow and cross-flow as determined by other system parameters such as target spacing and Reynolds number are extremely important to the resulting heat transfer on the target wall.

Several studies have also been performed to correlate the heat transfer under an array of impinging circular jets, primarily for normal impingement on flat surfaces. Kercher and Tabakoff (1970) tested a matrix of square arrays of in-line jets over ranges of target spacing and jet Reynolds number, correlating streamwise heat transfer with geometry and flow parameters. In a series of studies by Florschuetz, Berry, and Metzger (1980), Florschuetz, Truman, and Metzger (1981), and Florschuetz, Metzger, and Su (1984), the heat transfer to a flat plate beneath arrays of impingement jets was determined, including in-line and staggered arrays and various effects of initial and developing cross-flow. Various jet array geometries were investigated in these studies, providing a major portion of the current database for heat transfer correlations of impingement arrays. Recently, detailed heat transfer information has also been obtained for such arrays by Van Treuren, Wang, Ireland, and Jones (1995) and Van Treuren, Wang, Ireland, Jones, and Kohler (1996) using liquid crystal techniques.

Two recent studies are of particular application to the present investigation. A study by Huang, Ekkad, and Han (1996) looked at the effect of confining an array of 11 rows of jets, each with just three jets across, within a channel constrained to flowing in one of three exhaust configurations. The effects on target wall heat transfer of the confining walls and cross-flow were shown for a single array geometry. Gillespie, Wang, Ireland, and Kohler (1996) determined heat transfer for a very specific case of double-row jet impingement within a confined channel, which exhausted the coolant through film holes. Heat transfer was measured in both the target wall and the

jet-issue wall. Heat transfer levels on portions of the jet issue wall were as much as half of the target wall despite the film extraction.

2.3 Impingement with Cross-Flow

Jet impingement heat transfer has become well established as a high performance technique for heating, cooling, or drying a surface. Impingement jet cooling systems have been used in advanced gas turbine engines, which operate at a high gas temperature (1300-1500 °C) to improve thermal efficiency and power output. Gas turbine blades need to be cooled to operate under the allowable temperature condition without failure. Cooling by impinging jets on the heated interior surface of the turbine components is used in turbine blade internal cooling, and there have been many experimental investigations and theoretical studies on the heat transfer characteristics of jet impingement. Chupp et al. (1969) evaluated the internal heat transfer coefficient for impingement cooling on the leading edge of a turbine blade. Studies summarized findings relating to the parametric effects of geometry, temperature, cross-flow, turbulence, and other factors on jet impingement heat and mass transfer. Florschuetz, Truman, and Metzger (1981) determined the heat transfer characteristics for jet array impingement with the effect of an initial cross-flow rate. They presented correlations for both in-line and staggered hole patterns, including effects of geometric parameters for one cross-flow direction. Downs and James (1987) presented a comprehensive literature survey of most jet impingement studies before 1987 and the correlations developed by those studies. Viskanta (1993) reviewed the heat transfer characteristics of single and multiple isothermal turbulent air and flame jet impingement on the surface. Metzger and Bunker (1990) studied impingement cooling on turbine airfoil leading-edge regions with and without film coolant

extraction. Huber and Viskanta (1994) studied the effect of jet-jet spacing and compared heat transfer from target plate perimeter and center jet impingement in a confined, impinging array of axisymmetric air jets. Ekkad, Gao, and Hebert (2002) studied the effect of jet-to-jet spacing in impingement arrays with different jet-to-target spacing. All of the previously mentioned studies observed an increase in heat transfer with jet impingement. They presented the effects of various geometrical and flow parameters on jet impingement heat transfer.

2.4 Review of Some Patent Applications

In this section, we will discuss patents, which are related to cooling of gas turbine engines or to heat exchangers. There are other fields in which the impinging jets are used and which are here omitted for brevity. Let us, for example, mention cooling of electronic components, drying in the paper industry, cooling and heating in the food industry, and annealing in metallurgy.

2.4.1 Cooling of Gas Turbine Engines

Thermal loading of some components of gas turbine engines became one of the limiting factors of their power. Therefore, intensive cooling is crucial. In modern engines, the cooling system usually incorporates the impinging jet technique for cooling of turbine blades and sometimes also for cooling of the liners of combustion chambers. The cooling air is usually bled from a compressor (see Figure 2.1), and after passing through the cooling system, it mixes with hot gases. This arrangement creates a bypass in the thermal loop of the engine, and therefore, it decreases the engine's thermal efficiency. Therefore, the flow rate of cooling air should be low and its temperature before mixing

with the hot gases should be high. A high heat transfer rate is required for fulfilling both requirements.

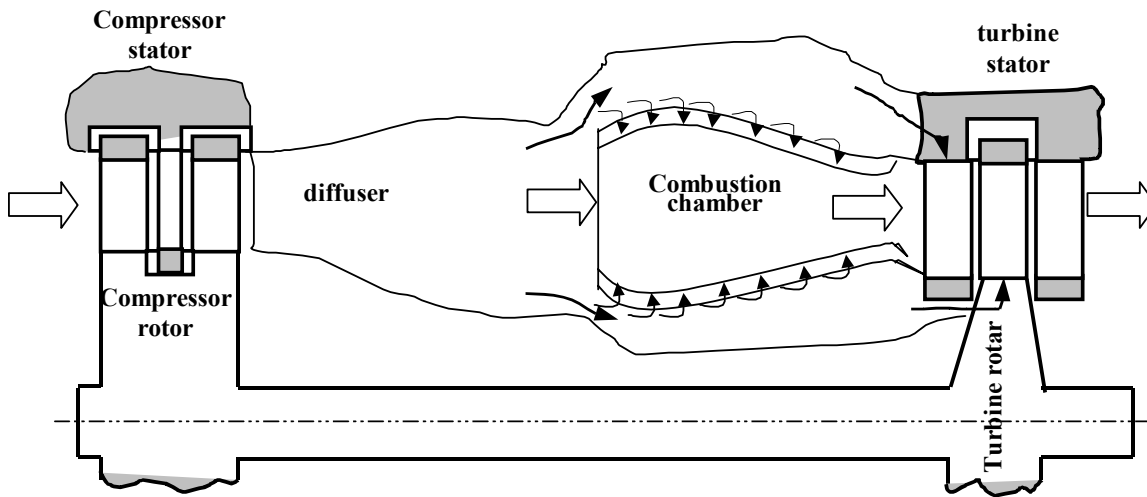


Figure 2.1 Cooling in gas turbine engine (Source: Vejrazka, 2002)

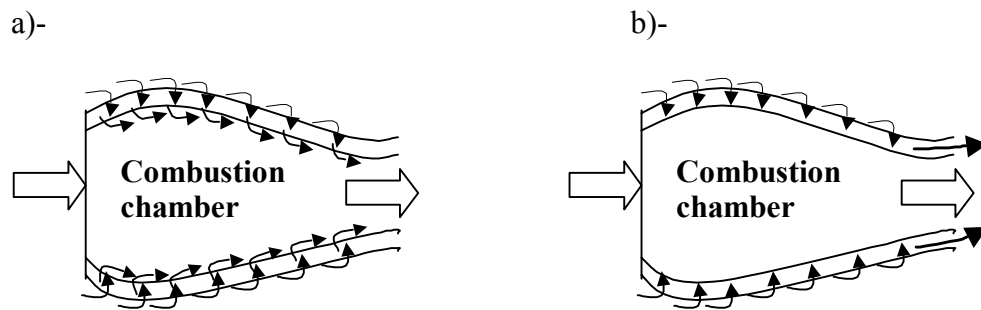


Figure 2.2 Cooling of combustion chamber: a-with film cooling, b-without film cooling

2.4.2 Cooling of Combustion Chamber and Related Patent

The impingement-cooled combustion chamber has a typical double-skin design. The inner wall, the so-called liner, is in contact with hot gases. It is impinged from the outer side by a number of jets that originate from perforations in the outer wall. After impingement, the cooling air leaves, usually through perforations in the liner or through gaps between its segments, forming a relatively cooled film that separates the liner from hot gases in the combustion chamber.

In some cases, it is not desirable to inject cooling air into the combustion chamber. Then the cooling air leaves space between the walls along the combustion chambers, creating a cross-flow, in which the jets are issued. However, the cross-flow decreases the heat transfer significantly. The general solution is to increase the section between the walls without increasing the nozzle-to-liner spacing. The heat transfer rate decreases also in regents, where the wall jets of neighboring jets collide.

2.4.3 Cooling of Turbine Blades and Related Patent

The turbine rotor and stator vanes are thermally the most loaded component of gas turbine engines. Their cooling often requires a combination of several cooling techniques. Typically, the whole blade is covered by a cooling film, which protects its surface from hot gases. In addition, they are internally cooled either by a simple or by a serpentine passage of cooled air, which is then used for generation of the cooling film. When the thermal loading of the fan is excessive or when there is need of a low flow rate of cooling air, then the impinging jets are used.

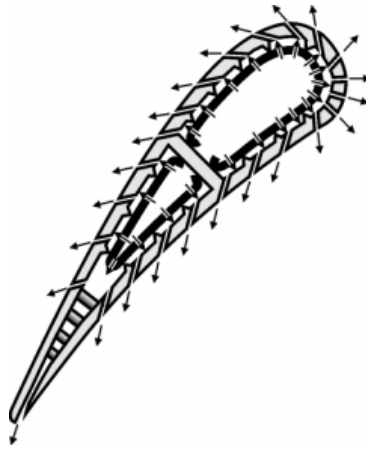


Figure 2.3. Turbine vanes with internal cooling by impinging jets

Figure 2.3 shows turbine vanes, in which the cooling air passes through a perforated metal plate, which is inserted into the blade and creates the jets. The air exits the vane by holes drilled in it, creating a cooling film. Figure 2.3 illustrates a blade made by integral casting. It has three chambers cooled by cascaded impinging jets and another five chambers cooled by a simple air passage.

2.4.4 Heat Exchangers Employing Impinging Jets

The heat transfer rate of a heat exchanger is a product of the exchange surface area and of the local heat transfer rate on this surface. Hence, there are two ways to achieve a high heat transfer rate: either by extension of the heat transfer surface or by an increase of the local heat transfer rate. The use of impinging jets represents an increase in the local heat transfer rate. However, a majority of exchangers use the former method: the extension of the exchange surface.

By surface extension, it is possible to get a very high specific surface area (in order of 1000 m^2 per m^3 of exchanger volume). This high compactness cannot be reached easily in an exchanger with impinging jets; therefore, they are not very advantageous in this application. Moreover, heat

exchangers with impinging jets have high pressure loss, which is intrinsic to jets. However, there are some exchangers that employ the jets.

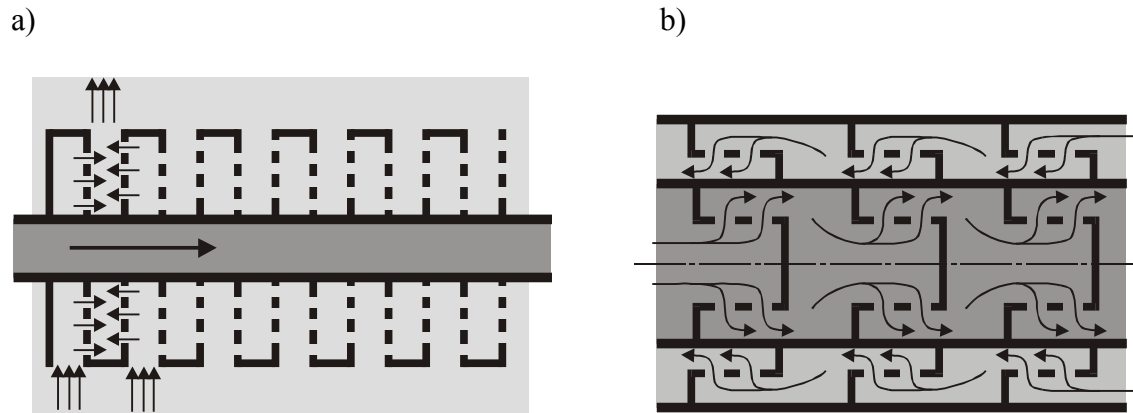


Figure 2.4 a- Arrangement of furnace recuperator, b- Heat exchanger with impingement on fins

For example, Figure 2.4(a) shows the flow arrangement in a furnace recuperator; Figure 2.4(b) illustrates the tube- and-fin exchanger with impinging on fins. The special class of heat exchangers, which are commonly referred as CHICs (compact high intensity coolers), applies the impinging jet more often. The exchangers of this class are very compact; on the other hand, they have high pressure loss and leakage problems. They are used in applications where the primary criterion is the weight of the exchanger, while the pressure loss and eventual leakage are not as important (e.g., the air conditioning unit in air planes). The design of these exchangers is similar to plate heat exchangers--a number of plates are stacked and sealed. Figure 2.5 illustrates the arrangement of one side of such an exchanger. It consists of orifice plates, which create the jets and serve as a target plate for the jets from the previous plate. Between them, there are insert plates that create a cavity for the development of jets. All plates are welded, soldered, or pressed together. Heat is conducted in the orifice plate from the side, which is connected to a heat source or to other CHIC

models. By proper arrangement of holes, a heat exchanger for two fluids can be designed (Figure 2.6)

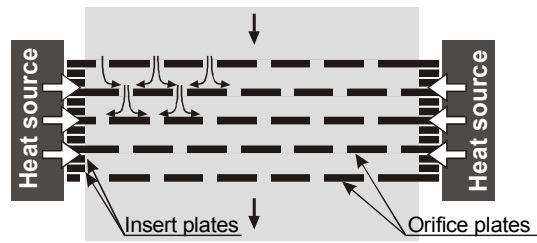
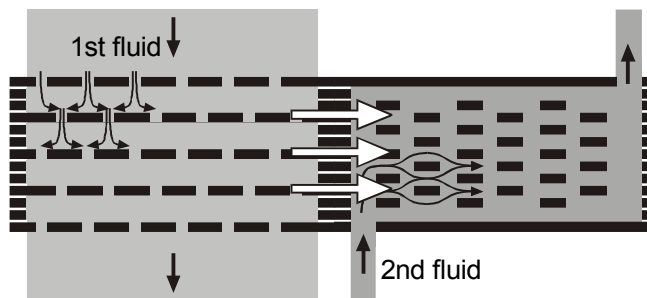


Figure 2.5 Heat exchanger module with stacked plate design (CHIC module). U.S. Patent.

a)-



b)-

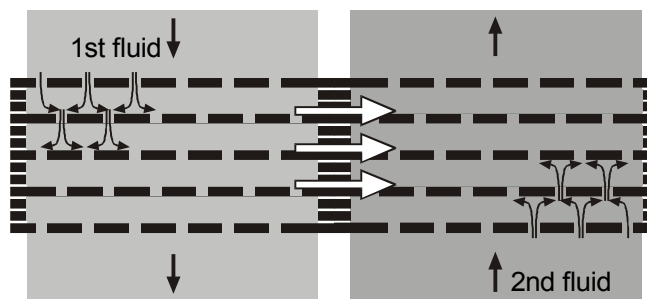


Figure 2.6 a- CHIC module and OSF module, b- Two CHIC modules. U.S. Patent.

3.0 THERMOCHROMIC LIQUID CRYSTAL

3.1 Introduction

Thermochromic liquid crystals (TLCs), as the name indicates, display different colors according to their temperature. Based on this property, TLCs can be used to indicate temperature. One example of the application of TLCs is the TLC thermometer, which is used to measure body temperature or to monitor water temperature in an aquarium. In heat transfer research, TLCs have been employed to map isotherms or to measure convective heat transfer coefficients. In addition to acting as a temperature indicator, TLCs also provide the visualization of flow and heat transfer patterns. This chapter gives a brief description of liquid crystals in general with focus on the TLC, followed by the calibration procedure and results of the TLC used in the current study.

3.2 Liquid Crystals Background

Liquid crystals have been used for convective heat transfer measurements for the past two decades. Liquid crystal techniques have emerged as standard and time-tested measurement methods for surface heat transfer measurement in the past decade. The development of accurate, plug-and-play image processing systems has contributed immensely to the accuracy and reliability of this technique. Mapping temperature and heat transfer distributions using liquid crystals has become a common practice for surface heat transfer measurements. Cholesteric liquid crystals are organic compounds derived from esters of cholesterol. Liquid crystals are referred as thermochromic because

they reflect different colors selectively when subjected to temperature changes. A reorientation of lattice structure takes place when the liquid crystals are exposed to a certain temperature. At a particular temperature, only one component of the light wavelength is reflected as the rest of the wavelengths are transmitted. The wavelength reflected is dependent on temperature. The colors of the liquid crystals can be calibrated to a particular temperature because the transition of colors is sharp and precise. Liquid crystals are microencapsulated in gelatin spheres of 5 to 30 μm to reduce the possibility of contamination due to shear stress, chemical vapors, and ultraviolet rays.

The earliest study to use liquid crystals for convective heat transfer measurements was performed by Vennemann and Butefisch (1973). They used liquid crystals for measuring aerodynamic heating in a high-speed flow setup. A transient technique was used to calculate the heat transfer coefficient. Den Ouden and Hoggendoorn (1974) performed steady state heat transfer measurements to determine stagnation heat transfer from a jet impinging on a flat plate. Cooper, Field, and Meyer (1975) measured heat transfer around cylinders using a constant heat flux source and liquid crystals. Hippensteele, Russell, and Stepka (1983), Simonich and Moffat (1984), and Hippensteele, Russell, and Torres (1985) used a thin foil heater and a liquid crystal sheet to obtain steady state heat transfer measurements. They used a composite of a heater element and liquid crystals and measured surface temperatures by providing a constant heat-flux surface. They used a 35 mm camera and a series of still images to track the yellow band of the liquid crystal range during a steady-state heating experiment. With the advent of computer technology and improvements in image processing tools, liquid crystal color processing has become more accurate and less cumbersome. Faster computers and better software tools have contributed to improved color processing, thus providing accurate, detailed heat transfer measurements.

Camci, Kim, and Hippensteele (1992) and Camci, Kim, Hippensteele, and Poinatte (1993) used advanced color processing methods to break down composite colors into hue, saturation, and intensity (H-S-I) values. They determined that the hue value of the liquid crystal color was linearly related to the surface temperature. This determination made the two-dimensional mapping of surface temperatures relatively easy and time-efficient. Camci et al. (1992) used a steady state test to map the surface temperatures and demonstrate the technique. Camci et al. (1993) used a transient test by mapping the entire surface temperature at a particular instant of time. The advantage of this test is the relatively low duration of the experiment. However, calibration of the entire liquid crystal range is required, and a sequence of images are required to map the entire surface if the surface shows large variations in heat transfer coefficient. Wang, Ireland, and Jones (1995) and Wang, Ireland, Jones, and Davenport (1996) proposed to use two or three different liquid crystal coatings to map the entire surface using a combination of intensity and hue scaling techniques. Ireland and Jones (1987) were the first to present a transient technique for heat transfer measurements using a liquid crystal coating where they tracked the movement of a single band of liquid crystals during a transient experiment. Ireland and Jones (1987) did not use an image processing system but captured a series of 35 mm camera photographs and tracked the band movement on a marked grid. Metzger and Larson (1986) used a similar method to measure heat transfer inside ducts with phase change melting point surface coatings. They presented a transient liquid crystal technique in which they used an image processing system to measure the time at which each location on the test surface reached a certain liquid crystal band temperature during a transient test. The technique basically measured iso-heat transfer coefficient lines on the liquid-crystal-coated surface. They demonstrated the technique for heat transfer measurements on a rotating disk. Vedula and Metzger (1991) measured both adiabatic wall temperature and heat transfer coefficient on a flat surface using a simultaneous solution method

for a three-temperature film-cooling problem. The accuracy of the simultaneous determination of both adiabatic wall temperature and heat transfer coefficient for film cooling situations depends on theoretical accuracy. Vedula and Metzger used two similar tests to resolve the two unknowns. They also suggested that both unknowns could be resolved by tracking two different color bands during the same experiment.

A liquid crystal, also termed mesophases, mesomorphs, mesophoric phases, or mesogens, is the state between the liquid phase and the solid phase. It flows like an isotropic liquid, yet its molecular structure maintains the characteristics of solid crystalline. It has optical properties like a solid crystalline and mechanical properties like an isotropic liquid. In addition, it has its unique properties, such as the ability of its molecular structure to be reoriented by external forces. This is because intermolecular forces in the liquid crystal phase are weak and the structures are easily affected by changes in mechanical stress, electric field, magnetic field, temperature, and chemical environment.

There are two kinds of liquid crystal that have been discovered so far according to the process by which liquid crystal are formed: lyotropic and thermotropic liquid crystals. The lyotropic liquid crystal is formed by adding solvent to certain liquid compounds; the thermotropic liquid crystal (TLC) is formed by a mesogen in the crystalline solid state. The liquid crystal phase can be destroyed by adding an extra amount of solvent in the lyotropic liquid crystal phase or by further heating in the TLC phase.

TLCs can exist in three phases: (a) smectic, (b) nematic, and (c) cholesteric (chiral nematic). The smectic liquid crystal has distinct layers of cigar-shaped molecules as shown in the schematic sketch in Figure 3.1

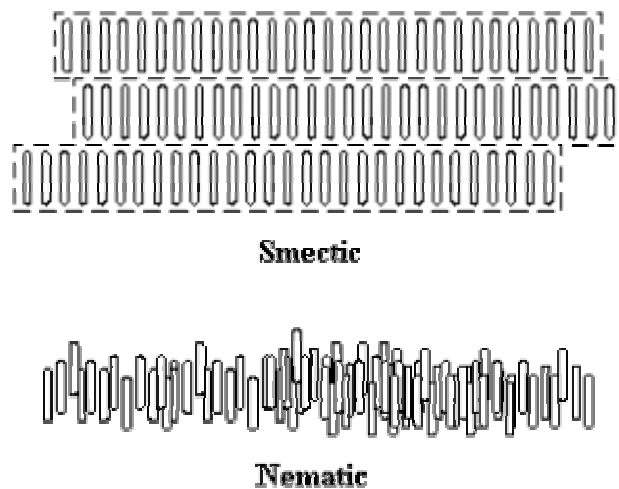


Figure 3.1 Molecular structures of TLC.

The molecules in each layer are positioned in order and have their long axes parallel. A molecule layer can only slide against other layers. The molecular structure in this phase possesses the strongest bounding intermolecular forces of the three phases.

The nematic phase has a long-range molecular orientation ordering but no positional ordering. The molecules are aligned along a symmetry axis, called the director. An external field, such as an electric field, magnetic field, or optical field can reorient the director when the field strength exceeds a certain transition threshold. The nematic phase has the weakest bounding intermolecular force of the three phases and is easily changed into an isotropic liquid phase. A schematic of the nematic liquid crystal is depicted in Figure 3.2.

The cholesteric liquid crystals consist of stacks of many parallel layers of nematic molecules. The directors of adjacent layers differ from each other by a small angle. The directors of layers can be viewed as aligning along a helix. This is why cholesteric liquid crystal is sometimes termed chiral nematic liquid crystal. As a matter of fact, the cholesteric liquid crystal has some physical properties

of the nematic liquid crystal but does not have its optical properties. All the TLCs belong to the category of cholesteric liquid crystals.

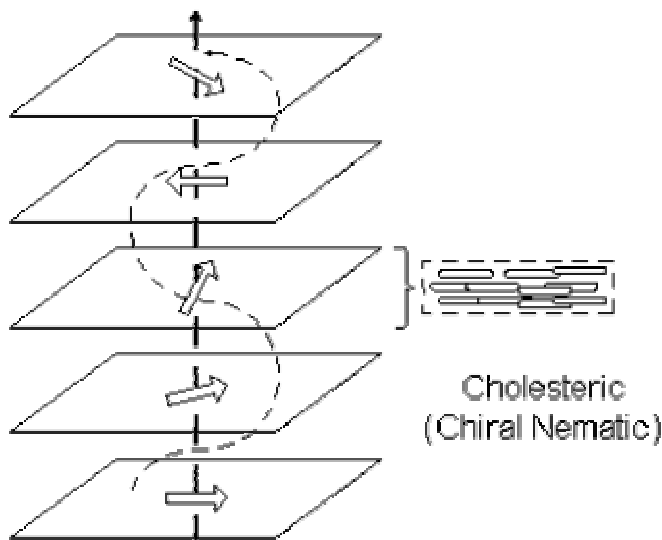


Figure 3.2 Schematic of the nematic liquid crystal.

3.3 Properties of TLCs

The optic properties of cholesteric (chiral nematic) liquid crystals include birefringence, optical activity, circular dichroism, and Bragg scattering. The net result of these optical characteristics is that when white light illuminates a cholesteric liquid crystal layer, the liquid crystal selectively reflects a narrow portion of the spectrum while the remainder is absorbed or transmitted. A black background is normally used to absorb any light that is not absorbed and provides the optimum visualization of the liquid crystal color display. When cholesteric liquid crystal compound is illuminated by white light, the spectrum of the reflected light depends on the surface temperature. Such a reflection will pass through the full spectral range from long wavelength (red) to short wavelength (blue) when heating. This sequence can be reversible on cooling. The temperature

dependence of reflecting colors comes from the peculiar molecular structure of the cholesteric liquid crystal. Maximum reflectivity of the reflected light is dependent on the pitch of the helical molecular structure. The spectral dependence of the maximum reflectivity of the light to be reflected can be determined by the Bragg diffraction equation,

$$\lambda_{\max} = p \cdot n \cdot \sin \phi \quad (3.1)$$

where λ_{\max} is the wavelength with maximum reflectivity of reflected light (i.e., the wavelength of most dominant color in the reflected light spectrum), n is the refractive index, p is the pitch of the TLC molecular layers, and ϕ is the incident angle of illuminating light. The wavelength with the maximum reflectivity will shift toward a longer wavelength in the spectrum as the pitch of liquid crystal layers increases. As the surface temperature of a TLC layer increases, the distance and angular deflection between adjacent thin molecular layers increase as well. The increase of distance between layers tends to increase the pitch. On the other hand, the increase of angular deflection tends to decrease the pitch. However, angular deflection has been found to be the more dominant effect in the TLC used in this study. Thus, when the effect is combined, the pitch decreases as the surface temperature increases. In turn, the reflected light will shift its maximum reflectivity toward shorter wavelengths as the surface temperature of the TLC increases, as inferred from Eq.(3.1). That is, as the temperature rises, the color of the TLC changes from red, to yellow, to green, to blue as its temperature goes beyond the limit of the temperature range. This behavior of the TLC is reversible during cooling. The color of the TLC is transparent, or more precisely, it does not reflect visible light when its temperature is not within the prescribed temperature range. The temperature at which the visible color can be viewed and the range of color changes are customizable. The temperature at which the colors are obtainable depends upon the point of the liquid crystal. The liquid crystal can be formulated to produce color up to about 150 °C with color ranges of 1 ° to 50 °C (Dixon, 1977). In

addition to its sensitivity to temperature, the color response of liquid crystal can be affected by other factors including electric fields, magnetic fields, certain organic vapors, and gases such as ammonia and oxides of nitrogen (Dixon). Pure liquid crystal is found to be extremely sensitive to its environment and is adversely affected by airborne contaminants and ultraviolet (UV) radiation. Airborne contaminants can change the molecular ordering of liquid crystal into a non-colored-reflecting texture. Exposure to UV light causes the event temperature to shift to a lower temperature. Adding a small amount of UV stabilizers to the liquid crystal can ease this effect of UV light on the event temperature response. Oxidative degradation becomes a problem during extended use of the liquid crystal. There was a corresponding decrease in the intensity of the color displayed. Antioxidants can be added to reduce the degradation.

The encapsulation provides a method for handling of the liquid crystal. In addition, it also renders extra protection from environmental contamination and reduces the degradation of the liquid crystal. The encapsulation is usually done by coating a thin, clear polymer layer surrounding a pure liquid crystal core. The encapsulated liquid crystal generally has a diameter between a few microns and a few millimeters. Dispersing pure liquid crystal in a clear polyurethane medium is the most developed process available to encapsulate liquid crystal. The thickness of the polymer coating of the encapsulated liquid crystal can be regulated to about 0.025 mm. Encapsulated liquid crystal has been used in the current study.

The spatial resolution of the TLC is reportedly 0.01 mm, which is the same order as the liquid crystal coating thickness. A thermographic system using TLC has been demonstrated to indicate a 0.02 °C difference in temperature if a high-resolution camera is employed to capture the reflected light. Ireland and Jones (1987) examined the response time of a thin film of encapsulated liquid crystal. For a liquid crystal layer with a thickness of 0.025 mm, a heater with a heating rate of

2,000 °C per second was used to investigate the time delay in the temperature responses of liquid crystal coating. Only a few milliseconds delay was found in the temperature response of this liquid crystal coating. In the TLC method of measuring heat transfer, the response time is negligible compared with the time of a test run. The TLC method in the current study is generally controlled to display color through the visible spectrum within 120 seconds.

3.4 Calibration of TLC

The TLC used in the current study is distributed by Hallcrest, Inc., BM/R36C5W/C17-10. This liquid crystal core is encapsulated with a clear, thin polymer layer. The encapsulation of the liquid crystal provides protection against environmental damage and UV light. Consequently, the lifetime of the liquid crystal is lengthened. This liquid crystal is referred to as liquid crystal compounds. The compounds can be sprayed as a thin layer of coating on the desired surface using an air gun or airbrush. The liquid crystal compound looks milky in a container due to light scattering. As the compound is sprayed as a thin layer, it reflects no visible light when the surface temperature is below the event temperature for displaying color. The liquid crystal used is customized to start displaying color at 33.3 °C. As mentioned above, the liquid crystal reflects light from the long wavelengths to the short wavelengths on heating. The first color shown is comprised of mainly red components. As heating continues, the color passes through the visible color spectrum from red to yellow to green and ultimately reaches blue. With further heating, the liquid crystal color will disappear. The temperature bandwidth for the color displayed is custom-tailored to 5° C.

Although the liquid crystal compound used in the current study is custom-built according to the same specification and obtained from the same manufacturer, calibration has been done for each

batch order at a different time to account for any discrepancy in different batches of liquid crystal compounds. A representative calibration of TLC used in the current study is presented in this section to demonstrate the calibration procedure and reveal the relation between the color display and surface temperature of a liquid crystal coating.

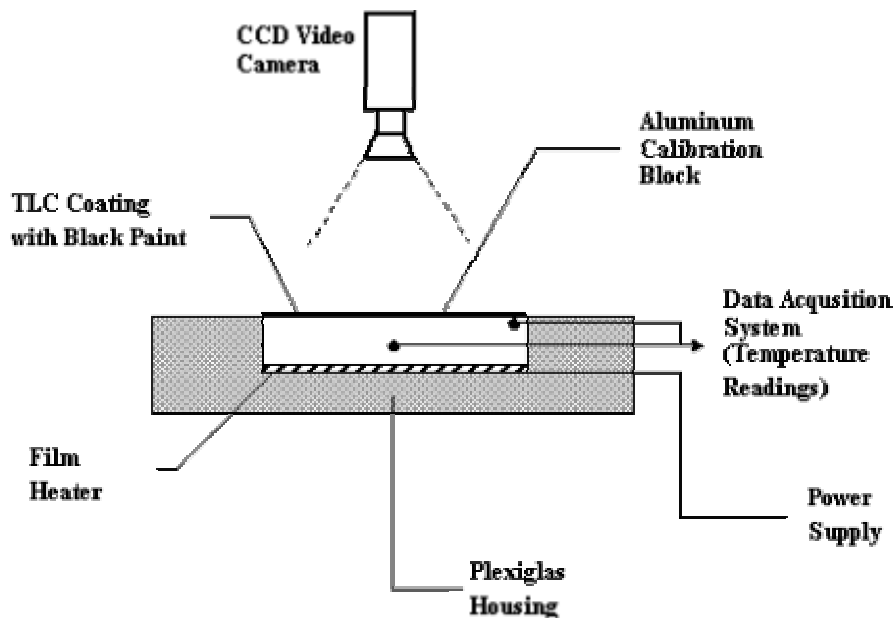


Figure 3.3 Calibration test rig.

3.4.1 Experimental Apparatus

A schematic sketch of a test rig is shown in Figure 3.3. An aluminum block was used, which had a rectangular front surface with a dimension of 5 cm × 15 cm. The thickness of the block was 0.635 cm. The block was implanted onto a Plexiglas housing as depicted in Figure 3.3. An etched-foil electric heater with an effective heating area of 5 cm × 15 cm (Omega, Inc., KH-206/2-P) was adhered to the bottom of the aluminum block and controlled by a HP 6228B DC power supply. The main reason for choosing aluminum for the calibration is that the high thermal conductivity of

aluminum provides a spatially uniform temperature within the block. Furthermore, the high thermal diffusivity of aluminum gives a fast heating response to the electric heater. A thin layer of high-heat-conductive adhesive was used to bind the heater to the back of the aluminum block. A k-type thermocouple was buried near the centroid of the aluminum block, and another K-type thermocouple was situated near the edge of the top surface of the aluminum block. The readings from the two thermocouples were monitored and recorded at a sampling rate of 10 Hz by a PC with a data acquisition board (Keithley, DAS-1801). The second thermocouple provided a measure for monitoring whether the temperature within the aluminum was spatially uniform. Test results showed that the difference between readings obtained from these two thermocouples was less than 0.1 °C. Therefore, the temperature field inside the aluminum block was almost spatially invariant. A thin layer of black paint was sprayed on the top surface of the aluminum block, followed by a thin layer of TLC. The black paint, as in the liquid crystal heat transfer measurement, functioned as a background. Against the background, the reflection of illuminated light on the liquid crystal coating can give an optimal bright color display. A CCD video camera was set about 1 m above the calibration test rig to record the image of the color change of the liquid crystal coating. One lighting setting was used in calibration.

Video images of the liquid crystal coating were recorded 10 seconds before heating began. A recording done before the heating provided background lighting information for the later data reduction. After about 10 seconds of reading, the electric foil heater, data acquisition system, and a marker, which indicated in the video when the test began for postprocessing, were simultaneously activated. The video camera recorded the live images of liquid crystal color display at a rate of 30 frames per second. A test was ended when the color of the liquid crystal coating passed the whole visible spectrum and returned to colorless. The video images and temperature readings were then

transferred to and analyzed by data reduction software (Liquid Crystal Image Analyzer, LCIA). The software matched the color-time history with the temperature-time history of a test run and yielded data for a color-temperature history.

3.4.2 Decomposition of Color

Before beginning an examination of the calibration results, a discussion of color is necessary. Color in video image processing has a dual meaning--first, it exists as a physical property of visible light, and second, this property is perceived by human vision. Color as a physical property can be defined and measured in objective and precise terms. In video image processing, color on each pixel (picture element) contains three basic components: intensity (luminance, brightness), hue (color), and saturation (purity). The intensity of a pixel can be viewed as brightness displayed in the pixel's location on the screen. In a monochrome image system, the intensity is equivalent to gray levels, which is usually divided into $2^8 = 256$ levels, because eight bits of memory are used to store the brightness information of a pixel in a black-and-white image system. Hue is a synonym for color. Visible light is electromagnetic radiation having a spectrum of wavelengths extending from approximately 400 to 780 nm, and its hue is determined by its wavelength. A mixture of white or gray light and a pure spectral color, the dominant wavelength, in the proper proportion can duplicate the appearance of any color. The ratio of the magnitude of the energy in the spectral component to the total energy of the light defines its saturation.

The trichromatic theory of color in digital image processing states that the sensation of color results from the stimulation of three sets of cones in the retina, each with a different spectral sensitivity. The perceived hue and saturation of color are determined by the ratio of amplitudes of

the responses of the sets of cones to the color stimulation. Thus, two colors will appear to have the same hue cones, even if the distribution of their spectral energies is different. A consequence of the trichromatic theory of color is that the hue and saturation of most color can be duplicated by combining three primary colors in the proper ratio. A video image system is an additive system, as it produces hues by adding the primary color components. The luminances of additive primary colors are red, green, and blue, the amplitude of their electrical analogues, E_R , E_G , E_B , are the basic color television parameters, and all other specifications are derived from them. Conventionally, the outputs of the video camera and the inputs to the kinescope are the electrical analogs of the three primary colors in the scene.

The video camera primary signals are the electrical analogs of the red, green, and blue visual components of the scene. Their colorimetry is specified by a graph of response versus wavelength. It is determined initially by the filters in the optical color splitter, but it can also be modified electrically in a camera matrix circuit by a process known as masking. With masking, it is possible to achieve a spectral response that would be impossible with the optical alone.

The product integrated over the entire spectrum determines the amplitude of each primary signal. For example, the amplitude of a green signal, E_G , is given by Eq.(3.2):

$$E_G = G_C \int L(\lambda) \cdot G(\lambda) d\lambda \quad (3.2)$$

Here, E_G is the output voltage of the green channel in the camera video output, G_C is a constant relating the electrical output of channel to luminance, λ is the wavelength, $L(\lambda)$ is the intensity of a picture element, and $G(\lambda)$ is the spectral characteristics of green primary. Primary signals E_R , E_G , and E_B determine all video signals. The video signal can be saved in composite or component format. In composite format, the luminance and chrominance signals are multiplexed within a single channel or

on the same carrier. In component formats, the luminance and chrominance signals are transmitted or recorded on separate channels or at separate times.

From this discussion of color, one can view color is composed of three components. Color can be presented by hue, saturation, and intensity in the HSI system, or it can be obtained by red, green, and blue in an RGB system. Although an HSI system has a stronger physical sense, an RGB system is more convenient in modern video image systems. An HSI system can be related to an RGB system as suggested by Farina, Hacker, Moffat, and Eaton (1994) by the following expressions:

$$H = \tan^{-1} \left(\frac{P_2}{P_1} \right) \cdot \frac{255}{2\pi} \quad (3.3)$$

$$S = \sqrt{2 \cdot (P_1^2 + P_2^2)} \quad (3.4)$$

$$I = \frac{1}{3}(R + G + B) \quad (3.5)$$

where P_1 and P_2 are defined as

$$P_1 = -0.25 \cdot R - 0.25 \cdot G + 0.50 \cdot B \quad (3.6)$$

$$P_2 = 0.25 \cdot R - 0.50 \cdot G \quad (3.7)$$

Note that all the color components (i.e., hue, saturation, intensity, red, green, and blue) are scaled from 0 to 255. In liquid crystal thermography, both systems are used in temperature and color response mapping.

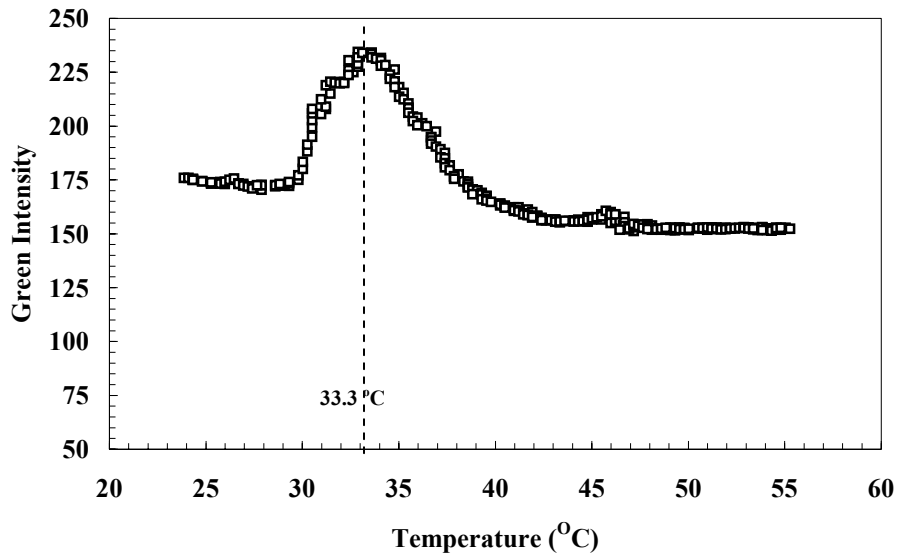


Figure 3.4 Green intensity vs. temperature of TLC.

Figure 3.4 shows the representative green intensity curve under calibration. Several calibration runs were done. The parameters that have been varied in the calibration tests include lighting, heating speed, viewing angles, and position of calibration area. Uncertainty analysis of the calibration has been performed. It is found that the temperature which corresponds to the peak of the green intensity curve of the current encapsulated liquid crystal is 33.3 ± 0.462 °C .

4.0 HEAT TRANSFER MEASUREMENT USING TLC

4.1 Introduction

TLC can be used as a precise indicator of surface temperature, providing the relation of its reflected light and surface temperature is known. The capability for temperature indication utilizes TLC application in heat transfer measurement. There are a few advantages to the liquid crystal heat transfer measurement over the other heat transfer measurement techniques. One of the most appealing advantages of the TLC method is that it provides detailed local heat transfer information and temperature distribution. Unlike traditional methods employing intrusive instrumentation, such as thermocouples, to measure the temperature, the TLC method obtains continuous local heat transfer information on the entire surface of interest rather than information on discrete points. This is particularly attractive in studying complicated heat transfer designs that have a highly spatial variation in flow and heat transfer patterns, such as designs in cooling system.

Methods of employing the TLC to attain the heat transfer measurement can be divided into two groups according to the process of the testing: the steady state and transient methods. The TLC is used to indicate or monitor temperature in both methods. The steady state method usually employs active heating to reach steady state conditions. The TLC is put to use in mapping a prescribed isotherm for different heater settings, or a number of isotherms once under a certain heater setting. The transient method resembles the thin-film method in heat transfer measurement. It treats the substrate where the surface temperature is to be measured as a semi-infinite solid domain and assumes that heat conduction within that solid domain is one-dimensional only. Lateral conduction is neglected in this method. In the transient method, the thermochromic liquid crystal coating provides

a temperature-time history, which is employed in obtaining convective heat transfer coefficients numerically. Details of these two methods are described in sections 4.2 and 4.3. Section 4.4 gives a comparison of these two techniques.

4.2 Steady State Liquid Crystal Method

The steady state liquid crystal method employs a liquid crystal coating to monitor surface temperature and map isotherms on the surface for an actively heated test model. A typical example of the steady state method using TLC is illustrated in Figure 4.1.

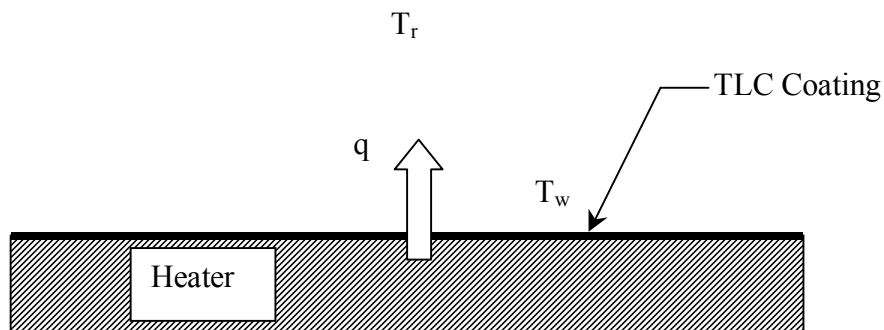


Figure 4.1 Schematic of steady state method.

Surface electrical heaters are frequently used to provide the desired heat flux condition for the experiments. Based on Newton's cooling law, the heat transfer coefficient can be determined in steady state from the equation,

$$h = \frac{q}{A(T_w - T_r)} = \frac{q_s}{q_L} \quad (4.1)$$

where q_s is the heat supplied. In cases where an electric heater is used, the supplied heat can be obtained by applying Ohm's law,

$$q_s = I^2 R = \frac{V^2}{R} \quad (4.2)$$

where R is the electric resistance of the heater, and I and V are the applied current and voltage, respectively. q_L in Eq. (4.1) accounts for the heat loss through radiation and conduction. The determination of q_L is commonly made through calibration tests under well-controlled testing conditions. A in Eq. (4.1) is the effective heat transfer surface, usually the wet surface (i.e., the surface that is directly exposed to the fluid). T_r is the reference temperature and conventionally selected to be the ambient air temperature of the external flow or bulk temperature of the duct flow.

By applying Eq. (4.1), the convective heat transfer coefficient, h , is readily obtained provided T_w is obtained under a steady state condition. T_w can be obtained from the TLC coating color transitions corresponding to specific temperatures. The TLC coating employed in this method can be narrow-band liquid crystal with one event. By adjusting the level of active heating, the TLC has, for example, a bandwidth of 1°C , a color line on the liquid crystal coating represents an isotherm of the specific temperature under a heater setting and condition. The isotherm has an accuracy of half the bandwidth, $\pm 0.5^\circ\text{C}$ in this case. The isotherm is virtually a curve of the constant heat transfer coefficient if the test is conducted under constant heat flux conditions. A photograph is usually taken to assist in giving more reliable isotherm mapping. The TLC used in a steady state method can also be a mixture of several liquid crystals with different event temperatures that can provide more than

one isotherm at a time and reduce test time and expense. However, the difference between two individual event temperatures has to be large enough to resolve isotherms. Carefully calibrated wide-band liquid crystals can be also employed in this method, with the assistance of an imaging system, to provide continuous surface temperature mapping from the colors on the surface reflected by the liquid crystal.

Many researchers have employed this method in heat studies for cooling systems. Baugh, Ireland, Jones, and Saniei (1989) used a vacuum-deposited gold coating as the surface heater and employed a narrow band liquid crystal to measure the local heat transfer coefficient on a cylinder in a cross-flow.

Hippensteele et al. (1983) developed a heat transfer measurement method using a composite of a heater element and liquid crystal. The composite was formed by stacking a plastic sheet coated with liquid crystal and a black coating, another sheet with a thin layer of a conducting material, and a heater element consisting of either a vapor-deposited coating of gold on a polyester film or a carbon-impregnated coating on a plastic sheet. They calibrated the yellow color of the TLC display and used it as a temperature indicator. Under steady state conditions, they changed the heater setting to obtain the desired isotherms. Still images of the liquid crystal display were photographed as the heater current was measured for data reduction.

Taslim, Li, and Spring (1995) applied the steady state liquid crystal method to study heat transfer on the trapezoidal passage near the trailing edge of an airfoil. Tapered turbulators were embedded on the trapezoidal passage. The liquid crystal layer was attached onto the ribs and the endwall. Taslim, Li, and Spring (1998) later used the liquid crystal method to investigate trailing-edge heat transfer for injection jets and embedded ribs. Recently, Matsumoto, Kikkawa, and Senda (1997) used liquid crystal to measure heat transfer performance for a variety of arrangements of pin fins under steady state conditions. Instead of using a single color, they adopted a neutral network

concept to match the relationship between three color components (red, green, and blue) and the thermochromic liquid crystal surface temperature.

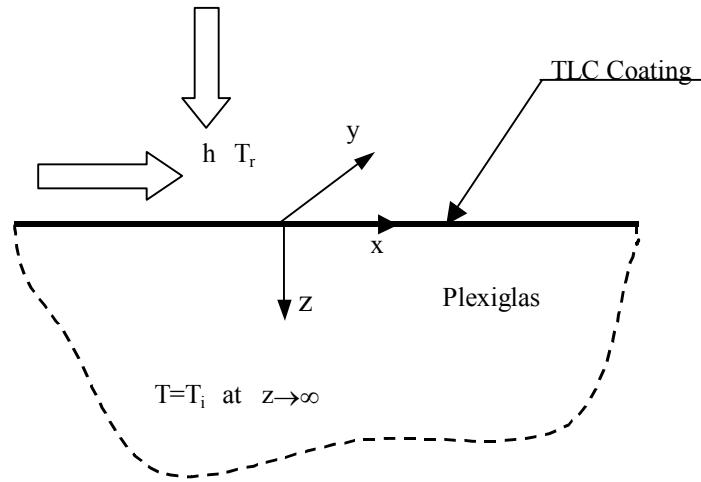


Figure 4.2 Schematic of Transient Liquid Crystal Method .

4.2 Transient Liquid Crystal Method

The transient method, sometimes termed the *thick wall*, treats the substrate (a thick Plexiglas channel wall) beneath the surface as a semi-infinite solid domain. Ireland and Jones (1985) and Metzger and Larson (1986) successfully demonstrated heat flux measurement based on a one-dimensional model using liquid crystal coatings and melting point surface coatings, respectively. The semi-infinite one-dimensional heat conduction model assumes that a semi-infinite solid domain in $0 \leq Z < \infty$ as depicted in Figure 4.2. before $t = 0$, the solid domain was maintained at temperature T_i . As time elapses ($t \geq 0$), the boundary surface at $Z = 0$ is suddenly exposed to the fluid flow and subjected to heat convection with the environment at temperature T_r . A steady convective heat transfer coefficient, h , is imposed on the surface. The mathematical formulation of the temperature

field in the solid domain can be modeled by the following one-dimensional, transient heat conduction equation:

$$k \frac{\partial^2 T}{\partial z^2} = \rho C_p \frac{\partial T}{\partial t} \quad \text{in } 0 < z < \infty, t > 0 \quad (4.3)$$

The boundary and initial conditions are

$$-k \left. \frac{\partial T}{\partial z} \right|_{z=0} = h(T_w - T_r) \quad \text{at } z = 0, t > 0 \quad (4.4)$$

$$T = T_i \quad \text{at } z \rightarrow \infty \quad (4.5)$$

$$T = T_i \quad \text{for } t = 0, \text{ in } 0 \leq z < \infty \quad (4.6)$$

where T_w is the local surface temperature (i.e., the temperature at $z = 0$ for $t \geq 0$). The temperature difference between T_w and T_r represents the driving potential for the convective heat transfer in the system. Equations (4.3)-(4.6), can be solved analytically by using the separation of variables method and the Laplace transform technique (Ozisik, 1980).

The solution for the temperature inside the solid, $T(z,t)$ can be expressed as

$$\frac{T - T_i}{T_r - T_i} = \operatorname{erfc}\left(\frac{z}{\sqrt{4\alpha t}}\right) - \exp\left(\frac{h}{k}z + \frac{h^2\alpha t}{k^2}\right) \operatorname{erfc}\left(\frac{z}{\sqrt{4\alpha t}} + \frac{h\sqrt{\alpha t}}{k}\right) \quad (4.7)$$

where \exp is the exponential function and erfc is the complementary error function defined as

$$\text{erfc}(z) = 1 - \frac{2}{\sqrt{\pi}} \int_0^z e^{-\xi^2} d\xi \quad (4.8)$$

Note that $\text{erfc}(\infty) = 0$ and $\text{erfc}(0) = 1$. $T_w = T_w(z = 0, t \geq 0)$ can be obtained by substituting $z = 0$ into the equation and expressed as

$$\frac{T_w - T_i}{T_r - T_i} = 1 - \exp\left(\frac{h^2 \alpha t}{k^2}\right) \text{erfc}\left(\frac{h\sqrt{\alpha t}}{k}\right) \quad (4.9)$$

In a typical convection problem, the reference temperature T_r is readily available, or equal to the temperature of the flow stream. As the time-varying TLC images provide a relation between T_w and t over the entire viewing domain, the distribution of the local heat transfer coefficient, h , can be resolved from the above equation. Therefore, the heat transfer coefficient h can be determined from Eq. (4.7) if the initial temperature T_i , the wall temperature T_w times t , and the mean flow temperature T_r , as well as the material properties of the solid are known or determined experimentally. In the transient liquid crystal tests, T_w is conventionally the temperature at which the green intensity reaches the peak value (i.e., T_g while t is the time for the wall to reach that temperature).

True step changes of the applied flow temperatures are usually not possible in reality, and the reference temperature, in fact, is a function of time. This can be accounted for by modifying the solutions via superposition and Duhamel's theorem. The solution becomes

$$T - T_i = \sum_{i=1}^N U(t - \tau_i) \Delta T_r \quad (4.10)$$

where

$$U(t - \tau_i) = 1 - \exp\left(\frac{h^2}{k^2} \alpha(t - \tau_i)\right) \operatorname{erfc}\left(\frac{h}{k} \sqrt{\alpha(t - \tau_i)}\right) \quad (4.11)$$

Note that in transient model formulation, one of the key assumptions of this classical heat conduction problem is that the heat conduction in the x- and y-directions is negligible compared to that in the z-direction, the direction normal to the surface between the fluid and solid domains. So, only one-dimensional heat conduction is evaluated. This assumption can be also assured if the temperature gradients in the lateral directions are small compared to that in the z-direction in Figure 4.2. This is normally the situation for heat transfer on a smooth surface. A numerical study by Valencia, Fiebig, and Mitra (1995) showed that neglecting lateral heat conduction has only a 10% difference at the most sensitive spot, where the largest temperature gradient is. Another key assumption is that the heat will not penetrate and transfer out from the other end of the substrate during testing. This assumption can be assured by employing thick material with low heat conductivity, such as Plexiglas. The surface coating of the liquid crystal layer has a negligible thermal influence on the heat conduction pattern on the solid domain, because the thickness of the layer is relatively thin. The transient liquid crystal method based on a one-dimensional transient model has been successfully applied for convective heat transfer investigation. Examples include Baugh et al., (1989), Critoph and Fisher, (1998), Ireland and Jones (1985), and Yu and Chyu (1996). Some researchers used the hue of the liquid crystal surface color display to give a complete history

of the surface temperature over a full scale (Camci et al., 1993); Wang et al., (1996). Vedula and Metzger (1991) extended the transient approach to study the film cooling. Two coupled equations for the heat transfer coefficient and film effectiveness can be solved with the assistance of two temporal histories of the liquid crystal coating. Chyu, Yen, Ma, and Shih (1999) used a similar idea to the heat transfer of film cooling in a pulsating flow. Recently, Chyu and Ding (1997) suggested a numerical operation to convert the local heat transfer coefficient based on the inlet temperature to that based on the local bulk flow temperature based on the principle of the conservation of energy. A heat transfer coefficient based on the bulk temperature provides more meaningful practical heat transfer information for cooling system designs.

4.3 Comparison Between Steady State and Transient Liquid Crystal Method

Baugh et al. (1989) conducted a comparison study of the transient and steady state liquid crystal techniques. The two techniques were used to study the heat of a cylinder in a cross-flow within a rectangular duct. Although the two techniques were applied to a test rig of the same configuration and similar inlet velocity profile at the entrance of the test channel, the two techniques yielded thoroughly different thermal boundary conditions on the cylinder. The difference was caused by the individual characteristics of the two techniques. In the steady state technique, active heating is set to give a constant heat flux and the thermochromic liquid crystal is used to map isotherms. The thermal boundary condition is thus the Neuman thermal boundary condition (constant heat flux). The thermal boundary condition of the transient technique varies as the test time elapses. Nevertheless, since the entire test time is normally short, the thermal boundary condition is more or less similar to the uniform wall temperature condition. Baugh et al. found that these two techniques yielded

compatible heat transfer coefficients on the stagnation region, where the heat transfer was less dependent on the imposed thermal boundary conditions. Away from the stagnation point, the heat transfer coefficients obtained by the two techniques differed from each other, but the discrepancy was explained by the difference of the prescribed thermal boundary conditions. Baugh et al. concluded that the two techniques are agreeable in the measurement of heat transfer. They also pointed out that the transient technique is useful in test models with complex geometry. Although the steady state technique has limitations in applications on curved surfaces, it is observed to have lower uncertainty than its transient counterpart. Critoph and Fisher (1998) applied and compared transient and steady state liquid crystal techniques in an investigation of heat transfer for plate fin-tube heat exchangers. By using radiative heating to overcome the difficulties of heating posed in the steady state technique, they found the results from the steady state method and transient method were not agreeable with each other. The heat transfer coefficient in that study was evaluated using inlet temperature. Critoph et al. concluded that the steady state method is preferable on the grounds that its results are closer to those from the numerical simulation. The inconsistency of the steady state and transient techniques lies partly in the reference temperature chosen to define the convective heat transfer coefficient and may be justified by using the bulk flow temperature as a reference to define the convective heat transfer coefficients. Chyu, Ding, Downs, and Soechting (1997) pointed out that the local fluid bulk temperature, instead of the inlet temperature at the entrance section of the test channel, is the more meaningful reference temperature to be used in the liquid crystal technique.

Valencia et al. (1995) conducted a numerical investigation of the effect on the lateral heat conduction of the steady state method and two transient methods. One of the transient methods they used was the so-called thick wall method. The thick wall method, which is the transient method referred to in the current study, treats the surface of the liquid crystal coating as a boundary between

the fluid flow (air) and the semi-infinite solid substrate (Plexiglas). The other transient method studied by Valencia et al. was termed the *thin wall* method. The method uses a thin substrate as the wall of the test channel. Because the wall is thin, the variation of temperature in the direction normal to the surface is negligible. Their work reveals that neglecting lateral heat conduction has the most significant impact on steady state liquid crystal thermography. However, the two transient methods, particularly the thin wall method, yield quite accurate results even when lateral heat conduction is neglected.

From the discussion above, it is clear that for the purpose of investigating heat transfer for a complicated geometry (as in some cooling systems designs), the transient method is more suitable for the current study and was chosen as the basis of the heat transfer measurement system developed in the current study.

5.0 DESCRIPTION OF EXPERIMENT

5.1 Preparation of Test Section

A typical test model used in the measurement system is depicted in Figure 5.1. To alleviate the error incurred by the assumption of one-dimensionality and the semi-infinite domain, this approach generally requires that the test model is fabricated from a material with low thermal conductivity and the wall of the test model is reasonably thick. 1.27 cm thick clear Plexiglas is a viable choice that meets such requirements.

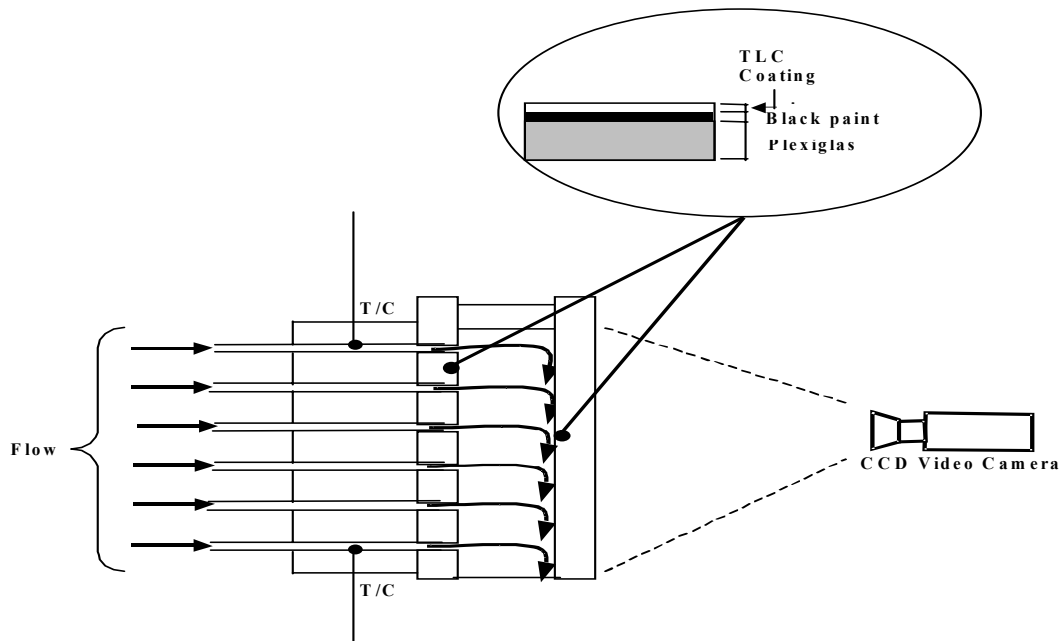


Figure 5.1 Typical test section in liquid crystal method.

The test surface to which the TLC coating will be applied was cleaned to rid it of grease and residues from the fabrication process. Grease and residues will deteriorate the optical and physical properties of the TLC so that the color display of its coating would be affected. The other surfaces of test section are also cleaned to provide good optical accessibility.

Because the TLC coating does not emit light itself, but only reflects light as a white light illuminates on the coating, a thin layer of black paint is thus necessary to provide the optimal color display of the liquid crystal coating. The black coating has to be thin to minimize added thermal resistance by the black paint coating. A layer of black coating can be made by spraying black paint on test surface using an air gun. Against the thin coating of black paint, a thin layer of encapsulated chiral nematic thermochromic liquid crystal was sprayed on the test surface of interest using an air gun. The TLC coating is well controlled to be thick enough to provide a bright color display, yet thin enough not to cause a significant disturbance on the conduction pattern within the solid. The order of the black paint coating and TLC coating can be reversed depending on the relative position of test surface to the viewing video camera. The TLC coating was always chosen to be closer to the video camera so that the bright and distinct color images could be captured.

5.2 Experimental Setup

Figure 5.2 shows a schematic sketch of an experiment setup. As indicated in Figure 5.2, compressed air, filtered and dried, was used as working fluid in the current study. The mass flow rate of compressed air was controlled by pressure regulators and adjusted through ball valves. Standard ASME orifices were employed to meter the compressed air. Readings from pressure

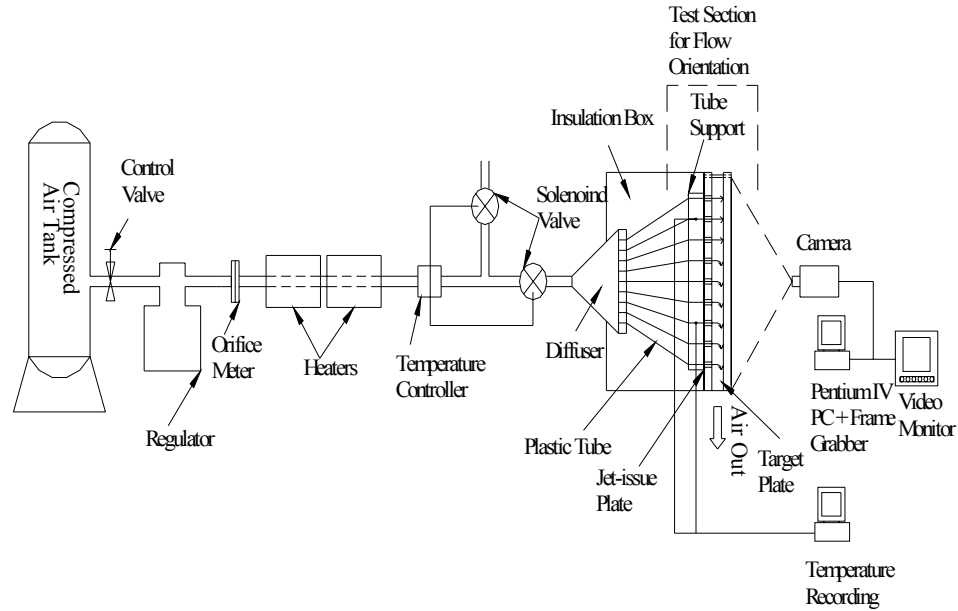


Figure 5.2. Experimental setup of liquid crystal method.

gauges were converted to mass flow rate through a computer program, which takes account of property variations caused by a change of the gas temperature.

Located upstream to the test section was a pair of tubular in-line heaters that control the temperature of the air flow stream to the desired level. The tubular heaters were rated 1500 W at 240 V and set by a Variac. Prior to the actual transient test, the compressed air flow was diverted away from the test section by two solenoid valves, which are alternatively open. A test started only when the flow rates and temperatures of both streams had reached steady state. The compressed air normally enters the jets on the test section through small pipes that are connected through a diffuser,

which made the flow uniform and provided a smooth flow of compressed air into the test section. Flow straighteners or turbulence grids are sometimes added to provide the desired flow pattern.

Thermocouples were installed in the inlet jets flow into two locations at the first and last raw jets of the test channel to survey the change of flow temperature. The thermocouple output signals were acquired by an A/D signal acquisition system at a sampling rate of 4Hz. One CCD video camera was employed to capture the real-time image of test section at the rate of 30 frames per second. The live images were simultaneously recorded by videocassette recorders (VCRs). The lighting and viewing video cameras were carefully adjusted before the test to avoid the unwanted reflection or glare caused by background lighting.

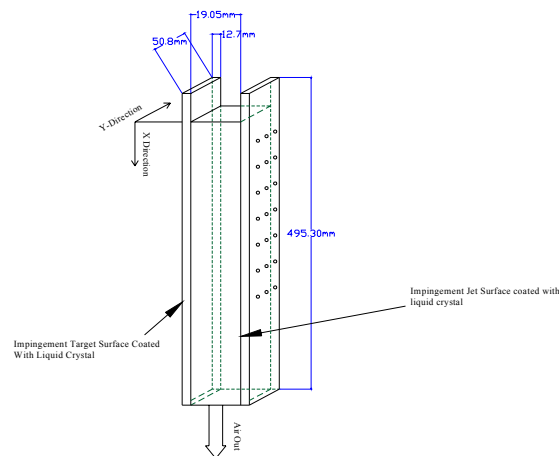


Figure 5.3 Schematic of the test section.

5.3 Test Sections

Figure 5.3 shows a three-dimensional schematic diagram of the test section and the flow direction. The channel wall of the current test section consisted of a jet-issuing plate, target plate, and side walls all made from 1.27 cm thick clear Plexiglas. The air, after impingement, is constrained to exit in a single direction along a channel formed by the target plate, the jet plate, and sidewalls. The downstream jets were subjected to a cross-flow from the upstream jets. The distance between the two plates (sidewalls) forms the height of the channel (jet-issuing-to-target plate spacing). Clear Plexiglas provided good optical accessibility and thermal conductivity and was the available choice for the liquid crystal transient test. Figure 5.4 shows the schematic of a top view and side view of the test channel. The opening of the rectangular test channel is 5.080 cm wide by 1.905 cm high. In order to study the effect of jet-to-target plate spacing on heat transfer for in-line jet array, two extra sets of sidewalls were used to replace the sidewalls. The two extra sets of sidewalls changed the height of the channel opening to 1.27 cm and 2.54 cm. The length of the entire test section was 49.53 cm. Three jet-issuing plates and one target plate were constructed. The jet-issuing and target plates were of equal size: 5.08 cm by 49.53 cm. Each jet-issuing plate had an inline array of jet holes. One jet-issuing plate had 6 rows with 1 hole in each row, the second had 12 rows with 2 holes in each row, and the third had 18 rows with 3 holes in each row. The diameter of each hole in the 6-hole test section was 9.525 mm, in the 24-hole test section it was 4.7625 mm, and it was 3.175 mm for the 54-hole test section. The jet-to-jet spacing (S_y/D_j) for all jet plates was 4 holes diameter in a spanwise, y-direction and a jet-to-jet streamwise spacing (S_x/D_j) of 6.5 holes diameter in a y-direction as shown in Figures 5.5, 5.6, and 5.7. The total area of 54 and 24 holes is the same as that of 6 holes and equals

4.275 cm² . The reason for their area similarity is to make a comparison between them. The local heat transfer coefficient is determined by the TLC technique as described in the previous chapters.

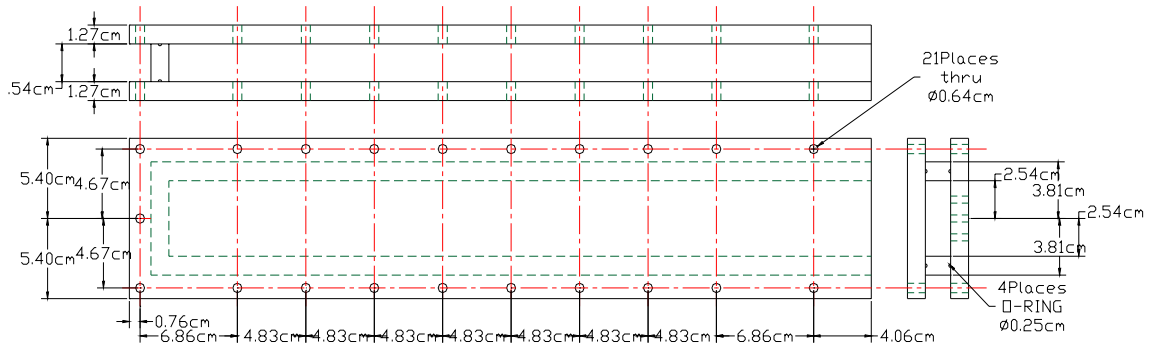


Figure 5.4 Schematic of a top view and side view of the test channel.

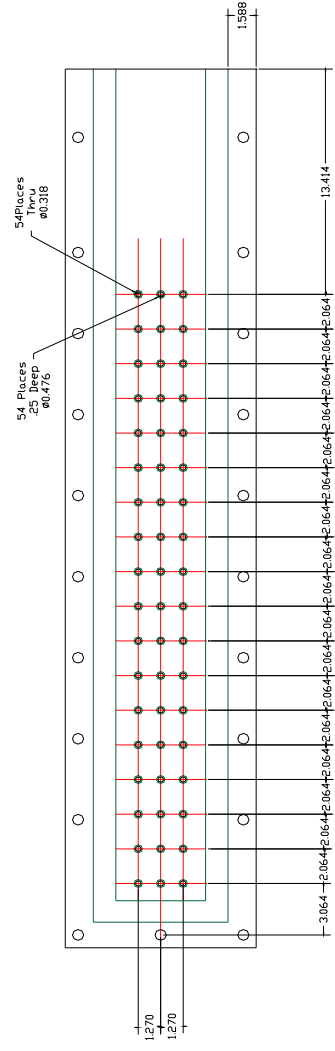


Figure 5.5 Test section of the jet-issuing plate for 54 holes (all dimensions in cm).

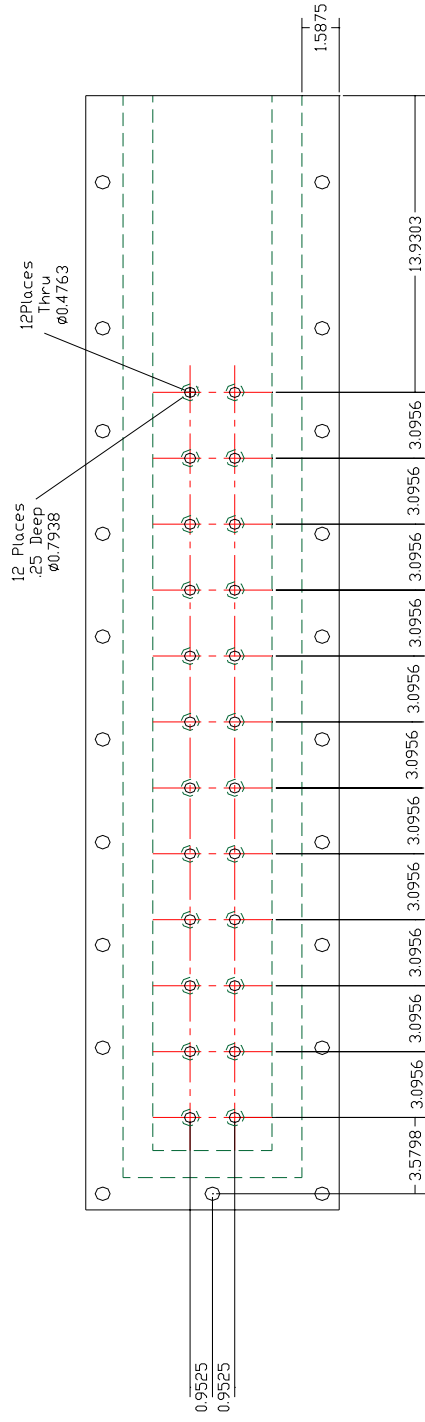


Figure 5.6 Test Section of the Jet-issuing Plate for 24 holes (all dimensions in cm).

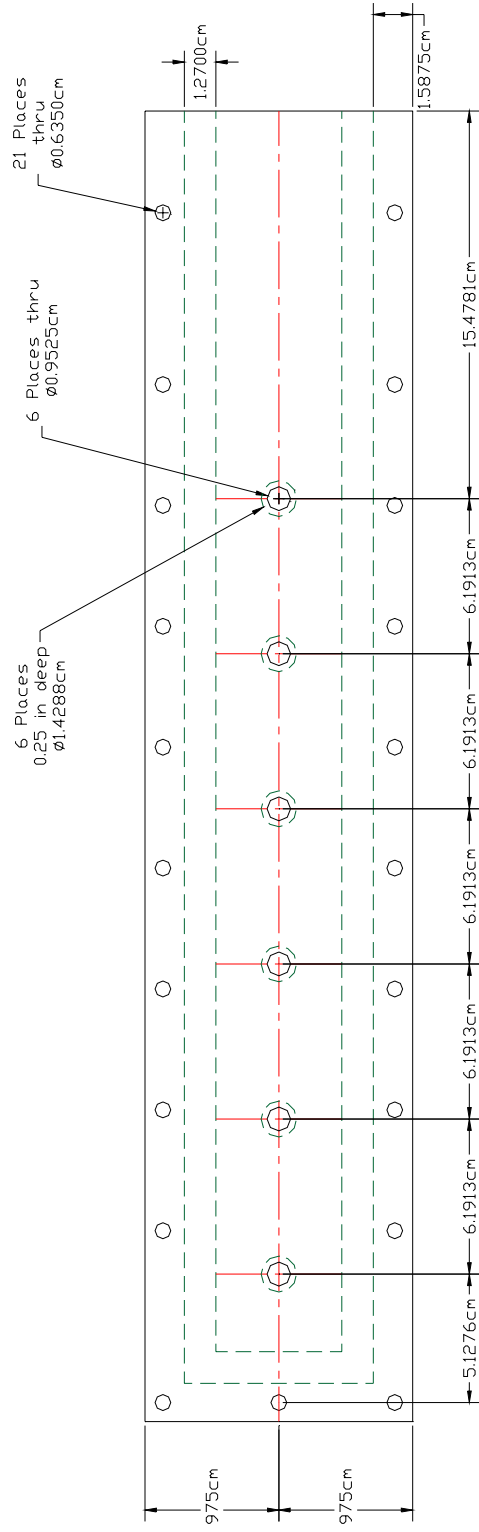


Figure 5.7 Test section of the jet-issuing plate for 6 holes (all dimensions in cm).

5.4 Test Procedure

Prior to the testing, the test section was examined to determine whether the whole test section reached a uniform temperature (initial temperature). Before each test run, the test section was put in the laboratory long enough for the entire test model to reach the ambient temperature in the laboratory. It was determined by testing that cooling down for 3 hours was long enough for the entire test model to reach the ambient temperature. The air conditioning in the laboratory was controlled at around 20 °C by a thermostat. The atmospheric environment in the laboratory provided a convenient thermal reservoir for the test section to attain the uniform temperature. The compressed air was then regulated and adjusted to the desired flow level. The flow was metered through standard ASME orifices and flows calculated through a custom-built computer program. The air was also heated to the desired temperature level.

After the flow and the temperature of the compressed air flow reached the desired steady-state level, the video camera begin to record images of the test section before the test for a few seconds. The live images before the test provided a base value for each location of the test section in the data reduction.

A test began by switching the solenoid valves simultaneously and routing the heated compressed air into the test section by using a temperature device, which was previously set to the desired temperature. Thermocouples situated before the outlets of the jet, in the first and last jets row, respectively, were also set to measure the flow temperatures. An A/D signal acquisition system with sampling of 4 Hz was used to acquire the analog output signals. The time-varying TLC images of the test surface were recorded by a CCD video camera at a rate

of 30 frames per second. A transient test was normally controlled to complete in less than 2 minutes. Within the test duration, the color of the TLC coating on the entire test surface had to pass through the entire visible spectrum, from red, to yellow, to green, to blue, and then return to transparent. The heater setting was used to control the time for the TLC coating display.

5.5 Data Reduction

A post-run image processing and data reduction procedure was to calculate the local heat transfer coefficient based on the relation of the lapse time required for a temperature change from the initial temperature to the temperature exhibited by the liquid crystals at every pixel. In the hybrid crystal technique, the solutions of the one-dimensional model over a semi-infinite substrate with a time-varying convection boundary condition is incorporated to yield the heat transfer information of the entire test surface.

Figure 5.3 illustrates a flowchart of the data reduction procedure in the liquid crystal measurement system. Color video, which was recorded by the CCD video cameras during the liquid crystal test, was digitized and saved in digital video file format in a data storage medium. The digitalization of video images was performed through a 24-bit color video capture card (WinTV PVR) with a PCI interface. Continuous capture of live video was attained at a rate higher than 10 frames per second for videos with a spatial resolution of 320 by 240 picture elements (pixels) in the current system. The digital video files were then transferred as an input to the custom-built software package, Liquid Crystal Images Analyzer (LCIA), for data reduction. LCIA is an integrated imaging processing and data reduction

package developed for the liquid crystal method in the current study. LCIA can analyze the color on each pixel from the digital video files and trace the time history for each pixel. The hardware of the current system limits the temporal resolution to be 0.1 second for an image with spatial resolution of 320×240 pixels. Note that the time history traced maximum green intensity, or the time elapsed from the start of the test to the instant when the green intensity of the pixel reached its peak value.

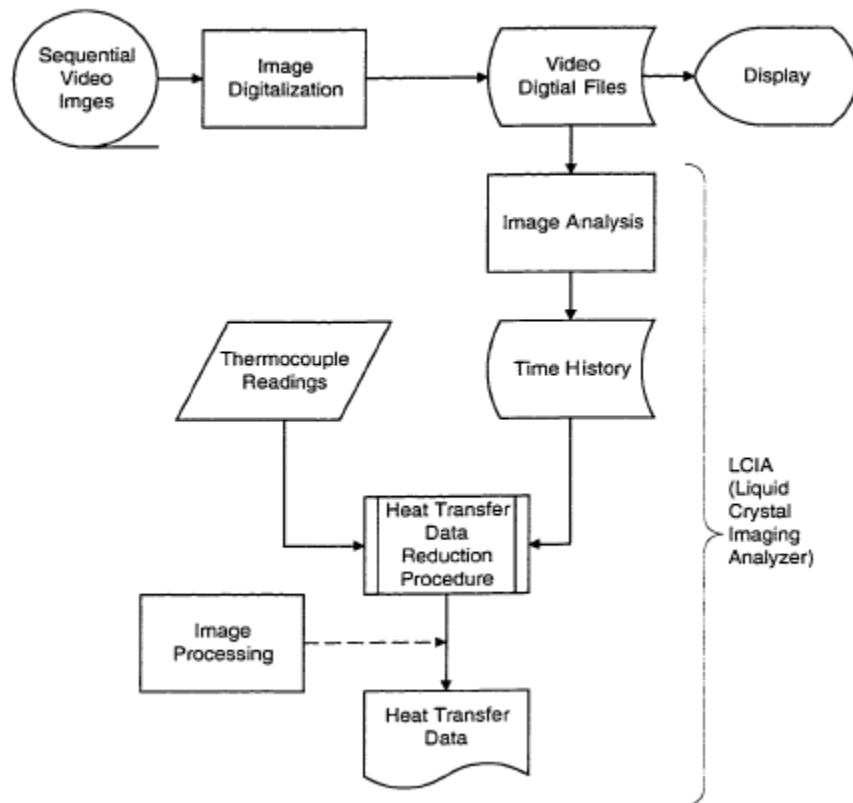


Figure 5.8 Flowchart of data reduction procedure.

LCIA used the time history and the recorded flow temperature readings during the test to deduce the local heat transfer coefficient.

5.6 System Uncertainty Analysis

An uncertainty analysis was performed for the TLC method to provide a measure of reliability for the current measurement system. The analysis employed the second power equation and followed the procedure suggested by Kline and McClintock (1953) to account for the propagation of inherent measurement errors. Because the current measurement system is virtually a combination of two independent data reduction models, the one-dimensional and lumped heat capacity models, uncertainty analyses were done separately on each model.

In the transient liquid crystal method, the local convective heat transfer coefficient, h , was deduced from an implicit equation.

$$\frac{T_w - T_i}{T_r - T_i} = 1 - \exp\left(\frac{h^2 \alpha t}{k^2}\right) \operatorname{erfc}\left(\frac{h\sqrt{\alpha t}}{k}\right) \quad (5.1)$$

In these implicit expressions, the heat transfer coefficient can be identified to be dependent on the following measured variables: T_i , T_r , T_w , and t , that is, h can be expressed as:

$$h = h(T_i, T_r, T_w, t) \quad (5.2)$$

The uncertainty interval of h can be estimated from the uncertainty intervals associated with all the independent measured variables based on the same odds. Kline and McClintock suggested that the uncertainty interval could be calculated as:

$$\delta h = \left\{ \left(\frac{\partial h}{\partial T_i} \delta T_i \right) + \left(\frac{\partial h}{\partial T_r} \delta T_r \right) + \left(\frac{\partial h}{\partial T_w} \delta T_w \right) + \left(\frac{\partial h}{\partial t} \delta t \right) \right\}^{1/2} \quad (5.3)$$

In Eq. (5.3), the first-order derivatives of the independent variables are called sensitivity coefficients. The sensitivity coefficient determines how a measured error of an independent variable affects the overall uncertainty. Because the heat transfer coefficient, h , is implicit expressed in Eq. (5.1), it is nearly impossible to analytically evaluate sensitivity coefficients of the independent variables in Eq. (5.3). Consequently, a numerical evaluation becomes the only way to obtain the derivatives. A forward difference method is employed to obtain the sensitivity coefficient (Moffat, 1982). The evaluation of the sensitivity coefficient is obtained by the equation:

$$\frac{\partial h}{\partial x_i} \cong \frac{h|_{x=x_i+\Delta x} - h|_{x=x_i}}{\Delta x} \quad (5.4)$$

where x_i represents any of the independent variables, $h|_{x=x_i}$ is h evaluated at $x = x_i$, and Δx is a small increment. In the present uncertainty analysis, $\Delta x/x=1\%$ has been employed. For a certain independent variable x_i , $h|_{x=x_i+\Delta x}$ is obtained by replacing $x_i + \Delta x_i$ with x_i while keeping other independent variables constant in the data reduction program. The sensitivity coefficient can be obtained by dividing the difference of h by the

increment of the independent variable. Once the sensitivity coefficients are evaluated, the uncertainty of the heat transfer coefficient can be obtained using the measurement uncertainties. The measurement uncertainties are found to be 0.5 °C in the thermocouples, 0.2 °C for the liquid crystal color response, and 0.1 second for the video image processing. By employing Eq. (5.3), the relative uncertainty for the one-dimensional model is found to be 5.52%.

6.0 RESULTS AND DISCUSSION

6.1 Detailed Local Heat Transfer Coefficient

Figures 6.1, 6.3, and 6.5 show detailed local heat transfer distributions for the 6-hole target plate as the function of nondimensional location X/D_j on the test surface for all four Reynolds numbers for jet-to-target plate spacing that is $H/D_j = 1.33, 2,$ and 2.67 . The results are presented from $X/D_j = 0$ to $X/D_j = 52$ in the streamwise or axial direction over the entire span.

Figures 6.7, 6.9, and 6.11 show detailed local heat transfer distributions for the 24-hole target plate as the function of nondimensional location X/D_j on the test surface for all four Reynolds numbers for jet-to-target plate spacing that is $H/D_j = 2.67, 4,$ and 5.33 . The results are presented from $X/D_j = 0$ to $X/D_j = 104$ in the streamwise direction over the entire span.

Figures 6.13, 6.15, and 6.17 show detailed local heat transfer distributions for the 54-hole target plate as the function of nondimensional location X/D_j on the test surface for all four Reynolds numbers for jet-to-target plate spacing that is $H/D_j = 4, 6,$ and 8 . The results are presented from $X/D_j = 0$ to $X/D_j = 156$ in the streamwise or axial direction.

Results for target plates show an increase in the local heat transfer coefficient for an increase in channel Reynolds number. The heat transfer coefficient decreases as X/D_j increases. It is evident that the cross-flow increases with increasing X/D_j in the upstream region. The jets show strong impingement at small X/D_j , where the cross-flow is very weak. Further downstream, the jets are pushed away from the target surface because of a stronger

cross-flow. This reduces the jet impingement, thus decreasing the local heat transfer coefficient underneath the jets. Also, the jets appear to show a shift in impingement location at large X/D_j because of the strong cross-flow. The heat transfer coefficients in the 54-hole target plate are higher than those in the 6- and 24-hole plates due to less jet-to-jet spacing in the 54-hole plate, which may produce more flow interaction between the impingement jets.

Figures 6.19, 6.21, and 6.23 show detailed local heat transfer distributions for the 6-hole jet-issuing plate as the function of nondimensional location X/D_j on the test surface for all four Reynolds numbers for jet-to-target plate spacing that is $H/D_j = 1.33, 2,$ and 2.67 . The results are presented from $X/D_j = 0$ to $X/D_j = 52$ in the streamwise or axial direction over the entire span.

Figures 6.25, 6.27, and 6.29 show detailed local heat transfer distributions for the 24-hole jet-issuing plate as the function of nondimensional location X/D_j on the test surface for all four Reynolds numbers for jet-to-target plate spacing that is $H/D_j = 2.67, 4,$ and 5.33 . The results are presented from $X/D_j = 0$ to $X/D_j = 104$ in the streamwise or axial direction over the entire span.

Figures 6.31, 6.33, and 6.35 show detailed local heat transfer distributions for the 54-hole jet-issuing plate as the function of nondimensional location X/D_j on the test surface for all four Reynolds numbers for jet-to-target plate spacing that is $H/D_j = 4, 6,$ and 8 . The results are presented from $X/D_j = 0$ to $X/D_j = 156$ in the streamwise or axial direction over the entire span.

Results for the jet-issuing plate show an increase in the local heat transfer for an increase in channel Reynolds number. The results show a high heat transfer coefficient at the small X/D_j , where the cross-flow is rather weak. Further downstream, where the cross-flow is stronger, the heat transfer coefficients increase. The heat transfer coefficients are rather low at the end of the test section, where there are no jets.

The heat transfer coefficient of jet-issuing plates are more uniform than those of the target plate. At the most upstream region, cross-flow is weak, and thus, high heat transfer coefficients are obtained, which are dominated by strong circulation of jet impingement. Farther downstream from jet rows 4 to 10, a stronger cross-flow develops that prevents jet impingement entrainment and circulation; therefore, the heat transfer coefficients became lower. When a strong cross-flow is developed, the interaction of jets and main flow may primarily enhance the heat transfer of the jet issue plate.

6.2 Span-Averaged Nusselt Number Distribution

The nondimensional heat transfer coefficient on the target and jet-issuing plate of the walls of the rectangular channel is represented by the Nusselt number as

$$Nu = \frac{hD_j}{k} \quad (6.1)$$

where D_j is the jet diameter and k is the conductivity of the air. The Reynolds number used herein is based on the jet parameter, shown in Eq. (6.2) as

$$Re = \frac{\bar{u}D_j}{\nu} \quad (6.2)$$

Where \bar{u} is the jet average velocity, and ν is the viscosity of the air.

The following results were obtained:

1. Figures 6.2, 6.4, and 6.6 show the effect of the Reynolds number on span-averaged Nusselt number distributions for the 6-hole target plate with $H/D_j = 1.33$, 2, and 2.67.

2. Figures 6.8, 6.10, and 6.12 show the effect of the Reynolds number on span-averaged Nusselt number distributions for the 24-hole target plate with $H/D_j = 2.67$, 4, and 5.33.

3. Figures 6.14, 6.16, and 6.18 show the effect of the Reynolds number on span-averaged Nusselt number distributions for the 54-hole target plate with $H/D_j = 4$, 6, and 8.

4. Figures 6.20, 6.22, and 6.24 show the effect of the Reynolds number on span-averaged Nusselt number distributions for the 6-hole jet-issuing plate with $H/D_j = 1.33$, 2, and 2.67.

5. Figures 6.26, 6.28, and 6.30 show the effect of the Reynolds number on span-averaged Nusselt number distributions for the 24-hole jet-issuing plate with $H/D_j = 2.67$, 4, and 5.33.

Figures 6.32, 6.34, and 6.36 show the effect of the Reynolds number on span-averaged Nusselt number distributions for the 54-hole jet-issuing plate with $H/D_j = 4$, 6, and 8.

Results for the target plates show that the Nusselt numbers increase with an increase in Reynolds number. The Nusselt number decreases toward the exit direction

(large X/D_j). The effect of cross-flow reduces The Nusselt number at large X/D_j . The jets also appear to tilt toward the cross-flow direction downstream to large X/D_j .

Results for the jet-issuing plate show that the Nusselt numbers increase with an increase in Reynolds number. The effect of weak cross-flow at small X/D_j increases the Nusselt number on the jet-issuing plate. However, strong cross-flow at large X/D_j increases the Nusselt number. The Nusselt number is very low in the area with no jets at the end of the test section.

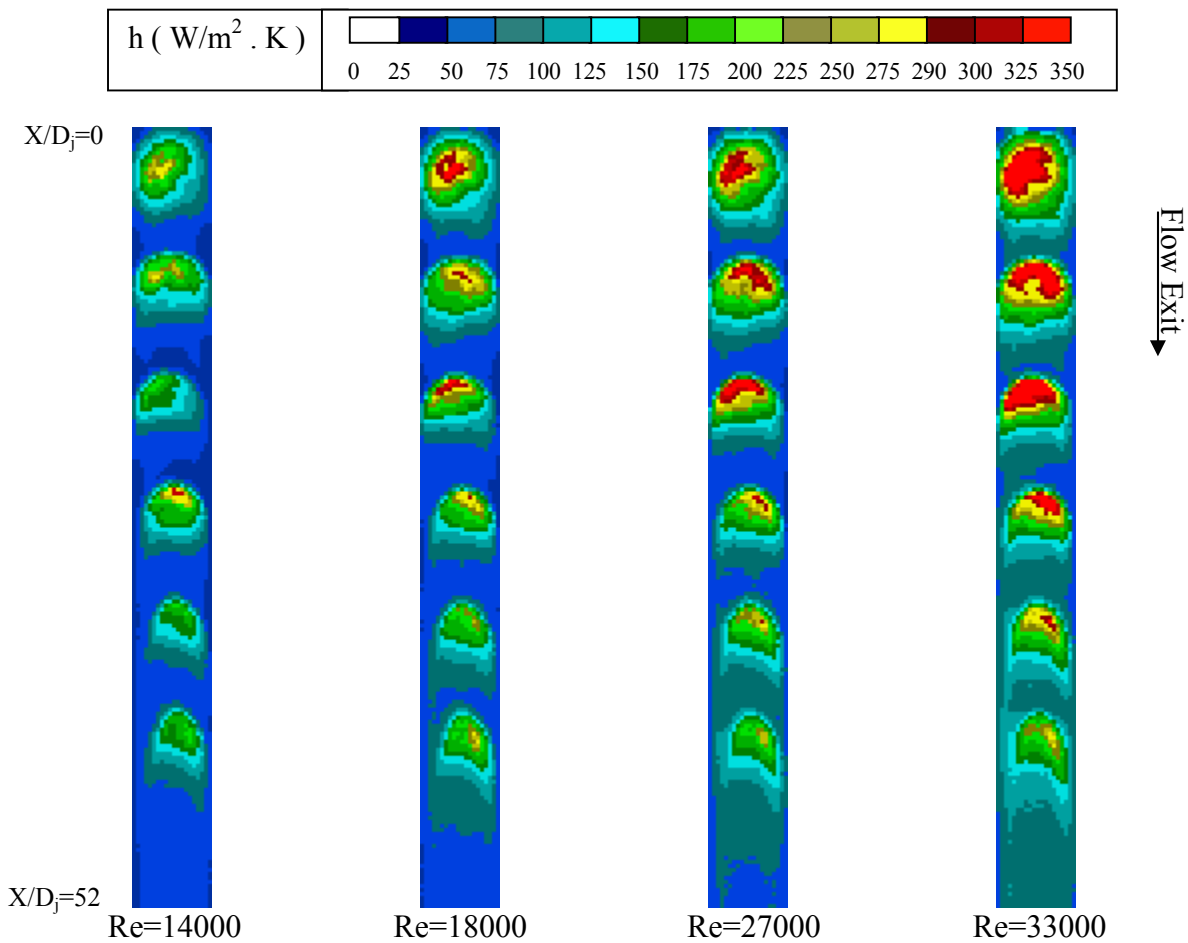


Figure 6.1 Local heat transfer coefficient for target plate with 6 hole and $H/D_j = 1.33$

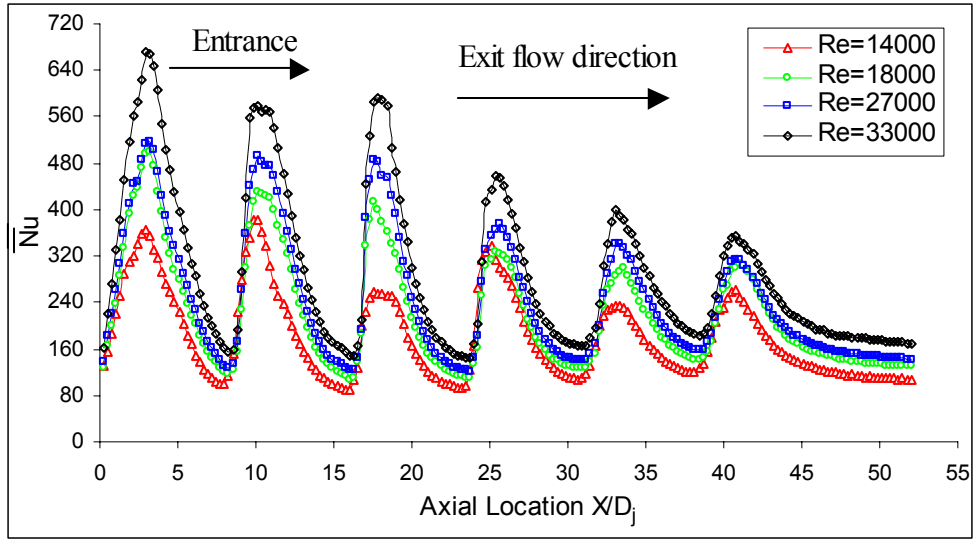


Figure 6.2 Span-averaged Nusselt number for target plate with 6 hole and $H/D_j = 1.33$.

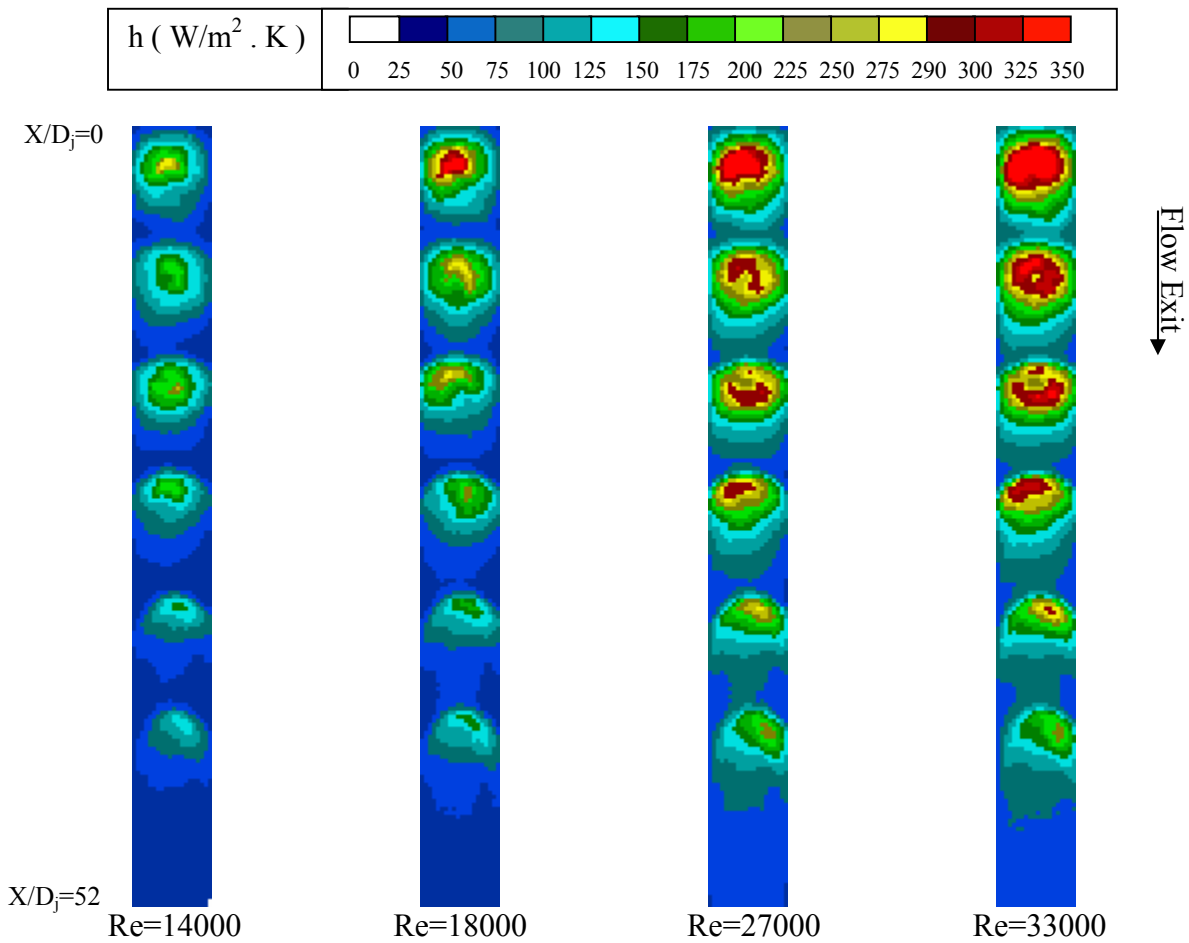


Figure 6.3 Local heat transfer coefficient for target plate with 6 hole and $H/D_j = 2$.

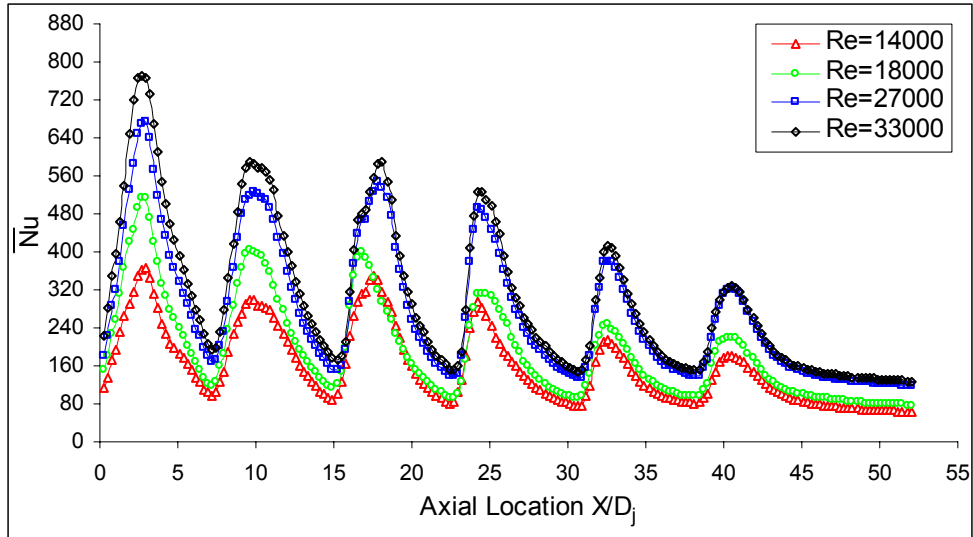


Figure 6.4. Span-averaged Nusselt number for target plate with 6hole and $H/D_j = 2$.

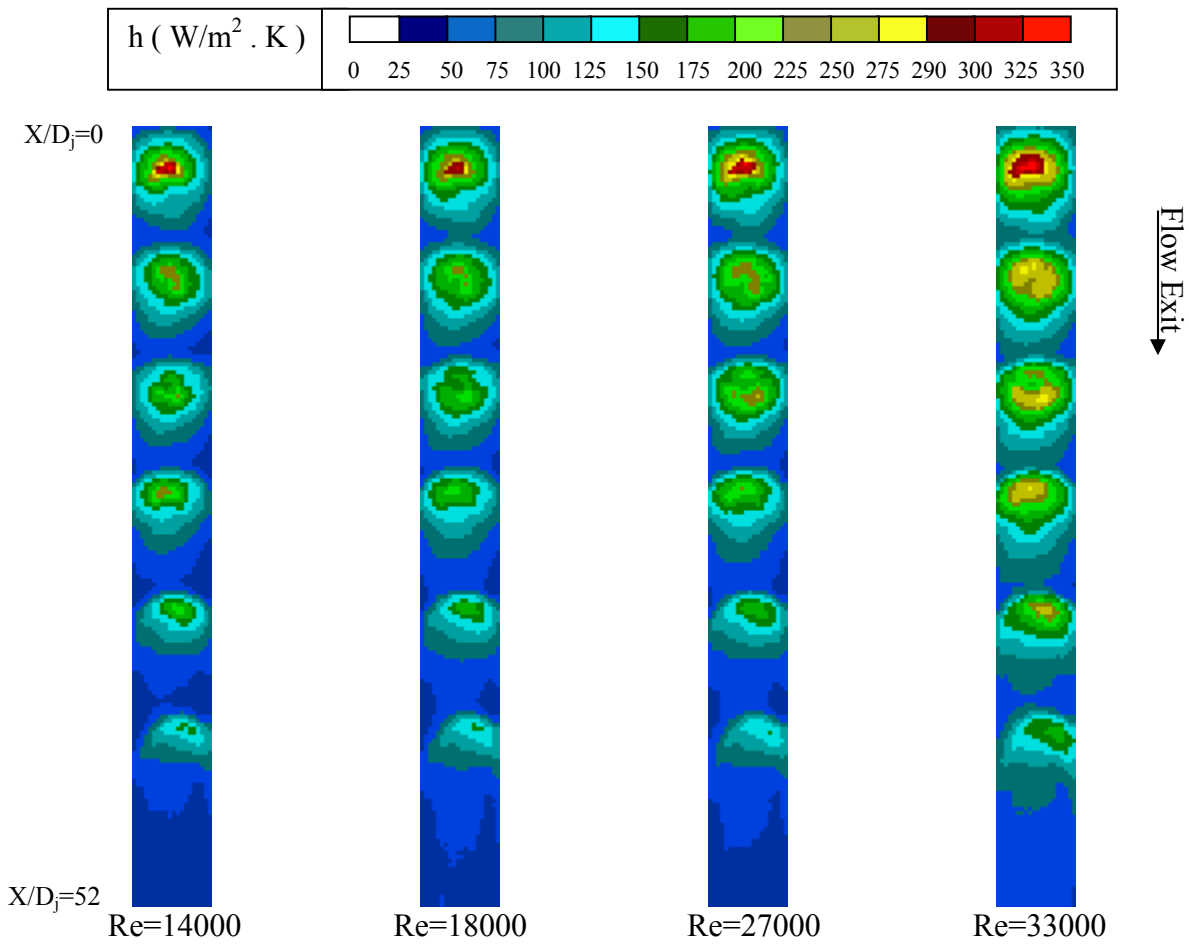


Figure 6.5 Local heat transfer coefficient for target plate with 6 hole and $H/D_j = 2.67$.

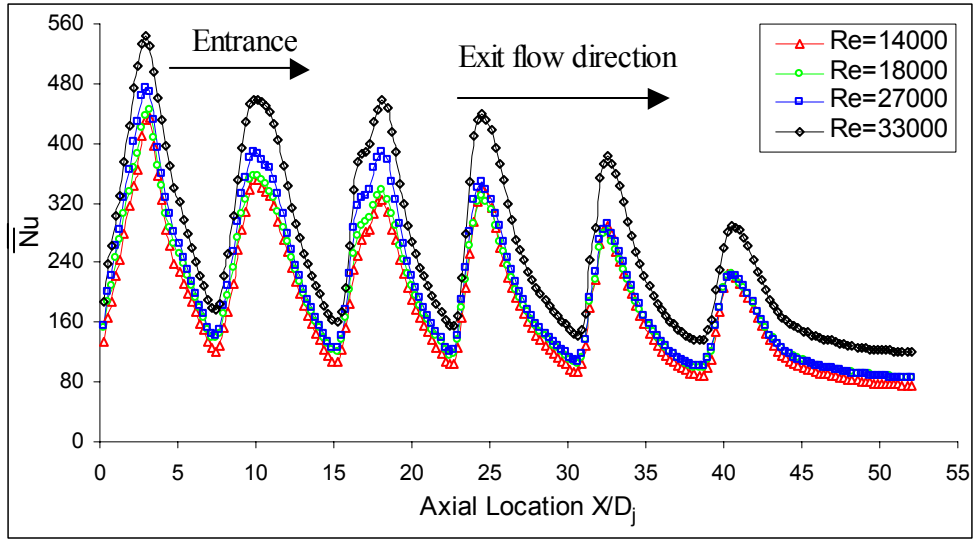


Figure 6.6 Span-averaged Nusselt number for target plate with 6 hole and $H/D_j = 2.67$.

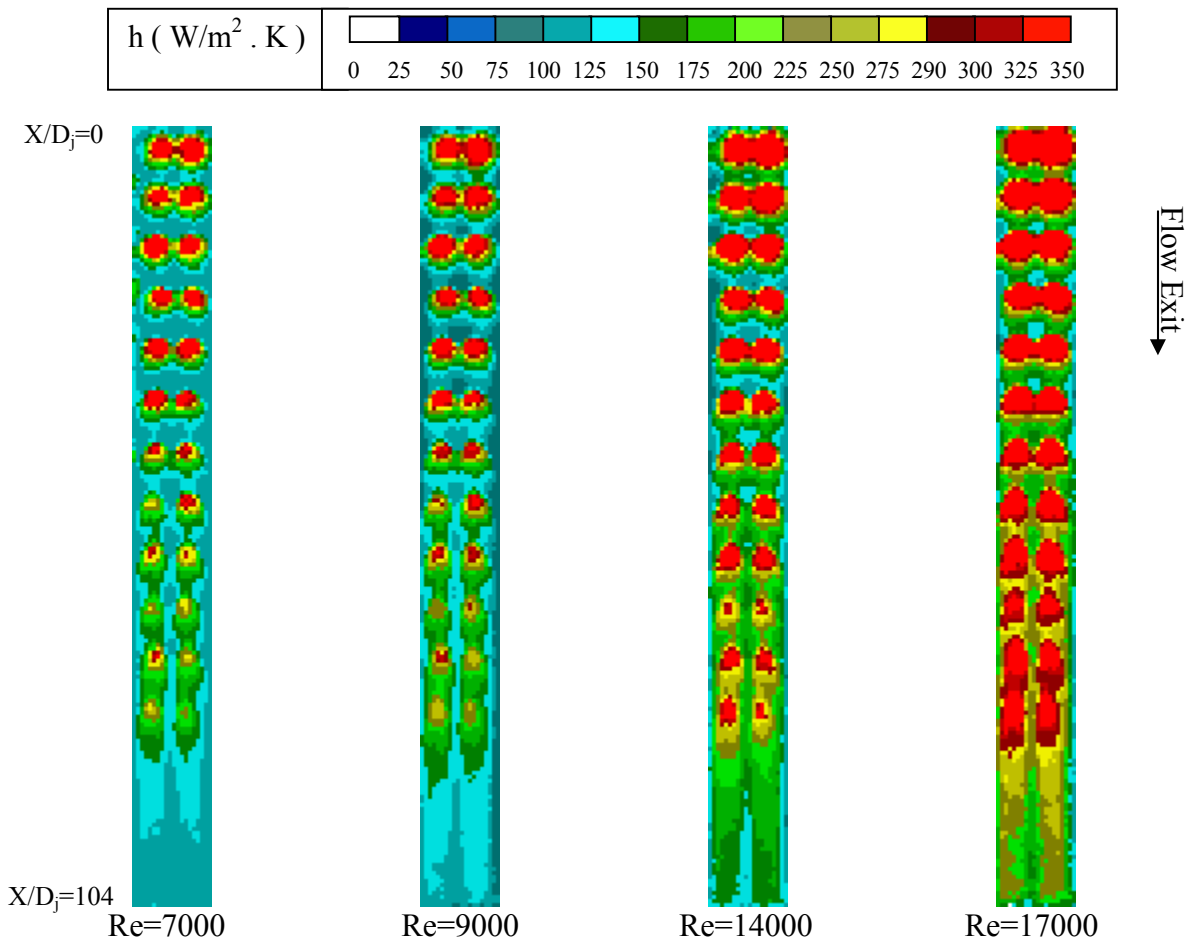


Figure 6.7 Local heat transfer coefficient for target plate with 24 hole and $H/D_j = 2.67$.

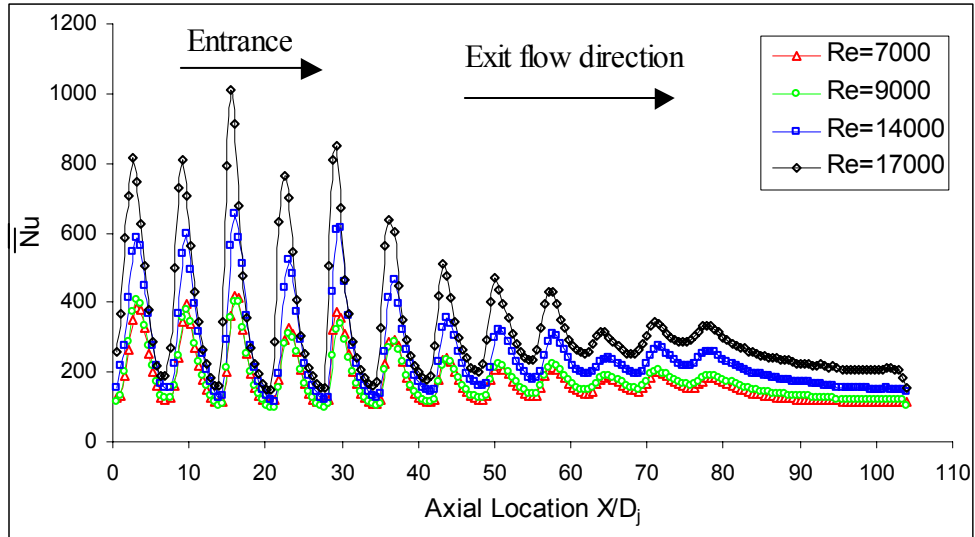


Figure 6.8 Span-averaged Nusselt number for target plate with 24 hole and $H/D_j = 2.67$.

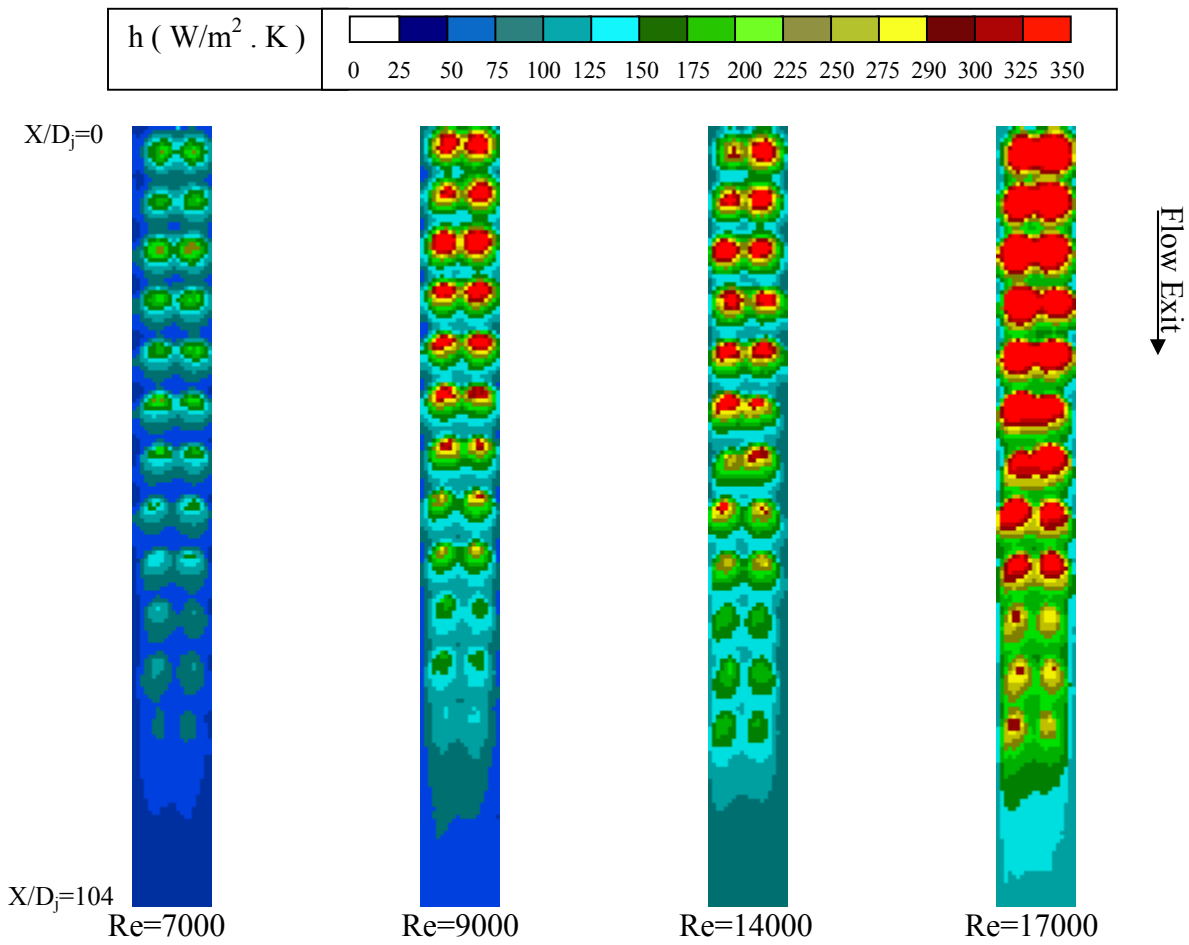


Figure 6.9 Local heat transfer coefficient for target plate with 24 hole and $H/D_j = 4$.

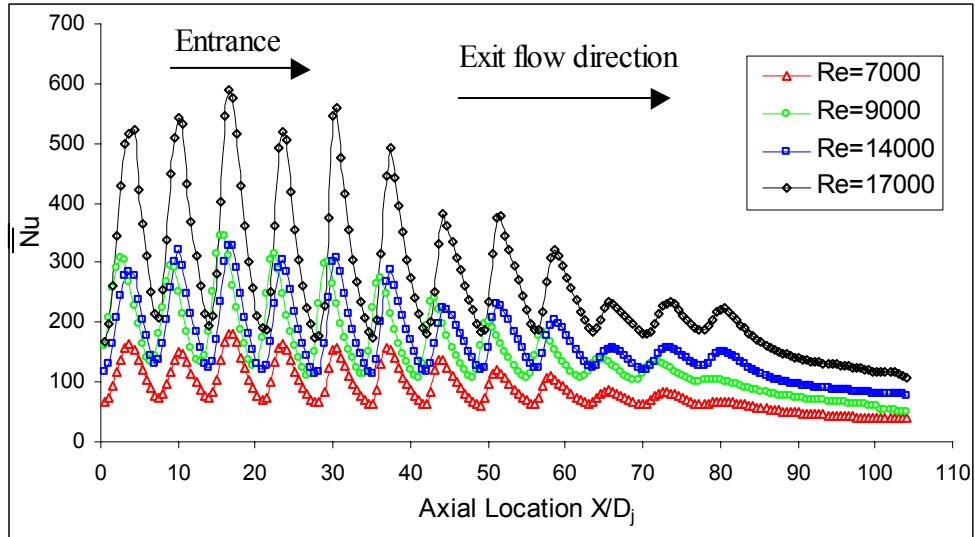


Figure 6.10 Span-averaged Nusselt number for target plate with 24 hole and $H/D_j = 4$.

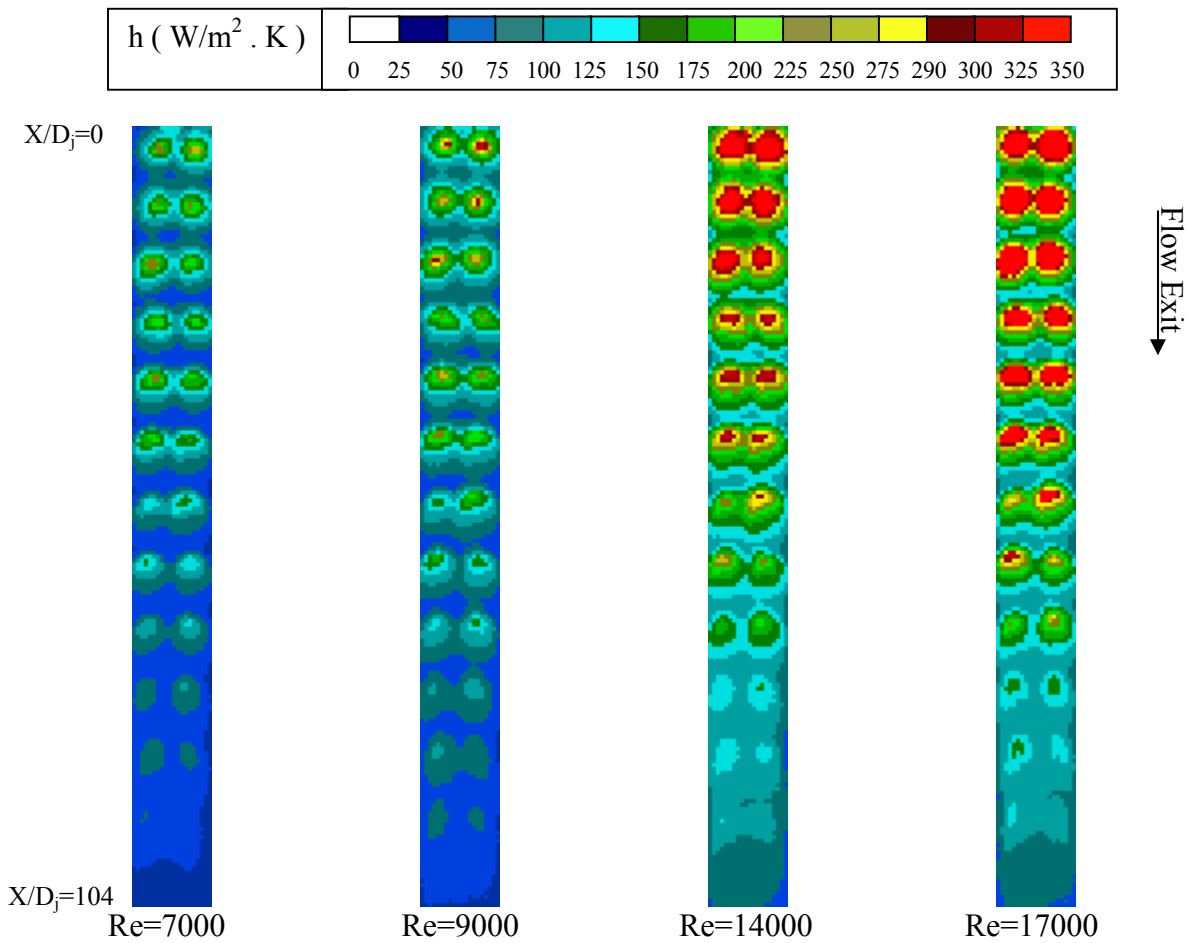


Figure 6.11 Local heat transfer coefficient for target plate with 24 hole and $H/D_j = 5.33$.

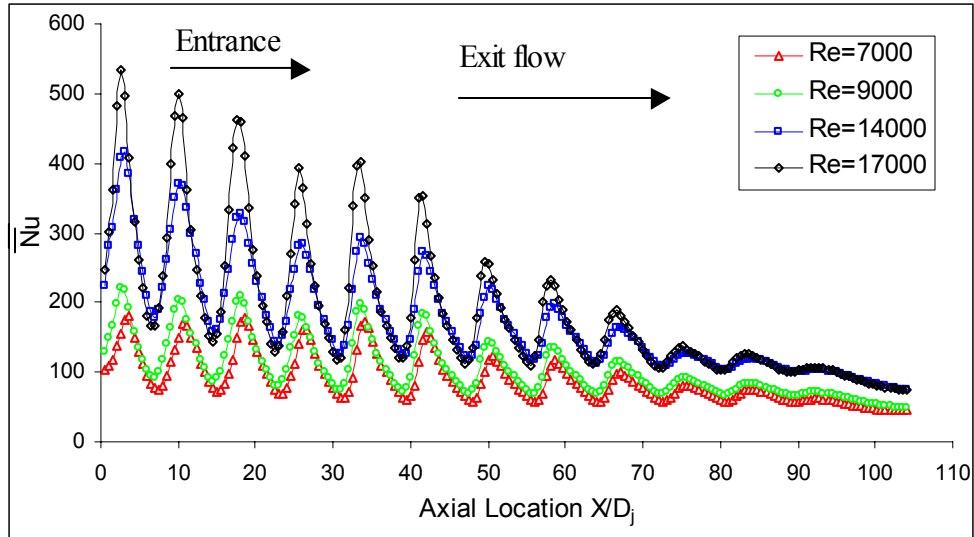


Figure 6.12 Span-averaged Nusselt number for target plate with 24 hole and $H/D_j = 5.33$.

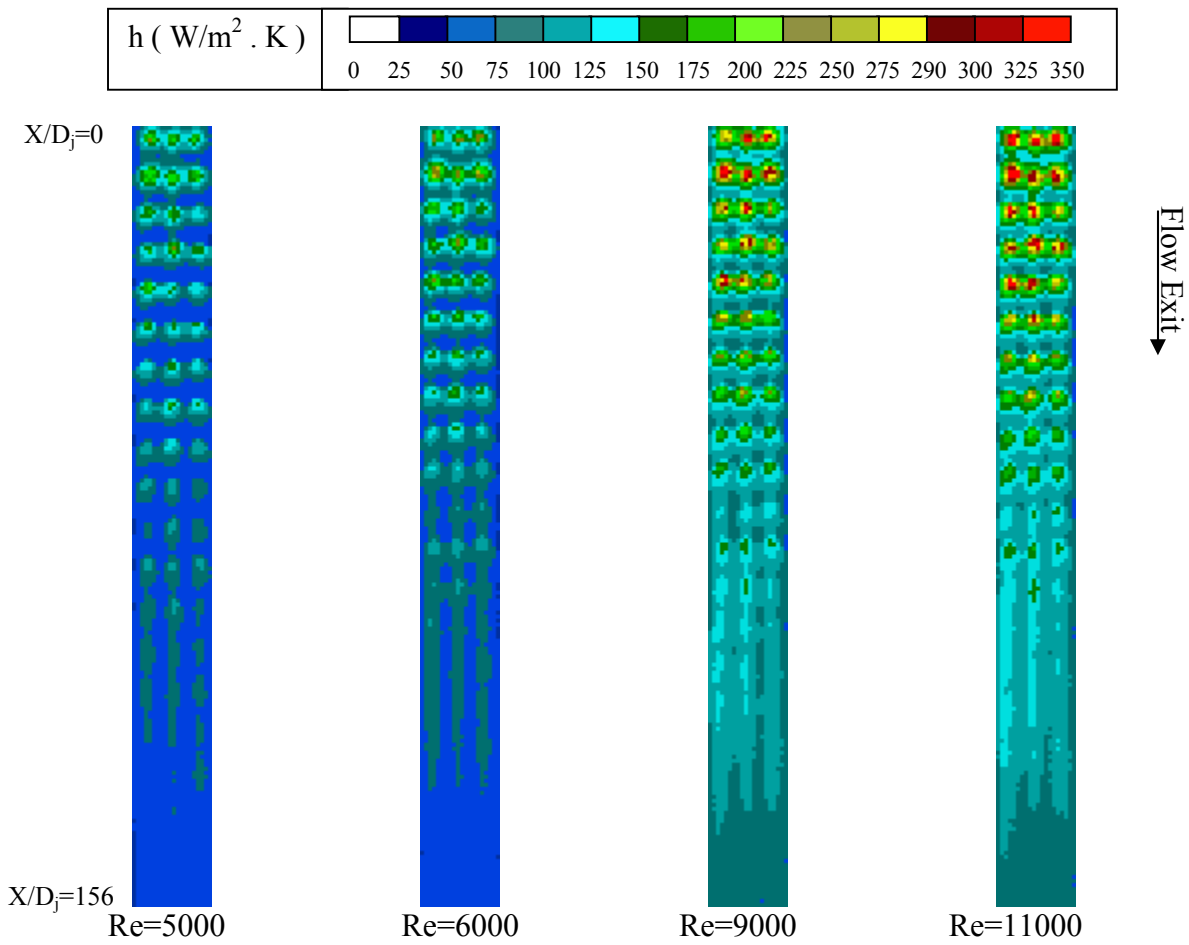


Figure 6.13 Local heat transfer coefficient for target plate with 54 hole and $H/D_j = 4$.

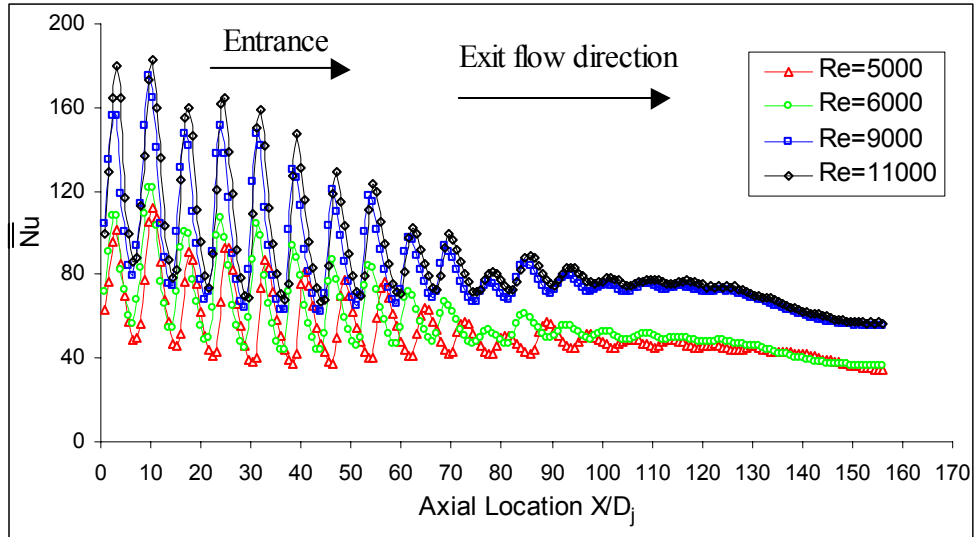


Figure 6.14 Span-averaged Nusselt number for target plate with 54 hole and $H/D_j = 4$.

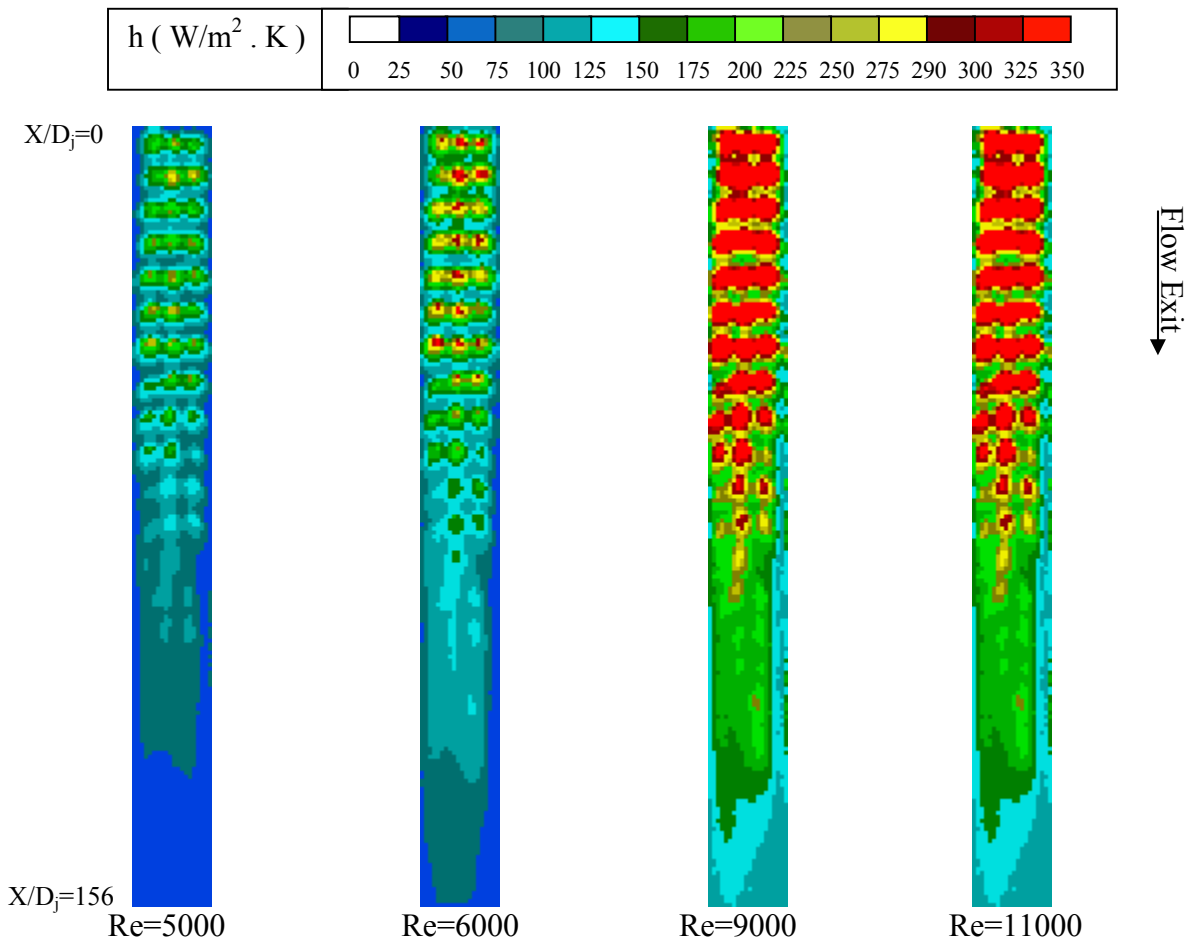


Figure 6.15 Local heat transfer coefficient for target plate with 54 hole and $H/D_j = 6$.

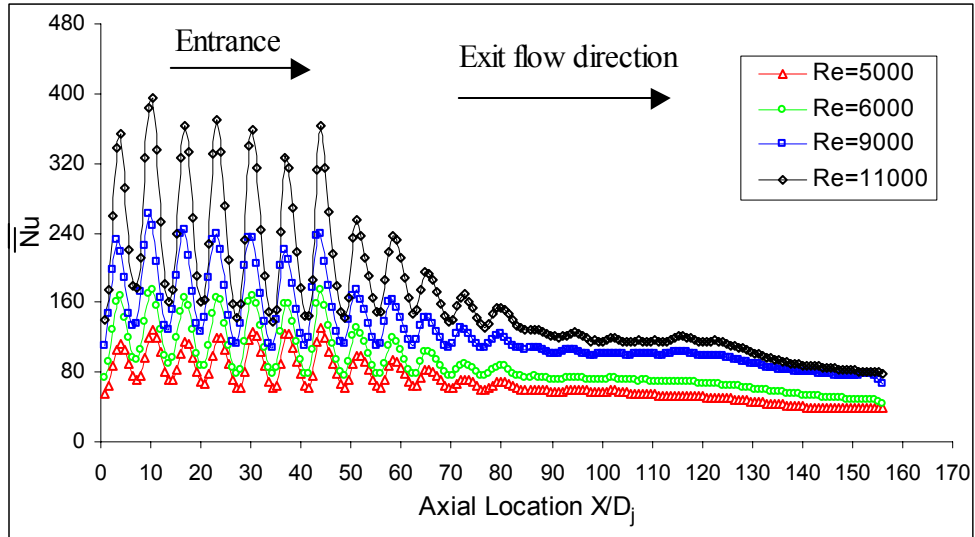


Figure 6.16 Span-averaged Nusselt number for target plate with 54 hole and $H/D_j = 6$.

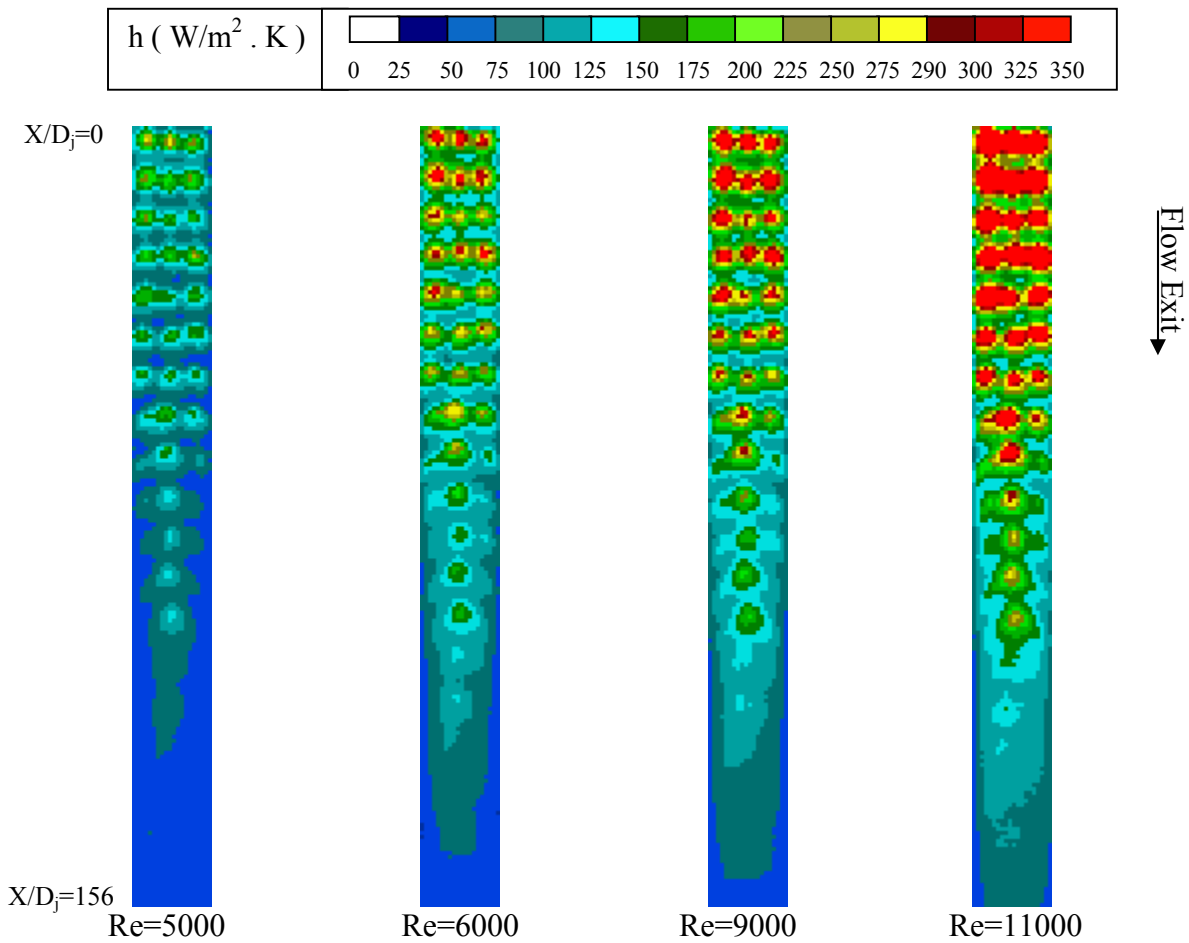


Figure 6.17 Local heat transfer coefficient for target plate with 54 hole and $H/D_j = 8$.

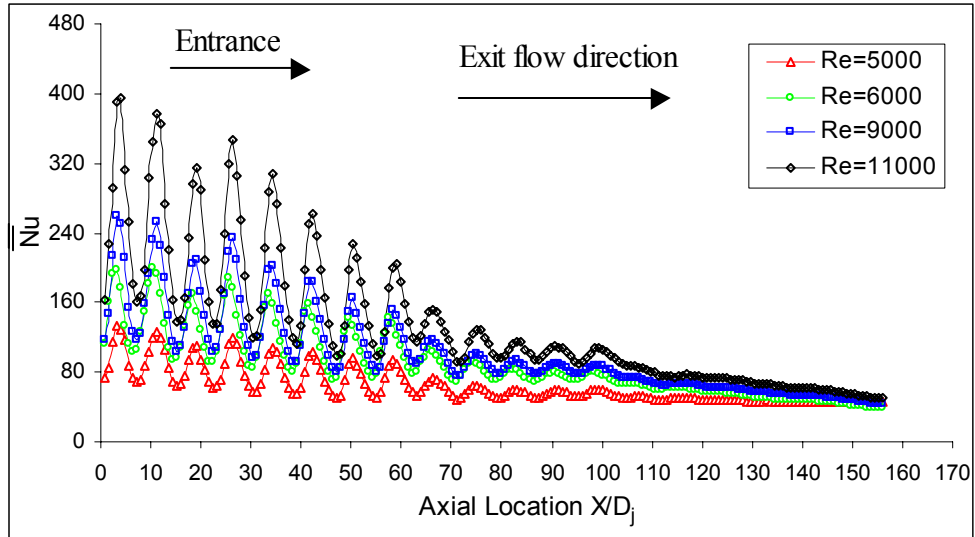


Figure 6.18 Span-averaged Nusselt number for target plate with 54 hole and $H/D_j = 8$.

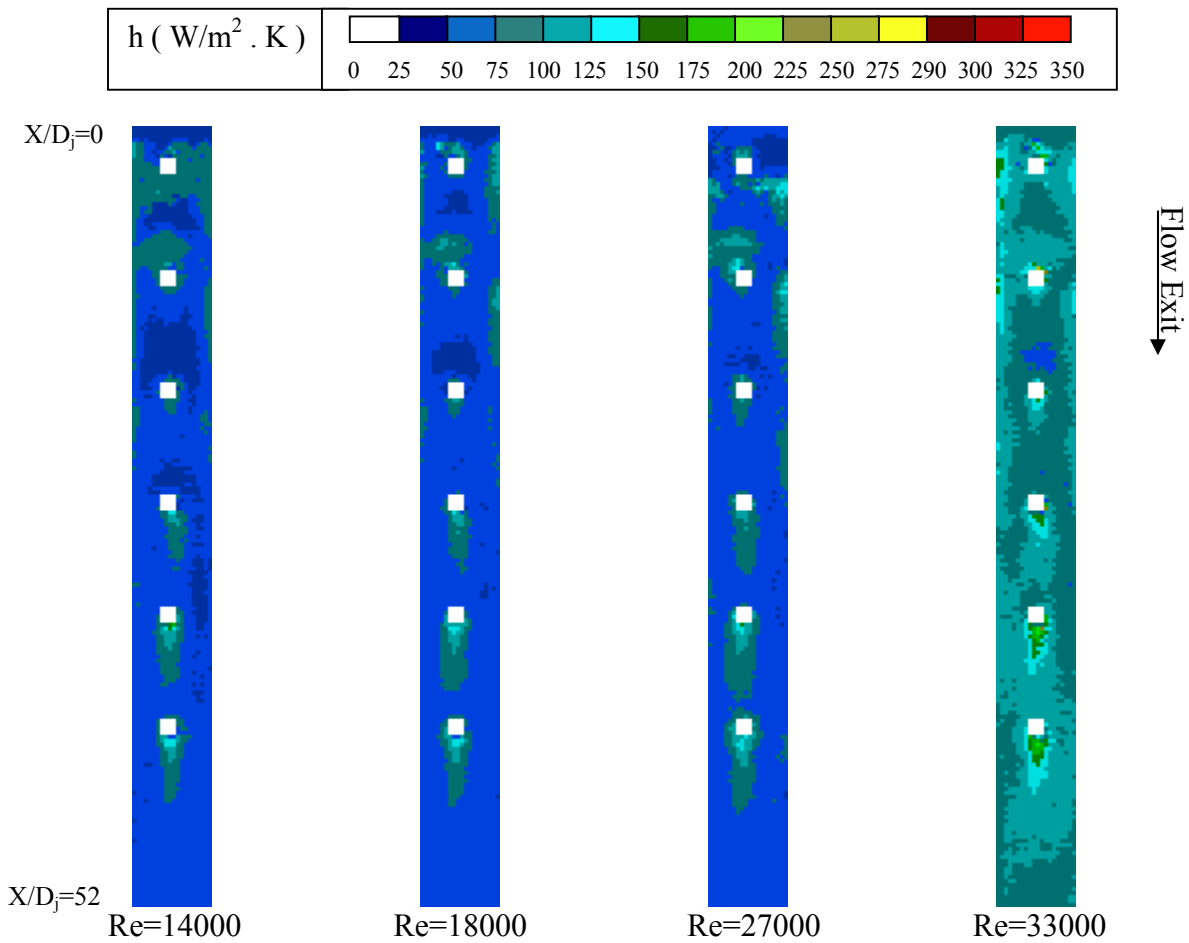


Figure 6.19 Local heat transfer coefficient for jet plate with 6 hole and $H/D_j = 1.33$.

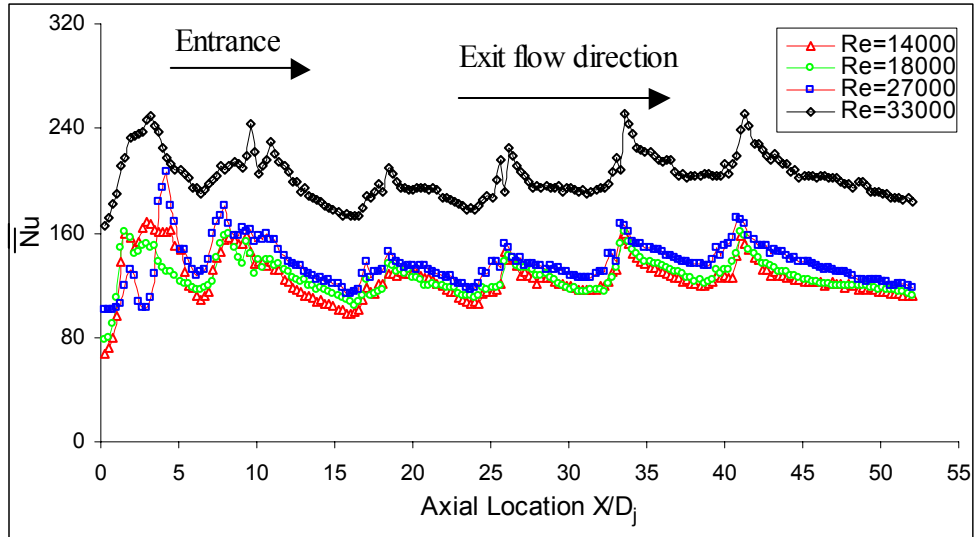


Figure 6.20 Span-averaged Nusselt number for jet plate with 6 hole and $H/D_j = 1.33$.

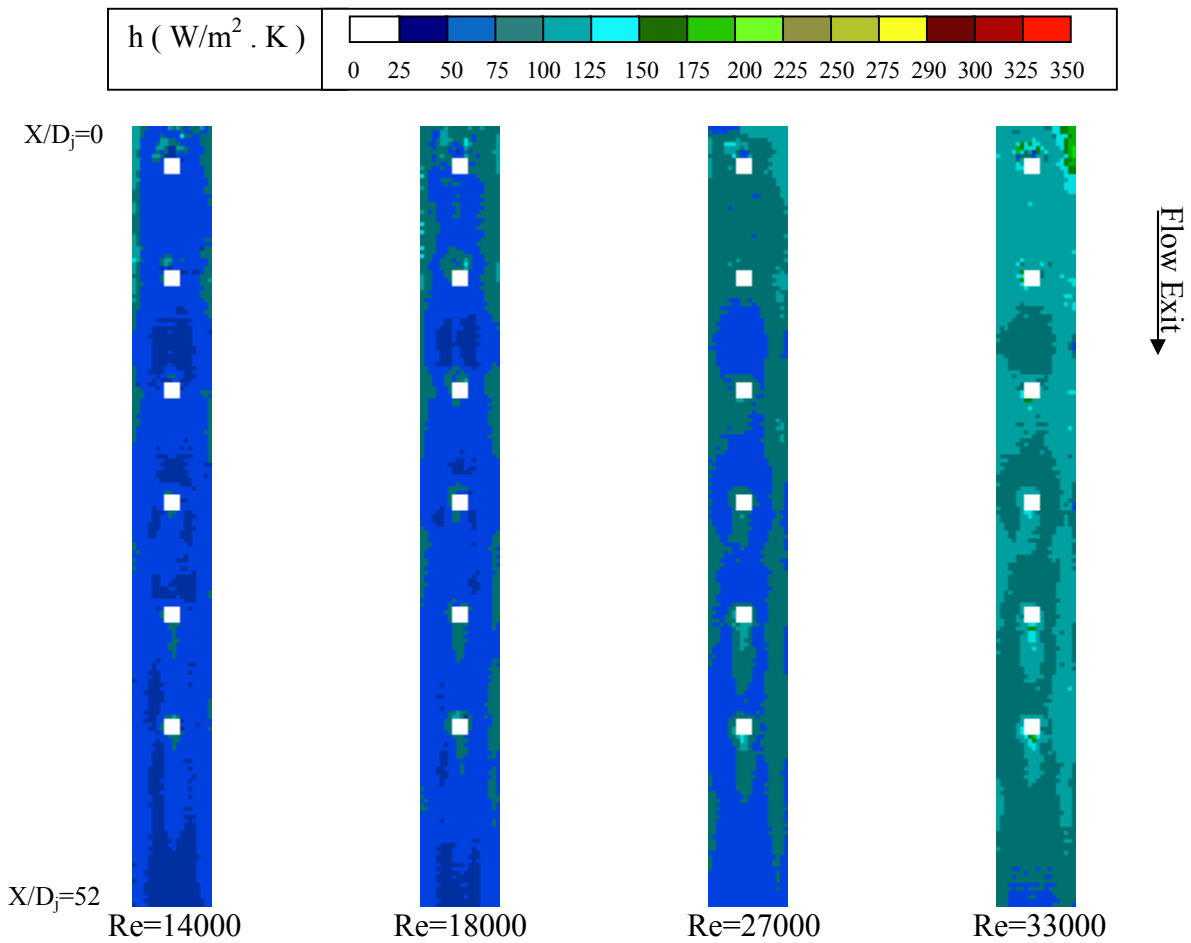


Figure 6.21 Local heat transfer coefficient for jet-issuing plate with 6 hole and $H/D_j = 2$.

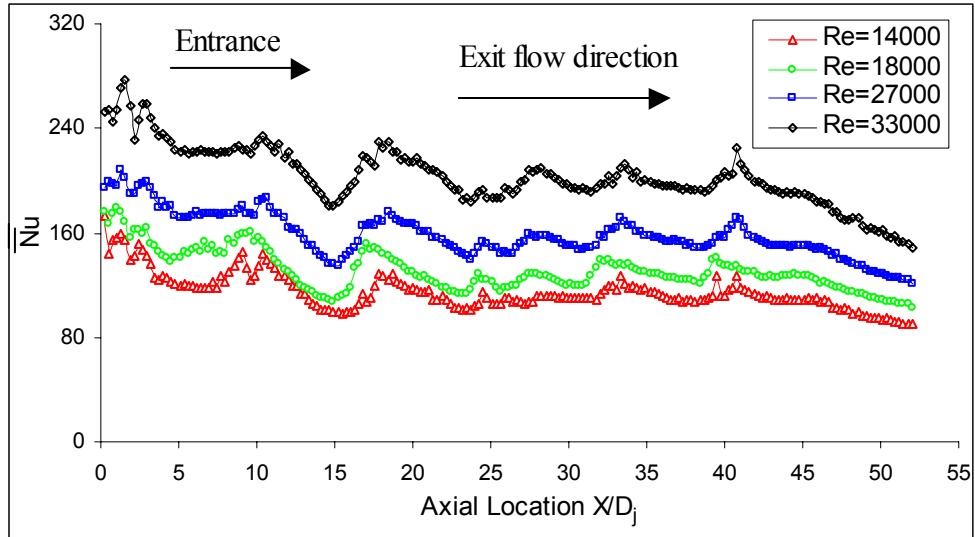


Figure 6.22 Span-averaged Nusselt number for jet-issuing plate with 6 hole and $H/D_j = 2$.

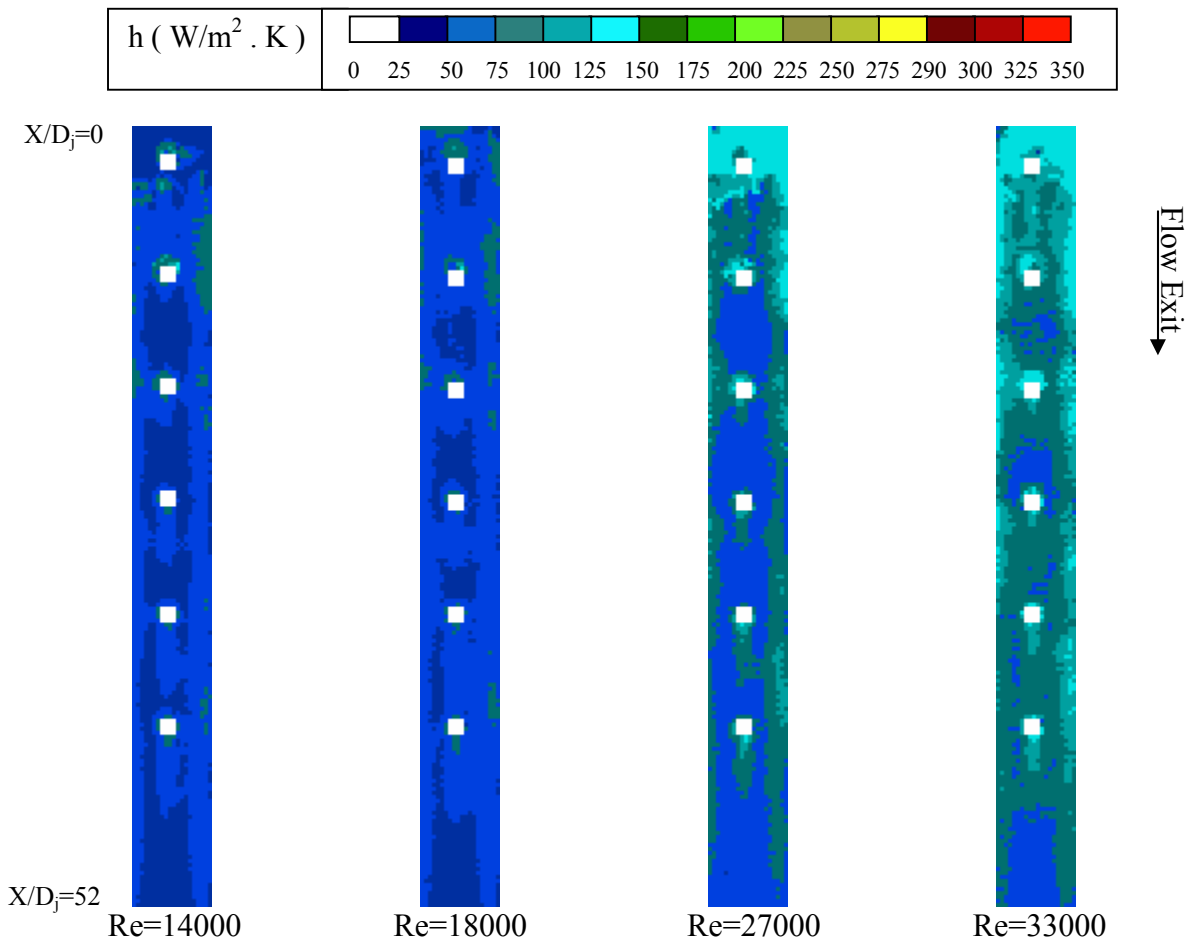


Figure 6.23 Local heat transfer coefficient for jet plate with 6 hole and $H/D_j = 2.67$.

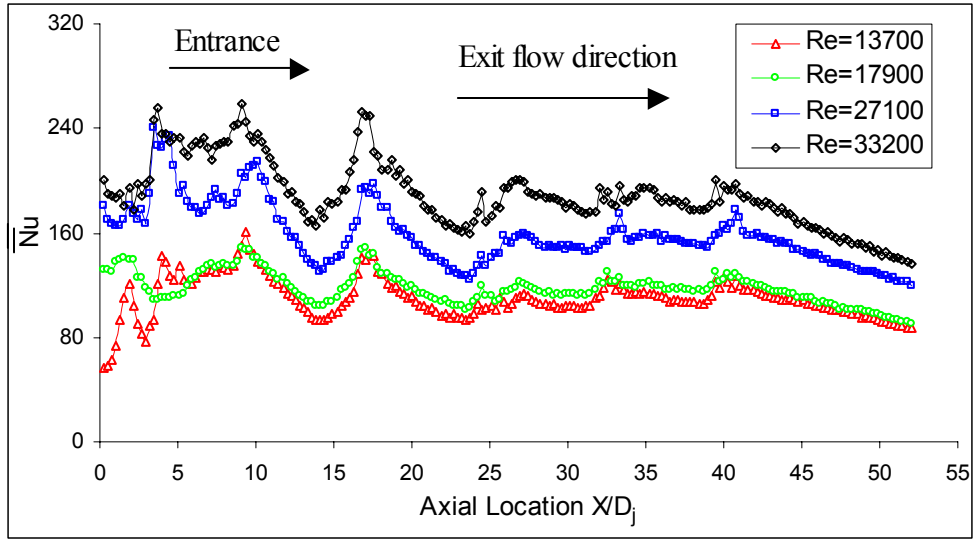


Figure 6.24 Span-averaged Nusselt number for jet plate with 6 hole and $H/D_j = 2.67$.

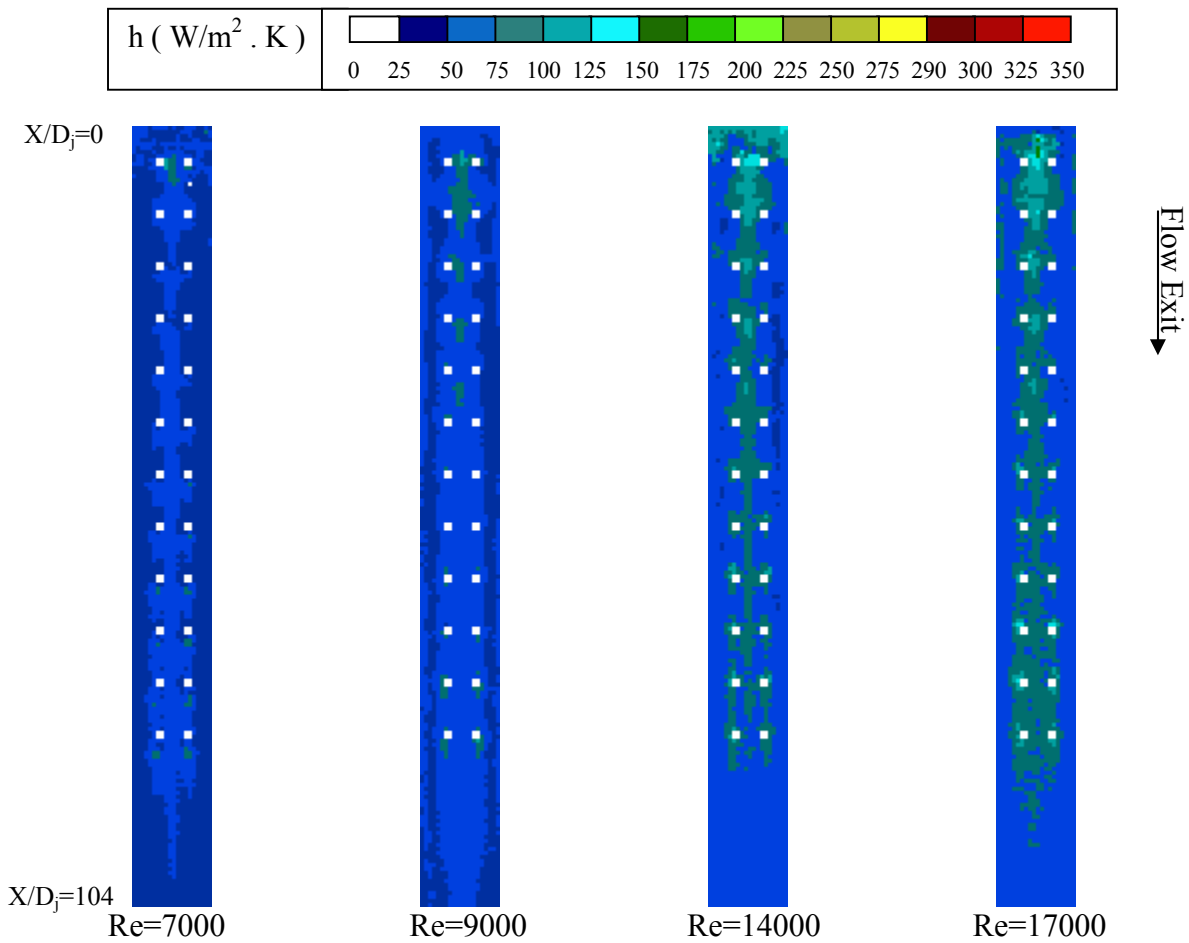


Figure 6.25 Local heat transfer coefficient for jet plate with 24 hole and $H/D_j = 2.67$.

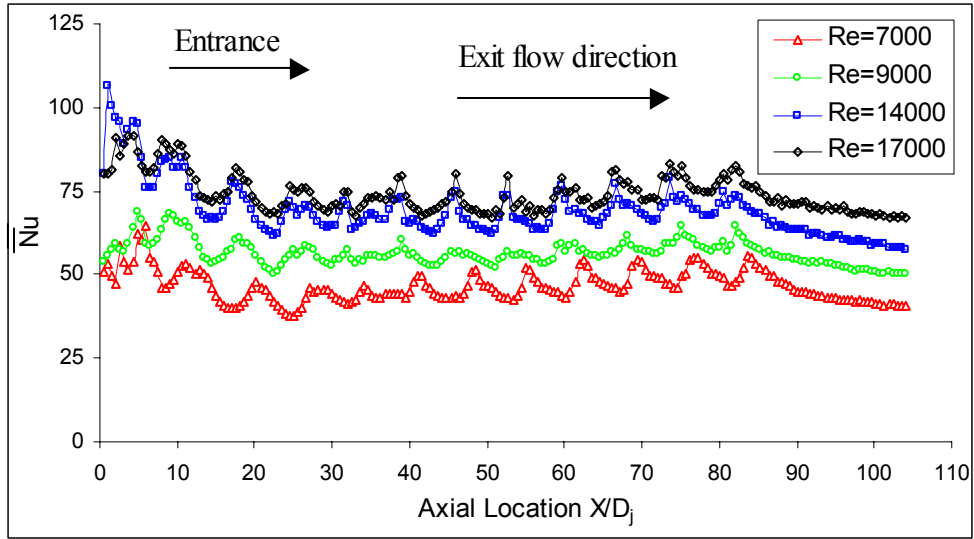


Figure 6.26 Span-averaged Nusselt number for jet plate with 24 hole and $H/D_j = 2.67$.

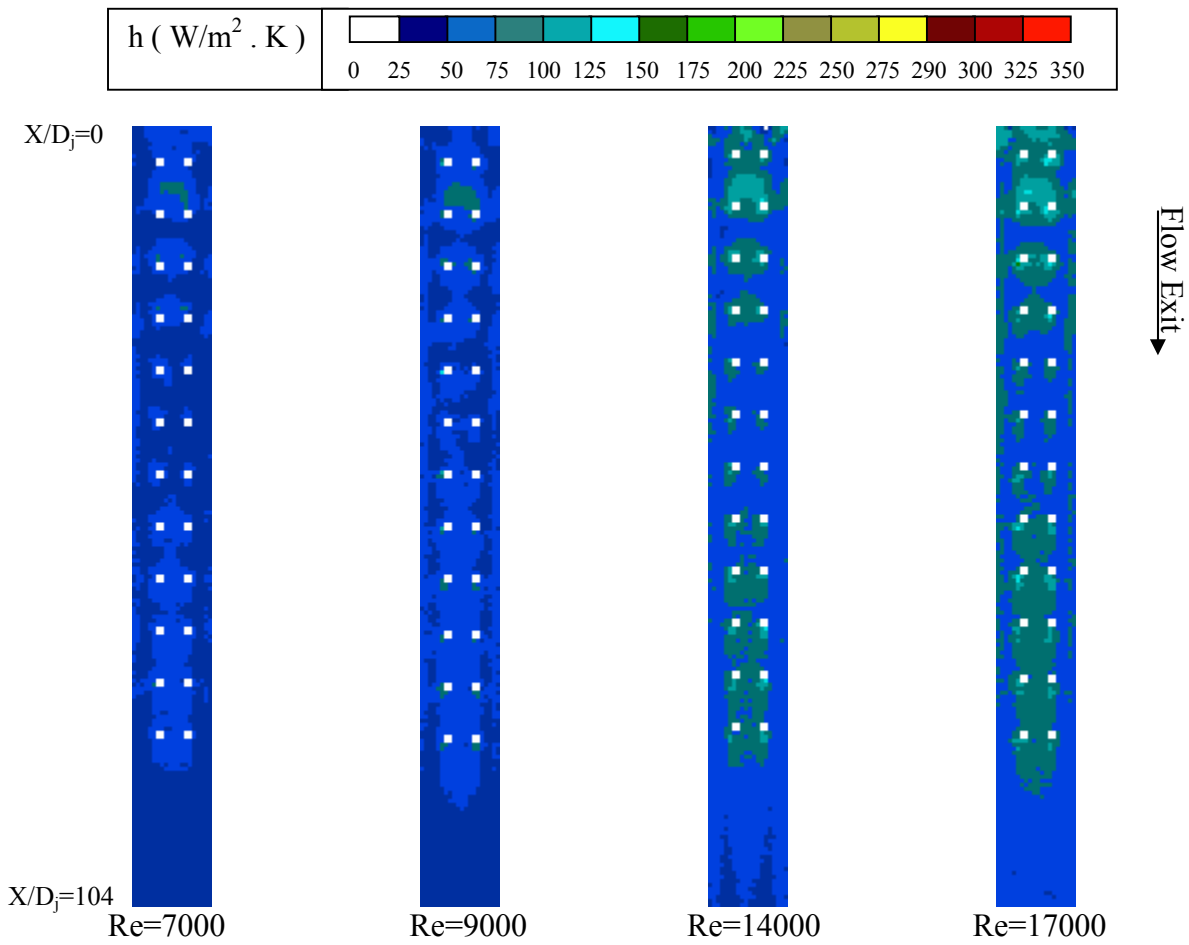


Figure 6.27 Local heat transfer coefficient for jet-issuing plate with 24 hole and $H/D_j = 4$.

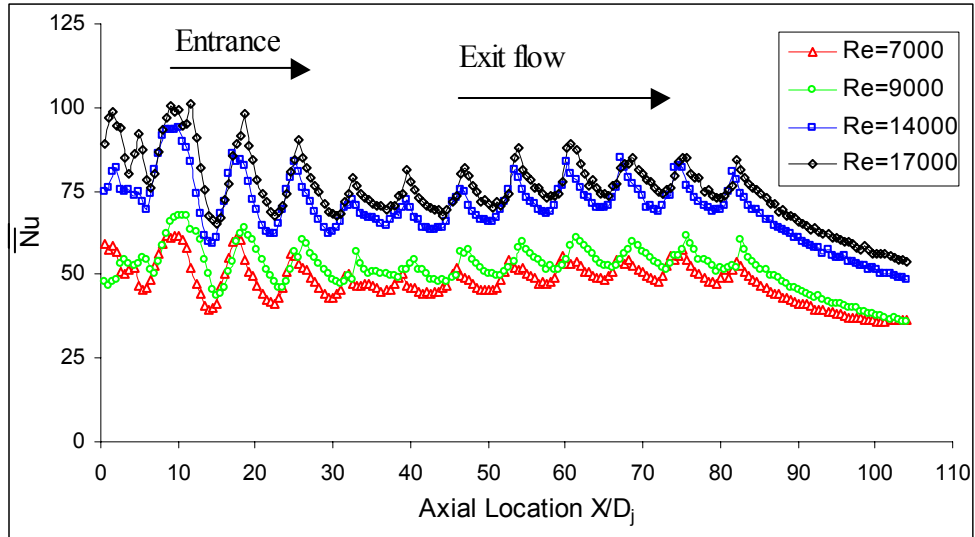


Figure 6.28 Span-averaged Nusselt number for jet plate with 24 hole and $H/D_j = 4$.

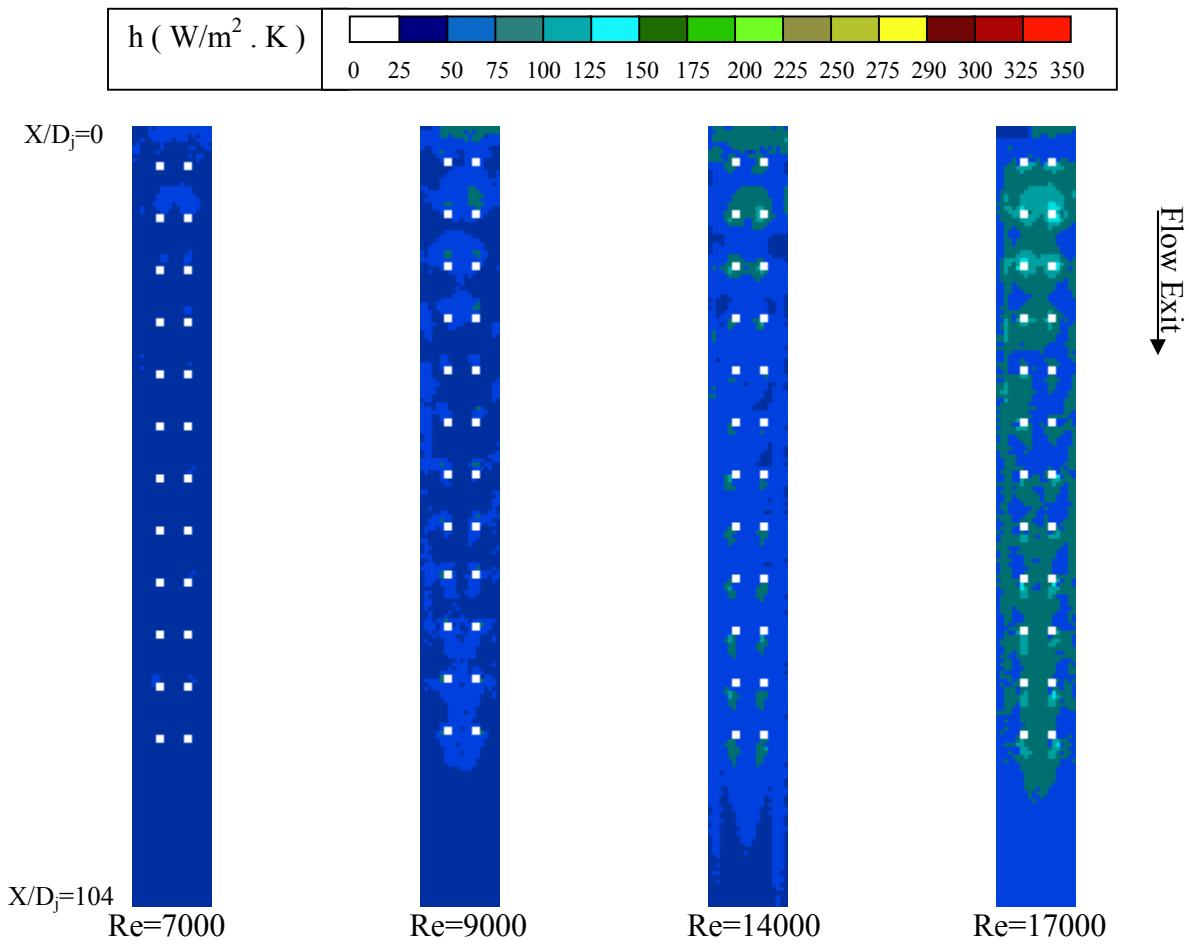


Figure 6.29 Local heat transfer coefficient for jet plate with 24 hole and $H/D_j = 5.33$.

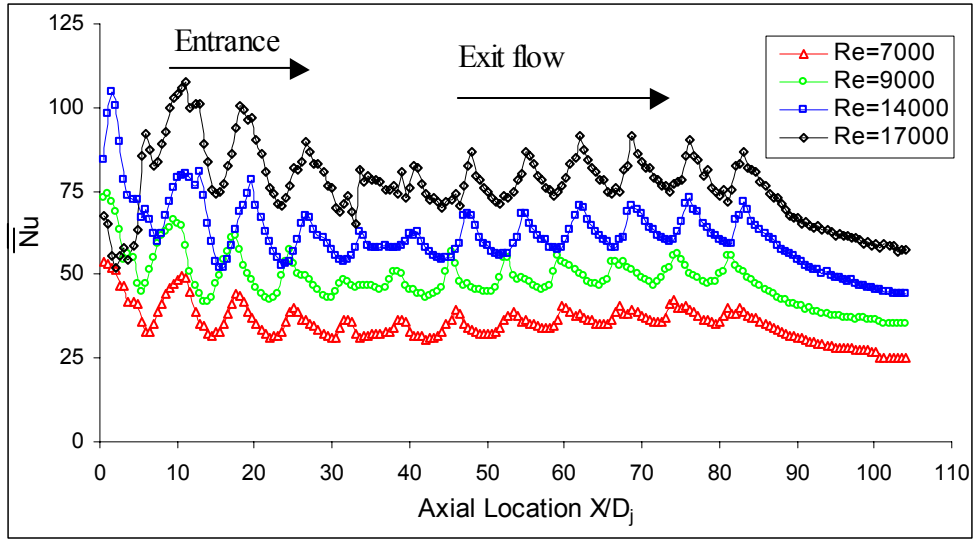


Figure 6.30 Span-averaged Nusselt number for jet plate with 24 hole and $H/D_j = 5.33$.

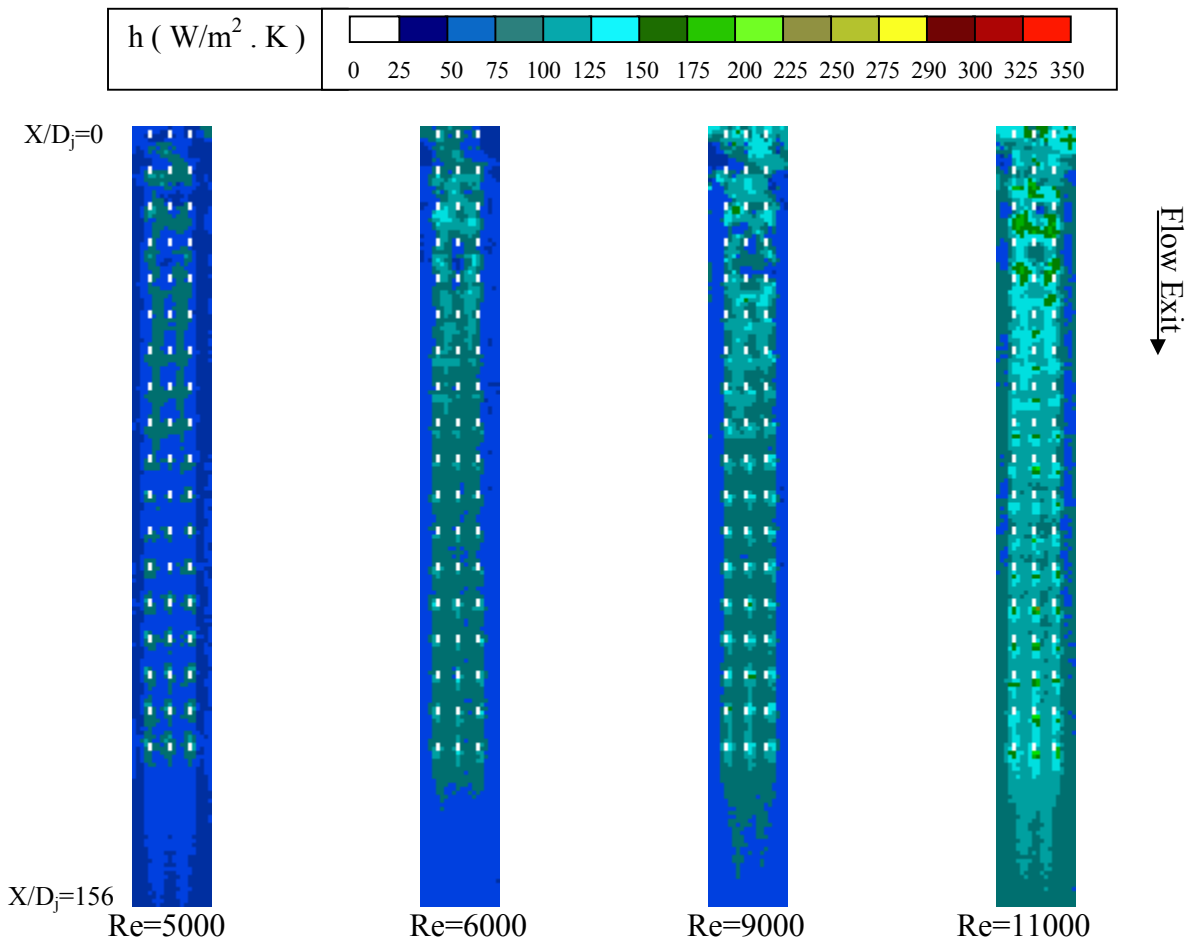


Figure 6.31 Local heat transfer coefficient for jet-issuing plate with 54 hole and $H/D_j = 4$.

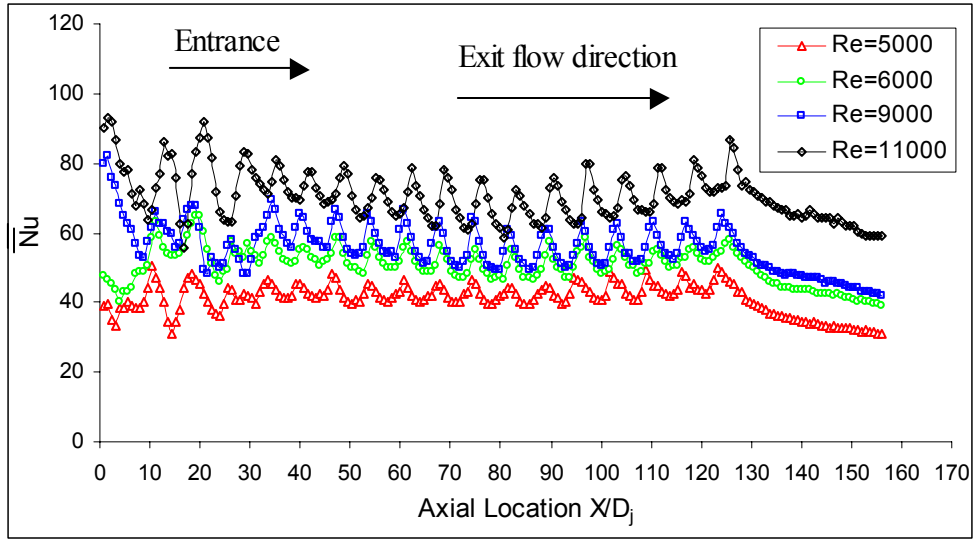


Figure 6.32 Span-averaged Nusselt number for jet plate with 54 hole and $H/D_j = 4$.

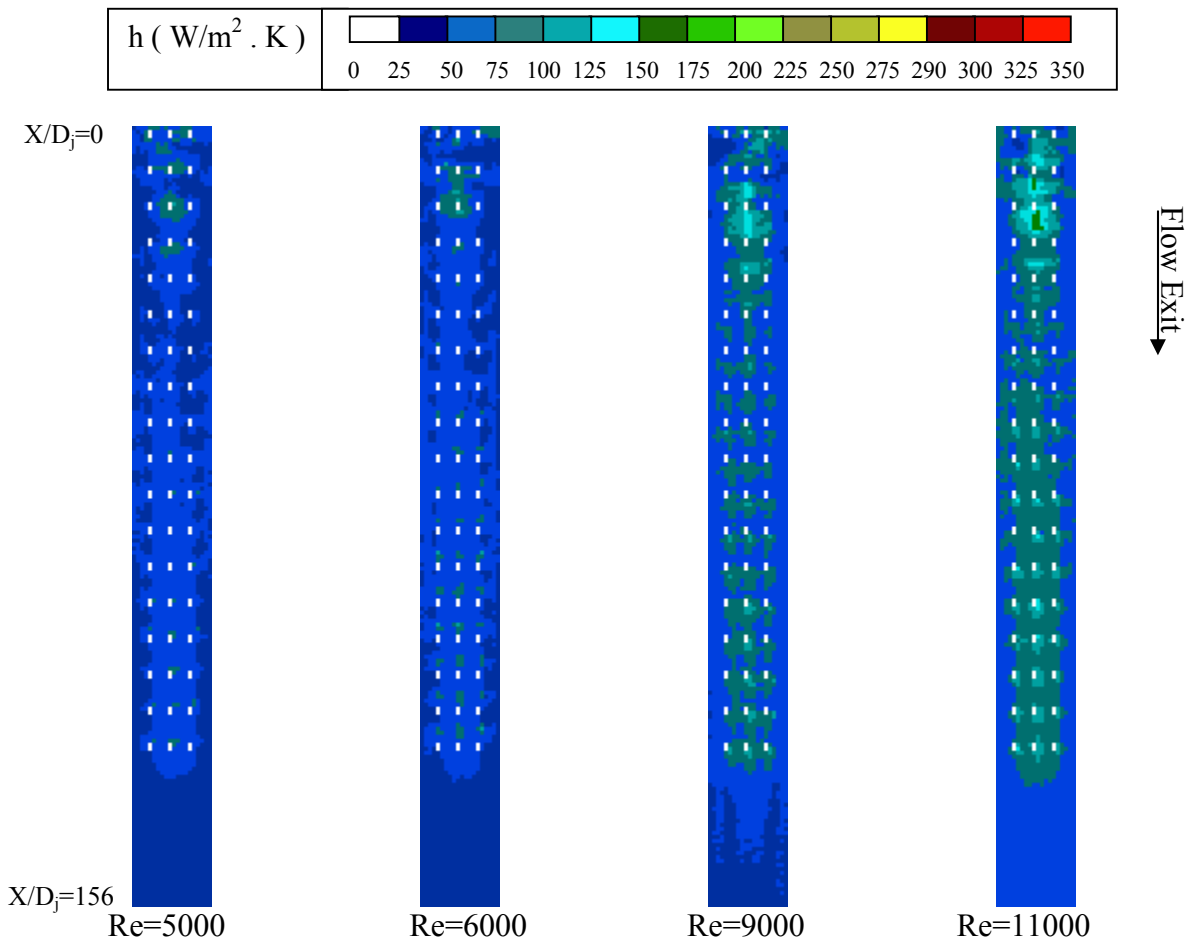


Figure 6.33 Local heat transfer coefficient for jet-issuing plate with 54 hole and $H/D_j = 6$.

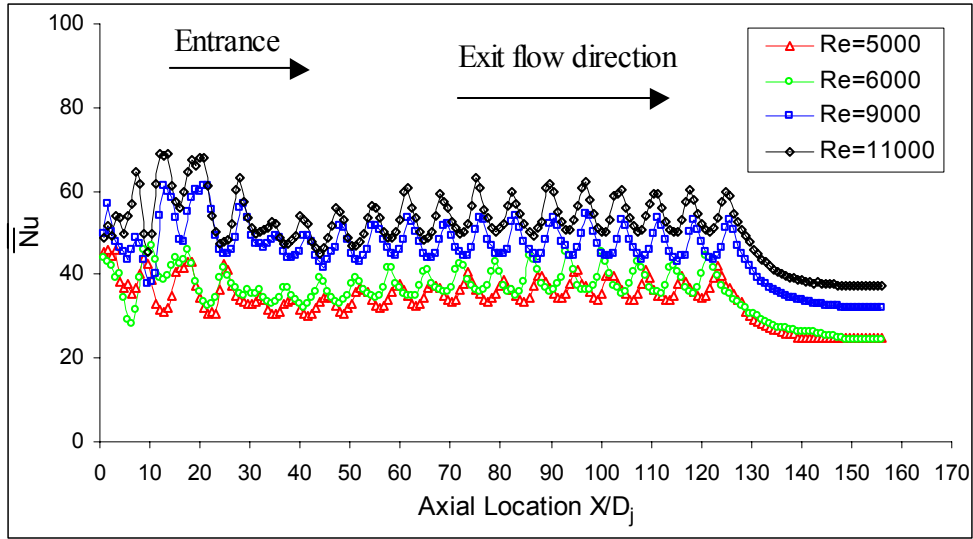


Figure 6.34 Span-averaged Nusselt number for jet plate with 54 hole and $H/D_j = 6$.

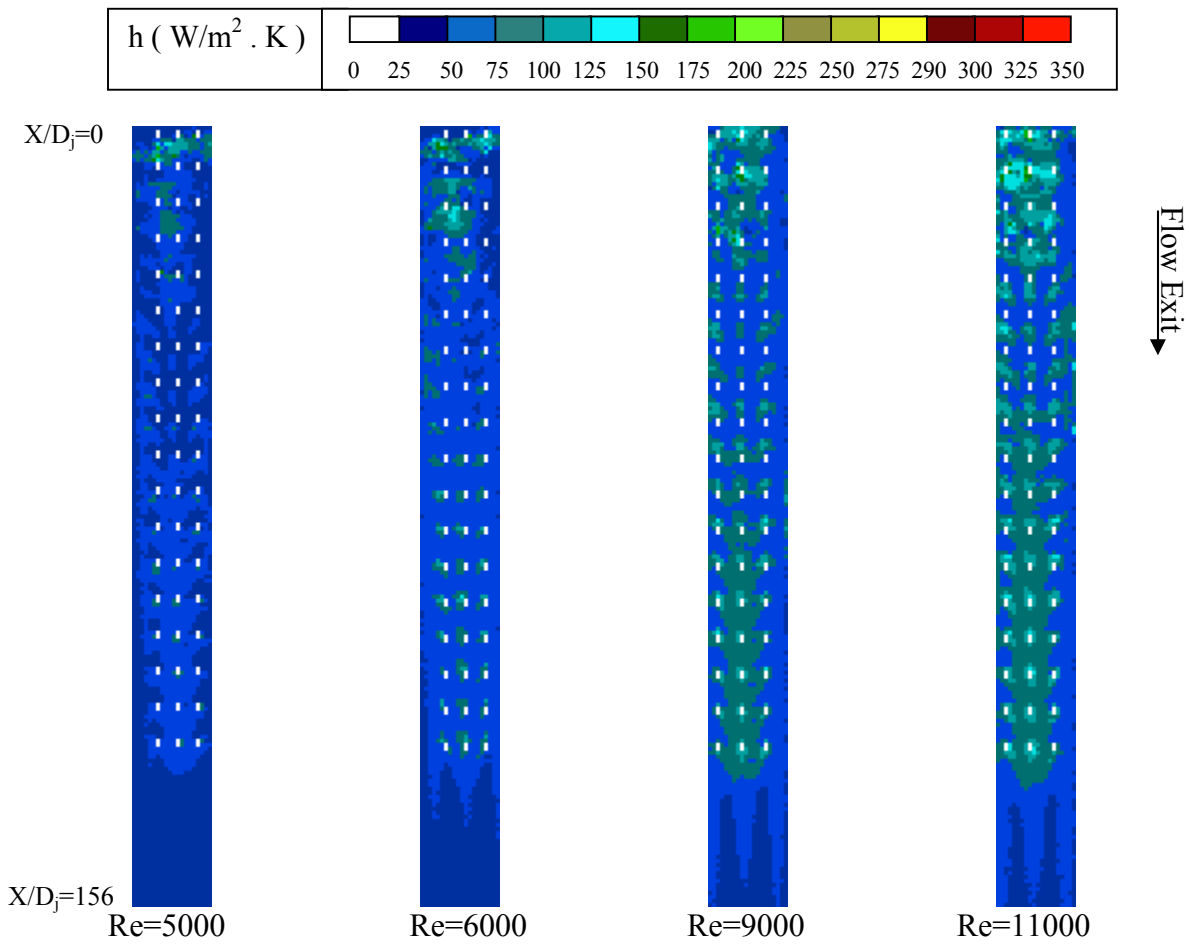


Figure 6.35 Local heat transfer coefficient for jet-issuing plate with 54 hole and $H/D_j = 8$.

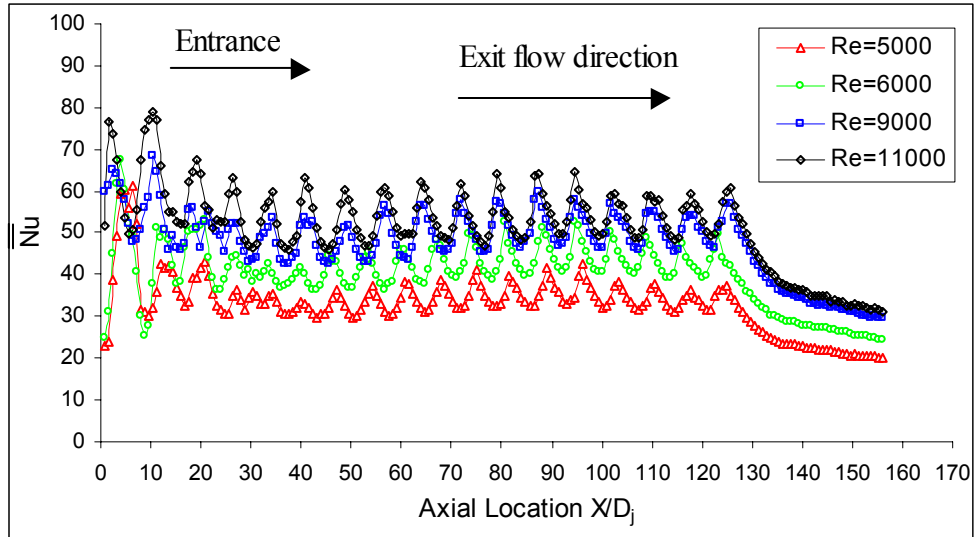


Figure 6.36 Span-averaged Nusselt number for jet plate with 54 hole and $H/D_j = 8$.

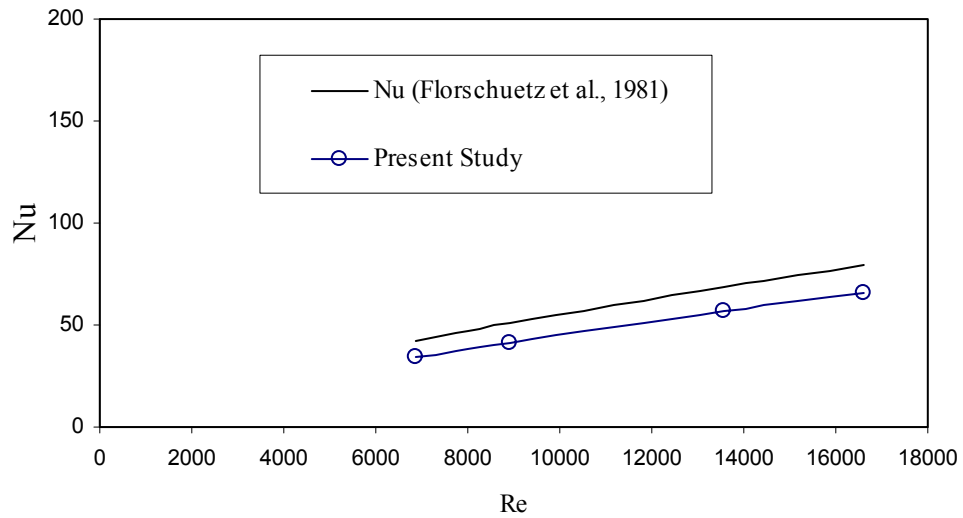


Figure 6.37 Overall-averaged Nusselt number for 24-hole target plate.

6.3 Overall-Averaged Nusselt Number

Figure 6.37 depicts the test results for the overall average Nusselt number for the 24-hole target plate at four Reynolds numbers tested. The heat transfer coefficient was converted into a nondimensional heat transfer coefficient, the Nusselt Number (Nu) to give a more general interpretation. The Nusselt number is defined as

$$\text{Nu} = \frac{hD_j}{k} \quad (6.3)$$

Florschuetz et al. (1981) showed a well-known correlation for the heat transfer of an impinging jet with a cross-flow effect similar to that of the current study,

$$\text{Nu} = 0.068\text{Re}^{0.727} \quad (6.4)$$

The correlation is plotted as a solid line in Figure 6.37 for comparison. The correlation has been widely used in cooling designs in the industry and compared by many other researchers.

As indicated in Figure 6.37, the overall average of the Nusselt number of the current study fits well with those predicted from the correlation, with a maximum discrepancy of only 18% of Florschuetz' correlation. Considering the difference in test rigs and thermal boundary conditions, the results from both studies agree well with current results, especially at a low Reynolds number. A least-square curve-fitting correlation of the average heat transfer from results of the current study can be expressed as

$$Nu = 0.046Re^{0.748} \quad (6.5)$$

Figure 6.38 illustrates the heat transfer enhancement over a fully developed flow in a smooth channel at the same Reynolds number. A modified Dittus-Boeltet equation,

$$Nu_0 = 0.023Re^{0.8}Pr^{0.4} \quad (6.6)$$

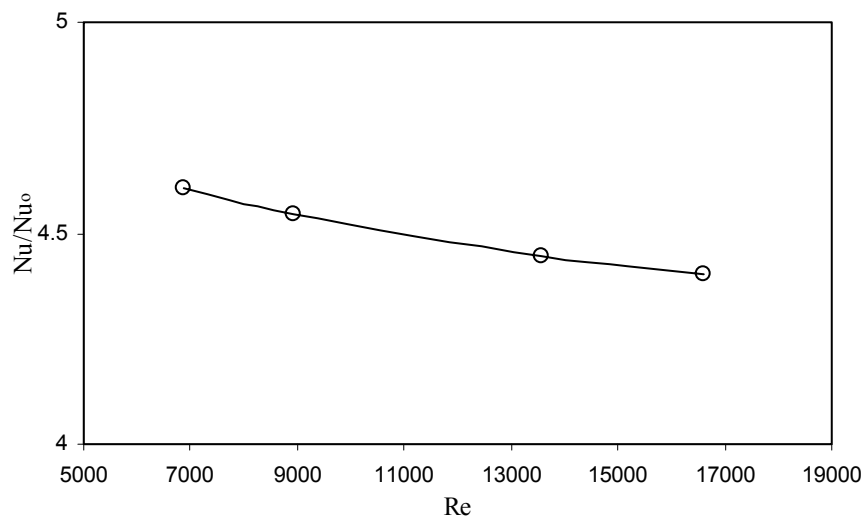


Figure 6.38 Heat transfer enhancement over developed flow in channel.

was used to estimate the heat transfer for fully developed flow in a smooth channel. Note in Eq. (6.7), the Nusselt number and Reynolds number are defined as

$$Nu_0 = \frac{hD_h}{k} \quad (6.7)$$

and

$$\text{Re}_0 = \frac{\bar{u}D_h}{\nu}, \quad (6.8)$$

respectively. These definitions are different from those used in the current study. A conversion had to be made to make a meaningful comparison. In fact, Re_0 , which is based on the mean velocity and channel hydraulic diameter, can be related to Re as

$$\begin{aligned} \text{Re}_0 &= \frac{\bar{u}D_h}{\nu} \\ &= \frac{\dot{m}D_h}{\rho A \nu} \\ &= \frac{\dot{m}}{\rho \nu} \cdot \frac{D_h}{A} \cdot \frac{A_{\min} D_j}{A_{\min} D_j} \\ &= \frac{\dot{m} D_j}{\rho A_{\min} \nu} \cdot \frac{D_h}{D_j} \cdot \frac{A_{\min}}{A} \\ &= \frac{D_h}{D_j} \cdot \frac{A_{\min}}{A} \cdot \text{Re} \end{aligned} \quad (6.9)$$

where A is the cross sectional area of the channel and A_{\min} is the minimum open area in the test section. Nu_0 can be expressed as function of a Nu , such that

$$\begin{aligned} \text{Nu}_0 &= \frac{hD_h}{k} \\ &= \frac{hD_h}{k} \cdot \frac{D_j}{D_j} \\ &= \frac{hD_j}{k} \cdot \frac{D_h}{D_j} \\ &= \text{Nu} \cdot \frac{D_h}{D_j} \end{aligned} \quad (6.10)$$

As depicted in Figure 6.38, the enhancement of heat transfer over a smooth channel flow decreases from 4.4 to 4.6 as the Reynolds number increases. Figures 6.39-6.44 represent the ratio of area-averaged Nusselt number to fully developed Nusselt numbers in the smooth channel for the 6-, 24-, and 54-hole target and jet-issuing plates for $H/D_j = 1.33\sim 8$ for the entire surface of the plates.

The magnitude of Nu/Nu_0 decreases exponentially as the Reynolds number increases for all the results except for the 24-hole target plate at ($H/D_j = 4$ and 5.33) and the 54-hole target plate at $H/D_j = 6$. The values of the Nusselt number for the 6-hole target plate are higher than those of the fully developed Nusselt number in the smooth channel by a factor of 1.3-2.6.

It is clear from Figure 6.39 that the heat transfer increases with an increase in jet-to-target plate spacing. With an increase in this distance, the cross-flow gets more space to develop, and therefore the deflection of the impingement jet is less. On the other hand, the values of the Nusselt number for the 24-hole target plate are higher than those of the fully developed Nusselt number by a factor of 3.4-4.6. In Figure 6.40, it can be seen that the heat transfer increases as jet-to-target plate spacing decreases. The 54-hole target plate results are higher than those of the fully developed Nusselt number in the smooth channel by a factor of 2.2-5.4. The maximum heat transfer of the 54-hole target plate occurs at jet-to-target plate distance $X/D_j = 6$ (see Figure 6.41).

Figure 6.42 shows that the magnitude of Nu/Nu_0 decreases exponentially with the Reynolds number. The values of the Nusselt number for the 6-hole jet issuing plate vary by 0.7-1.7 compared to those of the fully developed Nusselt number in the smooth channel, and the heat transfer is more uniform than the target plate. The heat transfer increases as the

space between the jet-issuing plate and the target plate increase. With an increase in this distance, the cross-flow gets more space to develop, and therefore the interaction of the impingement jet and the cross-flow is strong. For the 24-hole jet-issuing plate (see Fig. 6.43), the heat transfer varies by 1-1.5 compared to the fully developed Nusselt number. On the other hand, the values of the Nusselt number for the 54-hole jet-issuing plate are higher than those of the fully developed Nusselt number by a factor of 1.5-2.7 (see Fig. 6.44).

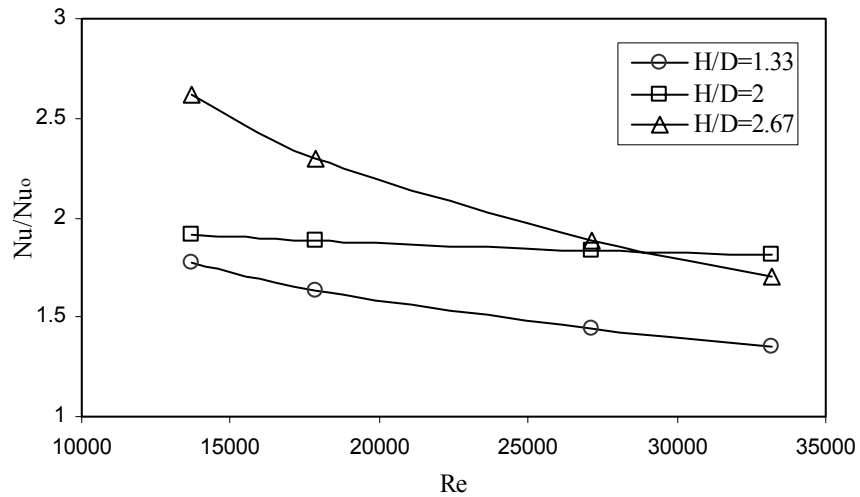


Figure 6.39 Heat transfer enhancement over developed flow for 6-hole target plate.

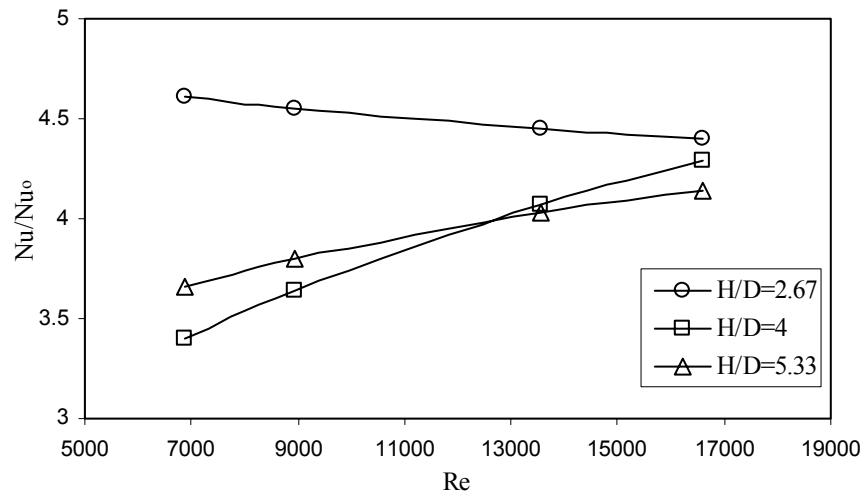


Figure 6.40 Heat transfer enhancement over developed flow for 24-hole target plate.

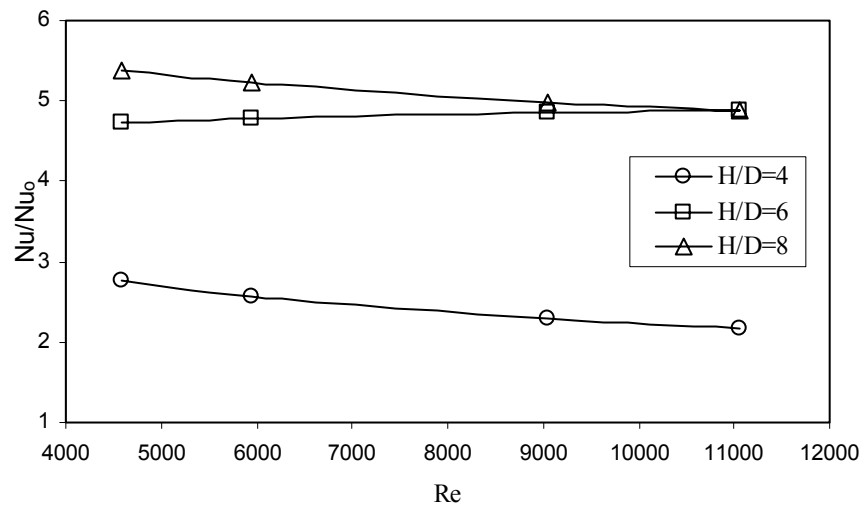


Figure 6.41 Heat transfer enhancement over developed flow for 54-hole target plate.

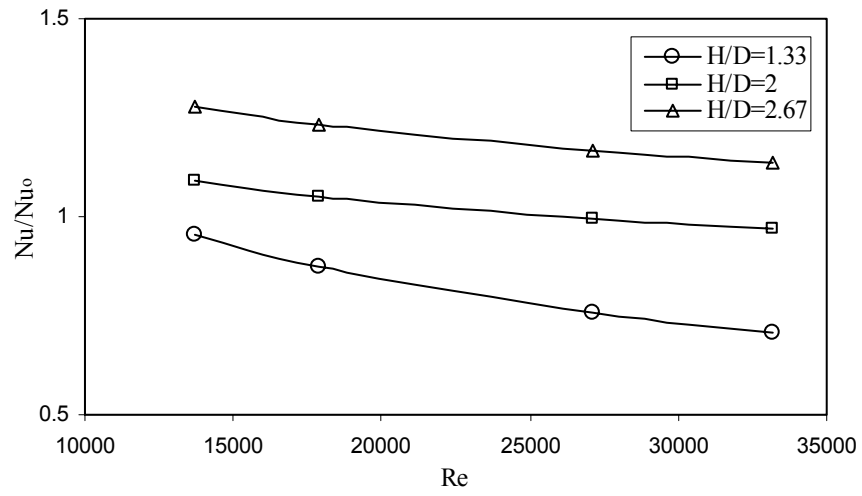


Figure 6.42 Heat transfer enhancement over developed flow for 6-hole jet-issuing plate.

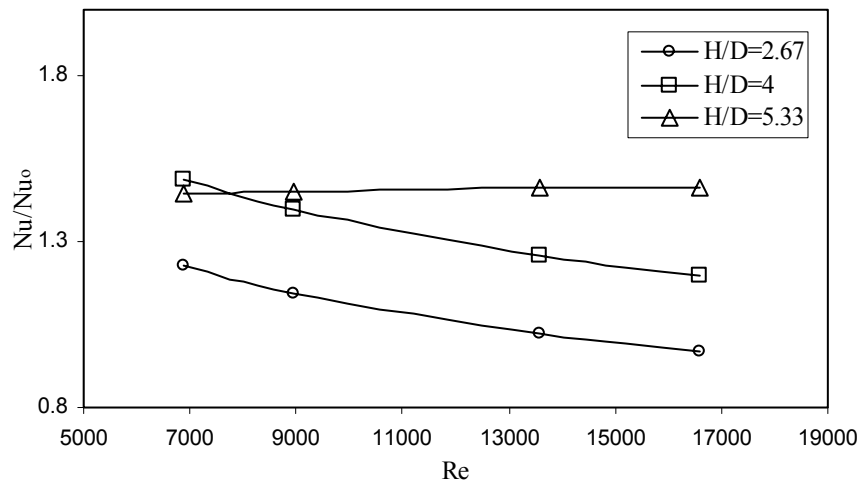


Figure 6.43 Heat transfer enhancement over developed flow for 24-hole jet-issuing plate.

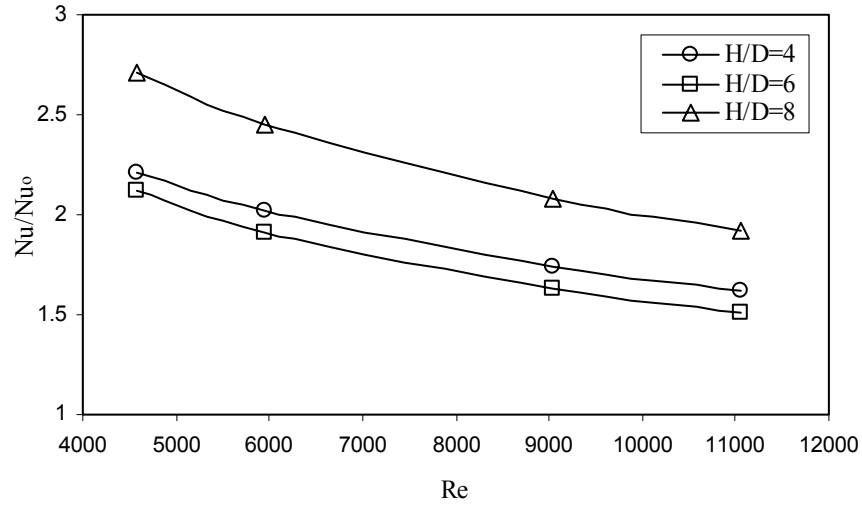


Figure 6.44 Heat transfer enhancement over developed flow for 54-hole jet-issuing plate.

6.4 Row-Resolved Heat Transfer

The heat transfer enhancement is normalized by dividing Nu by Nu_0 , which is predicted from the modified Dittus-Boetler equation for a fully developed internal flow in smooth channel. The area, which is used in calculating the average heat transfer of a row, covers the region from $0.5S_x$ upstream and downstream of the centers of the jet holes in a row, as shown in Figure 6.45.

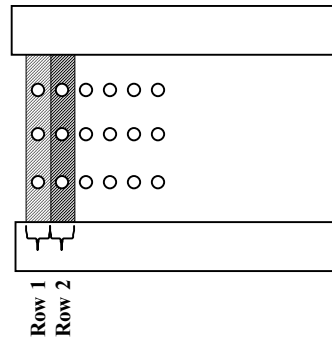


Figure 6.45 Schematic of rows in 54-hole jet-issuing plate.

The area of the holes of the jet-issuing plate was not included in the calculation (i.e., the pixels of the holes area were removed from the results of the jet plate).

In the TLC technique used in the current study, the thermal boundary condition is essentially between the constant wall temperature and constant heat flux. In this technique, the temperature of the entire test section is initially uniform. As the test begins, hot air enters the test section and imposes convective heat transfer. The thermal boundary condition imposed on the surface of the channel wall varies with time as the test proceeds. Because the test section is maintained at a constant initial temperature before the test and the measurements occur over such a short time (normally controlled to be completed within 2 minutes), the temperature changes are in general very small compared to the temperature difference from the flow to the surface. Therefore, the surface will usually appear nearly constant in temperature compared to the convective boundary layer.

Figure 6.47 to 6.64 represent a row-resolved area-averaged heat transfer plot. The following results show the first four rows for the jet-issuing plate and target plate for the 6-, 24-, and 54-hole test sections.

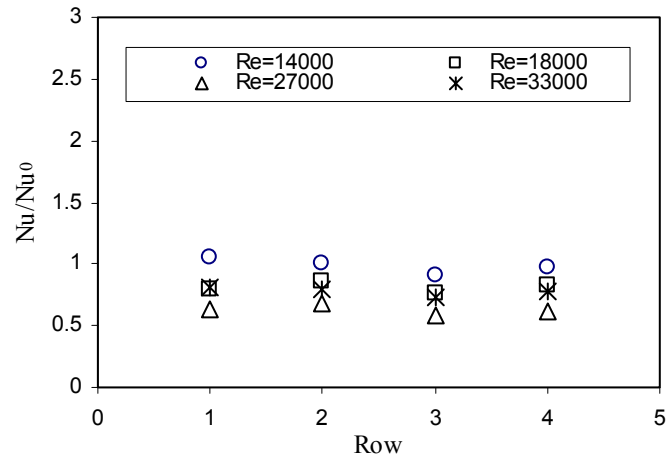


Figure 6.46 Row-resolved overall heat transfer for 6-hole jet plate with $H/D_j = 1.33$.

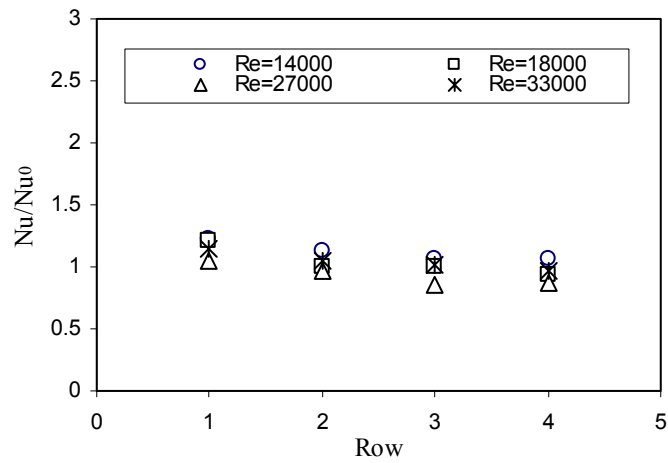


Figure 6.47 Row-resolved overall heat transfer for 6-hole jet plate with $H/D_j = 2$.

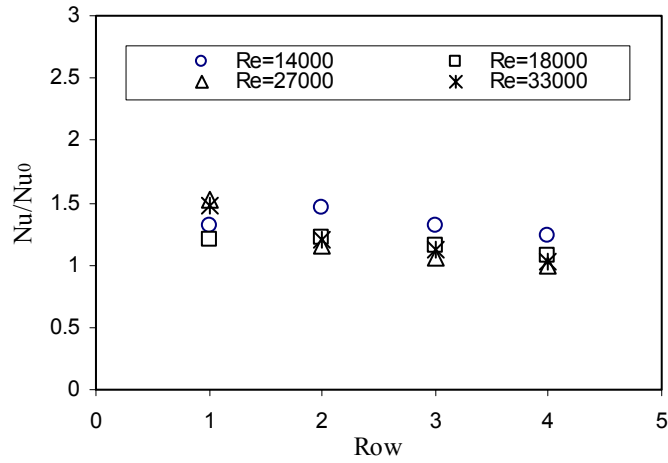


Figure 6.48 Row-resolved overall heat transfer for 6-hole jet plate with $H/D_j = 2.67$

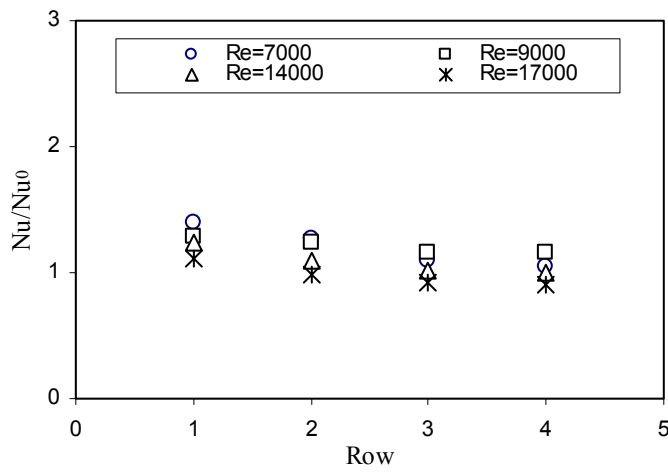


Figure 6.49 Row-resolved overall heat transfer for 24-hole jet plate with $H/D_j = 2.67$.

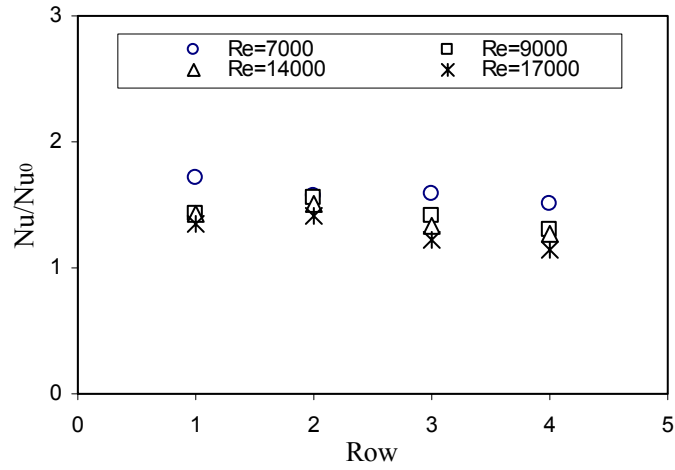


Figure 6.50. Row-resolved overall heat transfer for 24-hole jet plate with $H/D_j = 4$.

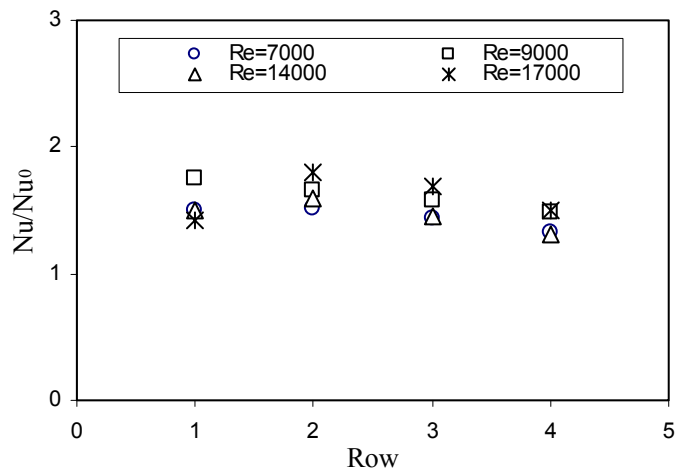


Figure 6.51 Row-resolved overall heat transfer for 24-hole jet plate with $H/D_j = 5.33$

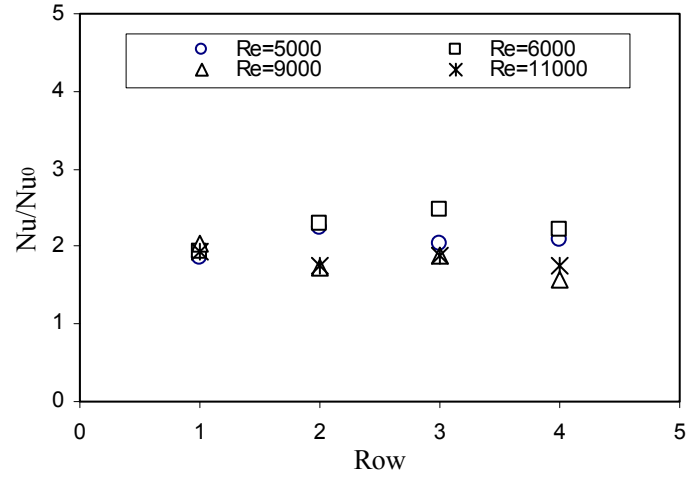


Figure 6.52 Row-resolved overall heat transfer for 54-hole jet plate with $H/D_j = 4$.

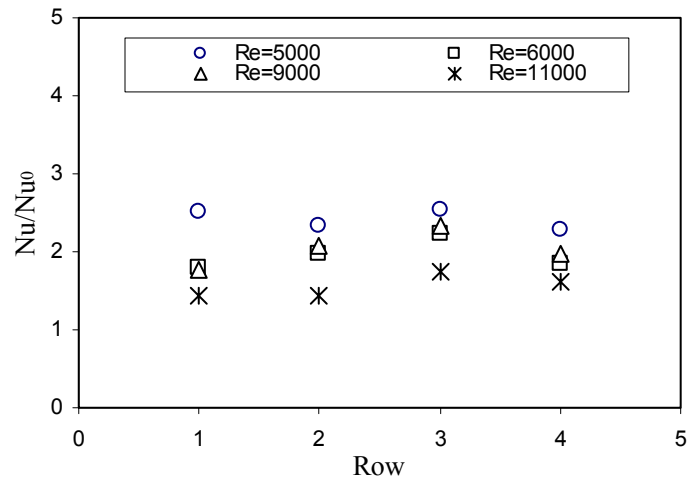


Figure 6.53 Row-resolved overall heat transfer for 54-hole jet plate with $H/D_j = 6$.

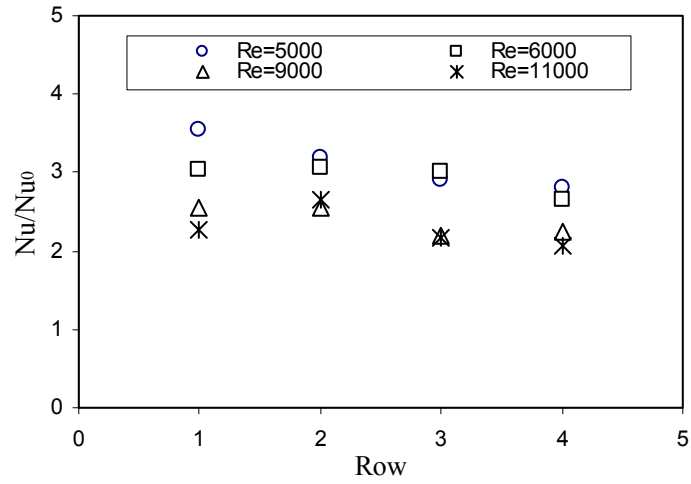


Figure 6.54 Row-resolved overall heat transfer for 54-hole jet plate with $H/D_j = 8$.

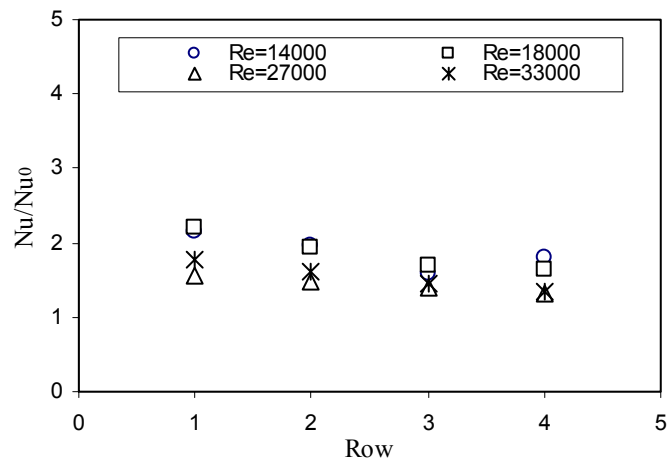


Figure 6.55 Row-resolved overall heat transfer for 6-hole target plate with $H/D_j = 1.33$.

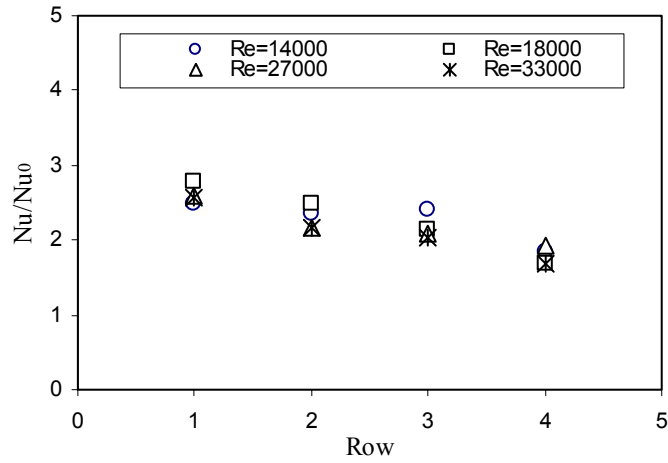


Figure 6.56 Row-resolved overall heat transfer for 6-hole target plate with $H/D_j = 2$.

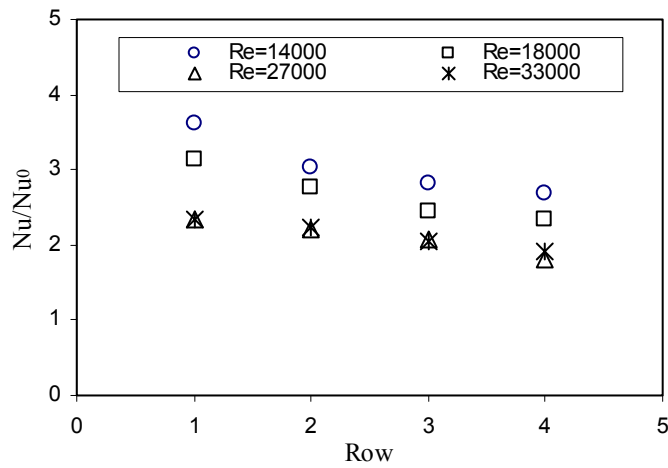


Figure 6.57 Row-resolved overall heat transfer for 6-hole target plate with $H/D_j = 2.67$.

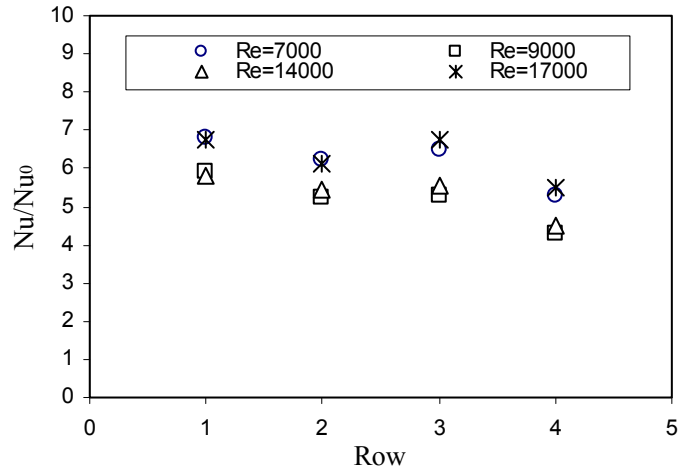


Figure 6.58 Row-resolved overall heat transfer for 24-hole target plate with $H/D_j = 2.67$.

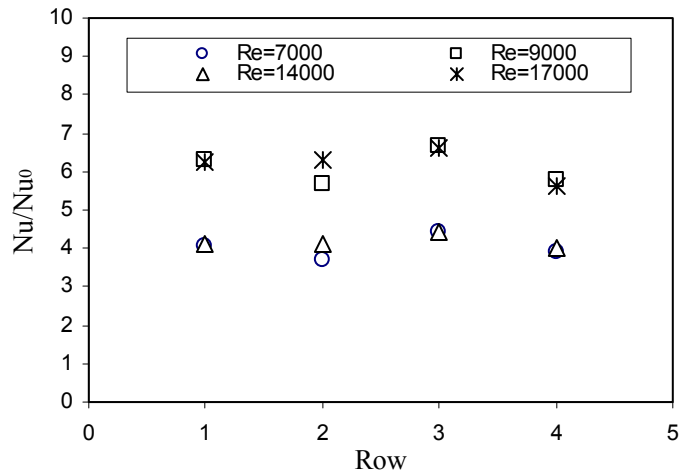


Figure 6.59 Row-resolved overall heat transfer for 24-hole target plate with $H/D_j = 4$

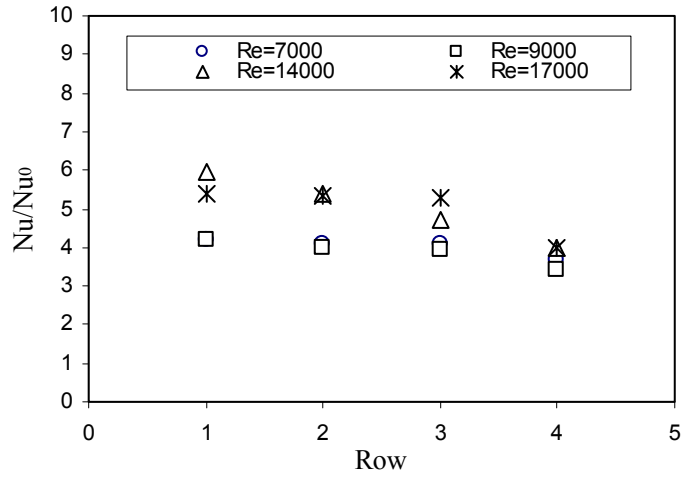


Figure 6.60 Row-resolved overall heat transfer for 24-hole target plate with $H/D_j = 5.33$.

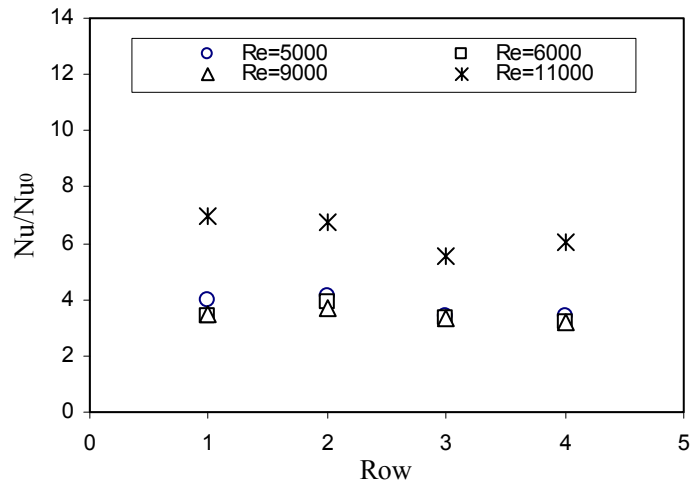


Figure 6.61 Row-resolved overall heat transfer for 54-hole target plate with $H/D_j = 4$.

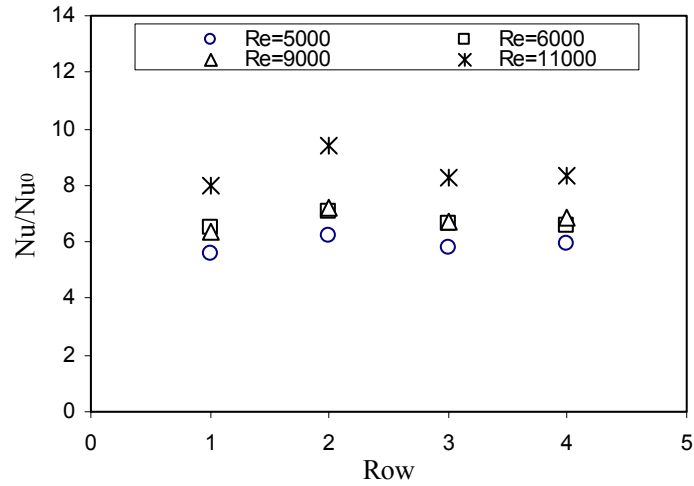


Figure 6.62 Row-resolved overall heat transfer for 54-hole target plate with $H/D_j = 6$.

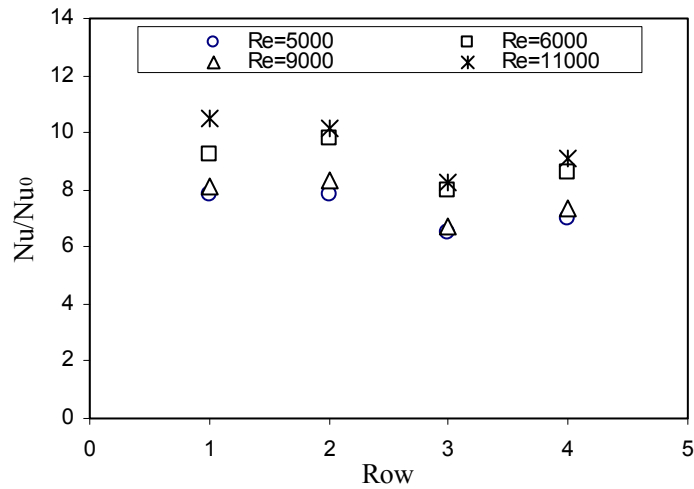


Figure 6.63 Row-resolved overall heat transfer for 54-hole target plate with $H/D_j = 8$.

Figures 6.46–6.63 explain the spanwise-averaged row-resolved heat transfer enhancement for the 6-, 24-, and 54-hole jet-issuing plate and target plate for different jet-to-

target plate distance. Generally, and as shown in these figures, a higher enhancement of heat transfer occurs at a lower Reynolds number.

In Figure 6.46, heat transfer initially started from a low value at the first row to a peak value at the second row, then decreased at the third row and increased at the fourth row. But the heat transfer of the first row was the highest when the Reynolds number was 14,000.

In Figure 6.47, heat transfer starts from a high value at the first row, then decreases, then starts to increase again at the fourth row. Figure 6.48 shows that heat transfer at Reynolds number = 14,000 and 18,000 increases from the low value at the first row and reaches a peak value at the second row, then decreases at the third and fourth rows. At $Re = 27,000$ and $33,000$, heat transfer decreases from the first row to the fourth row.

Heat transfer, as seen in Figure 6.49 decreases from a high value at the first row and becomes almost constant at the third and fourth rows. In Figure 6.50, heat transfer increases from a low value at the first row, and reaches a peak at the second row, but decreases at the third and fourth rows. Heat transfer is the highest when Re is 7,000.

Heat transfer in Figure 6.51 increases at the low value at the first row and reaches a peak at the second row. It then decreases at the third and fourth rows. The first row is the highest when Re is 9,000.

Figure 6.52 shows that heat transfer at $Re = 9,000$ and $11,000$ decreases from the highest value at the first row, increases at the third row, and then decreases at the fourth row. At $Re = 5,000$ and $6,000$, heat transfer increases from the low value at the first row and then reaches a peak at the third row for $Re = 5,000$ and the fourth row for $Re = 6,000$.

Heat transfer in Figure 6.53 increases from the low value at the first row and reaches a peak at the third row. When $Re = 5000$, the first row is the highest. In Figure 6.54, the heat

transfer for $Re = 5,000$ and $6,000$ starts to decrease from the high value at the first row to the fourth row, but the heat transfer for $Re = 9,000$ and $11,000$ starts to increase from the first row and reach a peak at the second row.

Figure 6.55 shows the heat transfer as it decreases from the high value at the first row and later increases at the fourth row. Both Figures 6.56 and 6.57 show the heat transfer as it decreases from the high value at the first row to a low value at the fourth row. Heat transfer in Figures 6.58 and 6.59 decreases at a high value at the first row, increases at the third row, and then decreases at the fourth row.

In Figure 6.60, heat transfer decreases at a high value at the first row, increases at the third row, and then decreases at the fourth row. In Figure 6.61, the heat transfer increases from a low value at the first row and decreases at the fourth row. Heat transfer at $Re = 11,000$ decreases at high value at the first row and then increases at the fourth row. Both Figures 6.62 and 6.63 explain the same results behavior as in Figure 6.61.

6.5 Effect of Number of Holes and Jet-to-Target Spacing

Tables 6.1, 6.2, and 6.3 show a comparison of area-averaged heat transfer enhancement for different jet-to-target spacing for 6-, 24-, and 54-hole jet-issuing and target plates. The tables reveal a whole picture of heat transfer performance regarding the effect of the jet-to-target spacing and number of holes. As for the target plate, the 54-hole plates have the best heat transfer at $H/D_j = 6$ and 8 , followed by the 24-hole plates at $H/D_j = 2.67$, then 6 holes at 2.67 .

Table 6.1 Comparison of Different Jet-to-Target Spacing for 6-Hole Jet and Target Plate

		Jet-issuing plate			Target plate		
Rem	Re	H/Dj=1.33	H/Dj=2	H/Dj=2.67	H/Dj=1.33	H/Dj=2	H/Dj=2.67
16000	14000	0.95	1.09	1.28	1.77	1.91	2.61
20000	18000	0.87	1.05	1.23	1.64	1.88	2.30
30000	27000	0.76	0.99	1.17	1.44	1.84	1.88
37000	33000	0.71	0.97	1.14	1.35	1.82	1.71

Table 6.2 Comparison of Different Jet-to-Target Spacing for 24-Hole Jet and Target

		Jet-issuing plate			Target plate		
Rem	Re	H/Dj=2.67	H/Dj=4	H/Dj=5.33	H/Dj=2.67	H/Dj=4	H/Dj=5.33
16000	7000	1.23	1.49	1.44	4.61	3.40	3.66
20000	9000	1.14	1.40	1.45	4.55	3.64	3.80
30000	14000	1.02	1.26	1.46	4.45	4.07	4.03
37000	17000	0.97	1.20	1.47	4.40	4.29	4.14

Table 6.3 Comparison of Different Jet-to-Target Spacing for 54-Holes Jet and Target

		Jet-issuing plate			Target plate		
Rem	Re	H/Dj=4	H/Dj=6	H/Dj=8	H/Dj=4	H/Dj=6	H/Dj=8
16000	5000	2.21	2.12	2.71	2.76	4.74	5.38
20000	6000	2.02	1.91	2.45	2.57	4.78	5.22
30000	9000	1.74	1.63	2.08	2.29	4.84	4.99
37000	11000	1.62	1.51	1.92	2.17	4.88	4.88

The highest value of the overall-averaged heat transfer of the 6-hole jet and target plate occurs at $H/Dj = 2.67$ and at $Re = 14,000$. This shows that the cross-flow becomes more developed and has its strongest effect on the impinging jet interactions at large

jet-to-target plate spacing. The cross-flow is high at small jet-to-target plate spacing, which may affect the jet from creating more circulation and interaction (see Table 6.1).

In Table 6.2, the highest value overall-averaged heat transfer for the 24-hole target plate occurs at $Re = 17,000$ and $H/D_j = 2.67$. This reveals that the cross-flow is strong and has a significant effect on jets at a high Reynolds number, which increases the heat transfer due to the interaction between the jets. However, the cross-flow for the 24-hole jet-issuing plate at $Re = 7,000$ and $H/D_j = 5.33$ is well developed and causes more heat enhancement around the stagnation regions of the jets.

Table 6.3 shows that the highest heat transfer appears at $Re = 5,000$ and $H/D_j = 8$ for both the 54-hole jet-issuing and target plates. Thus, the interaction and circulation between the jets is increasing due to the small jet-to-jet spacing and the strong cross-flow.

The results show a significant dependency on the jet-to-target spacing. The heat transfer decreases for a small jet-to-target plate due to strong cross-flow that is not yet developed enough to enhance the heat transfer. Accordingly, the upstream region experiences low heat transfer and may prevent circulation and the interaction between the jets while further downstream, where the jets are pushed away from the target surface. Therefore the jet impingement is reduced, thus decreasing the heat transfer underneath the jets.

The number of holes has a significant effect on the overall-averaged heat transfer on both the jet-issuing and target plates. The order of the highest value heat transfer results for all three test sections starts from 54 holes, then 24 holes, and finally, 6 holes. But jet-to-target plate spacing also has a significant effect at $H/D_j = 2.67$, where the values of the overall heat transfer for 24 holes is higher than those of 54 holes in the target plate.

At the same total flow rate of jets for all three test sections, the number of the holes increases as spaces between the jets decrease. Accordingly, the interaction and circulation between the small jet-to-jet spacing and around the stagnation regions becomes more affected by the cross-flow, thus increasing the overall heat transfer.

Results also show that the overall-averaged heat transfer of the target plates in each test section is higher than those of the jet-issuing plates at the same jet-to-jet target spacing. The highest overall-averaged heat transfer values in the jet-issuing plates is in the 54-hole plates and at $H/D_j = 8$. The lowest values is in the 6-hole plates and at $H/D_j = 1.33$. Tables 6.4-6.6 show the correlation equations obtained from the results by using a least-square curve fitting.

Table 6.4 *Correlation Equations for 6-Hole Jet and Target Plates*

H/D _j	Target plate	Jet plate	Re
1.33	$Nu = 0.66 Re^{0.491}$	$Nu = 0.25 Re^{0.467}$	
2	$Nu = 0.029 Re^{0.742}$	$Nu = 0.035 Re^{0.666}$	$14000 \leq Re \leq 33000$
2.67	$Nu = 1.9 Re^{0.316}$	$Nu = 0.033 Re^{0.667}$	

Table 6.5 *Correlation Equations for 24-Hole Jet and Target Plates*

H/Dj	Target plate	Jet plate	Re
2.67	$Nu = 0.046 Re^{0.748}$	$Nu = 0.087 Re^{0.526}$	
4	$Nu = 0.002 Re^{1.06}$	$Nu = 0.068 Re^{0.552}$	$7000 \leq Re \leq 17000$
5.33	$Nu = 0.045 Re^{0.938}$	$Nu = 0.005 Re^{0.818}$	

Table 6.6 *Correlation Equations for 54-Hole Jet and Target Plates*

H/Dj	Target plate	Jet plate	Re
4	$Nu = 0.122 Re^{0.529}$	$Nu = 0.189 Re^{0.451}$	
6	$Nu = 0.0132 Re^{0.833}$	$Nu = 0.188 Re^{0.421}$	$5000 \leq Re \leq 11000$
8	$Nu = 0.041 Re^{0.690}$	$Nu = 0.218 Re^{0.410}$	

7.0 CONCLUSION AND RECOMMENDATIONS

7.1 Summary of Thesis Research

The present research was designed to examine the effect of the size of jet, number of jets, and jet-to-target plate spacing for a jet-issuing plate and target plate in the presence of cross-flow originating from the upstream jets on the heat transfer distribution of the jet and target plates. Two-dimensional inline arrays of circular jets of air impinging on a heat transfer surface paralleled to the jet-issuing plate were considered. The air, after impingement, was constrained to exit in a single direction along a channel formed by the target plate and the jet-issuing plate. The downstream jets were subjected to a cross-flow from the upstream jets. The heat transfer measurement used a liquid crystal imaging technique with a one-dimensional transient conduction model. TLC technique was chosen as a base experimental tool. This is because it provides full coverage of detailed local heat transfer phenomenon and its potential to be applied on a complicated surface.

The general conclusions of this research accomplished are outlined below:

1. Detailed local heat transfer on two principal walls, target plate, and jet-issuing plates affected by an array of impinging jets was examined.
2. The measurement system was verified. By comparing against well-known data sets of heat transfer measurement for a simplified model, a 42-hole target plate, the discrepancy from the current measurement system has been found to be no more than 18%.

3. The local heat transfer coefficient on the target plate shows strong spatial variation and evidence of opposing effects between jet-induced turbulent mixing and cross-flow issued from upstream jets.

4. Local heat transfer on the jet-issuing plate shows much less nonuniformity, and the magnitudes of the heat transfer coefficient are much less than those on a corresponding target plate by a factor of approximately 1.9-2 for 6 holes, 2.3-4.5 for 24 holes, and 2-3.2 for 54 holes at the same jet-to-target spacing.

5. The area-averaged heat transfer coefficient over the entire target plate for the 24-hole case is 1.5-2.5 times higher than that of the 6-hole case at $Re = 14,000$.

6. The area averaged heat transfer coefficient over the entire target plate for the 54-hole case is 1.2-1.3 times higher than that of the 24-hole case at $Re = 9,000$, but the area-averaged heat transfer coefficient for the 24-hole target plate is 2 times higher than that of the 54-hole case at $Re = 9,000$ and $H/D_j = 2.67$.

7. The area-averaged heat transfer coefficient over the entire target plate for the 54-hole case is approximately 2.2-5.4 times higher than the value of a fully developed turbulent flow in channel, the 24-hole target case is 3.4-4.6 times higher than the value of a fully developed turbulent flow in channel, and the 6-hole target plate case is 1.3-2.6 times higher than the value of a fully developed turbulent flow in channel.

8. The area-averaged heat transfer coefficient over the entire jet-issuing plate for the 54-hole case is approximately 1.5-2.7 times higher than the values of a fully developed turbulent flow in channel, the 24-hole jet-issuing plate case is 1-1.5 times higher than the values of a fully developed turbulent flow in channel, and the 6-hole

jet-issuing plate case is 0.7-1.7 times higher than the values of fully developed turbulent flow in channel.

9. An optimum distance for jet-to-target plate spacing was found to be $H/D_j = 2.67$ for the jet-issuing and target plate for the 6-hole case. The 24-hole case is $H/D_j = 2.67$ for the target plate and $H/D_j = 5.33$ for jet-issuing plate. The 54-hole case is $H/D_j = 8$ for the jet-issuing and target plate.

10. Local heat transfer on the target plate shows much more uniformity at small jet-to-target spacing than large jet-to-target spacing.

7.2 Future Recommendations

The following suggestions are highly recommended for future study in this area.

1. Evaluation of heat transfer coefficient based on the local bulk temperature. The reference temperature used to deduce the heat transfer coefficient in the current study was the linear interpolation of the inlet temperature. This is acceptable only if the length of the test section is short and the temperature difference between the inlet and outlet is small. However, heat transfer coefficient based on the local bulk flow temperature is still desirable and more meaningful to the designers. Chyu, et al. (1997) demonstrated a numerical operation to convert the heat transfer coefficient based on the inlet temperature into the heat transfer coefficient based on the local bulk flow temperature for a long straight cooling channel roughened with vortex generators. This method is established on the principle of energy conservation and provides a very convenient means to bridge the

heat transfer coefficients based on the two different temperatures. This method is expected to provide more meaningful results.

2. In order to reach a uniform cooling effect in the complete length of the cooling section, other parameters in the design should be considered in future work. For example, increasing the number of holes and decreasing jet-to-jet spacing could be considered, therefore eliminating the low thermal effect between the jet impingements and creating more enhancement of the heat transfer between the jets. Varying the hole size along an inline array from upstream to downstream of the jet-issuing plate enhances the heat transfer on the downstream region by maximizing the hole size of the downstream jet-issuing plate and minimizing the hole size of the upstream jet-issuing plate.

3. Another design is also recommended by the U.S. Patent and Trademark (U.S. Patent No. 5,388,412) Department in which the impingement surface thickness is decreased linearly in the downstream flow direction, therefore, the cross-flow will be more developed on the downstream region and will enhance the heat transfer on this region.

BIBLIOGRAPHY

BIBLIOGRAPHY

- Baugh, J. W., Ireland, P. T., Jones, T. V., & Saniei, N. (1989). A comparison on the transient and heated-coating methods for the measurement of local heat transfer coefficients on a pin fin. *Journal of Heat Transfer*, 111, 877-881.
- Bunker, R. and Metzger, D. (1990). Local heat transfer in internally cooled turbine airfoil leading edge regions: Part I – Impingement cooling without film coolant extraction. *Journal of Turbomachinery*, 112, 451-458.
- Camci, C., Kim, K., & Hippensteele, S. A. (1992). A new hue capturing technique for the quantitative interpretation of liquid crystal images used in convective heat transfer studies. *ASME Journal of Turbomachinery*, 114, 765-775.
- Camci, C., Kim, K., Hippensteele, S. A., & Poinsatte, P. E. (1993). Evaluation of a hue capturing based transient liquid crystal method for high-resolution mapping of convective heat transfer on curved surface. *Journal of Heat Transfer*, 115, 311-318.
- Chupp, R., Helms, H., McFadden, P., & Brown, T. (1969). Evaluation of internal heat-transfer coefficients for impingement-cooled turbine airfoils. *Journal of Aircraft*, 6(3), 203-208.
- Chyu, M. K., & Ding, H. (1997). Heat transfer in a cooling channel with vortex generators, heat transfer gallery. *Journal of Heat Transfer*, 119, 206.
- Chyu, M. K., Ding, H., Downs, J. P., Van Sutendael, M. & Soechting, F. O. (1997). *Determination of local heat transfer coefficient based on bulk mean temperature using a transient liquid crystals techniques*. ASME paper 97-GT-489.
- Chyu, M. K., Yen, C. H., Ma, W., & Shih, T. I-P. (1999). *Effects of flow gap atop pin elements on the heat transfer from pin fin arrays*. Submitted to ASME TurboExpo 1999, Indianapolis, Indiana.
- Cooper T. E., Field, R. J., & Meyer, J. F. (1975). Liquid crystal thermography and its application to the study of convective heat transfer. *ASME Journal of Heat Transfer*, 97, 442-450

- Critoph, R. E., & Fisher, M. (1998). A study of local heat transfer coefficients in plate fin-tube heat exchangers using the steady state and transient liquid crystal techniques. *IMECHE Conference Transactions*, 2, 201-210.
- Den Ouden, C., & Hoogendorn, C. J. (1974). Local convective-heat transfer coefficients for jets impinging on a plate-experiments using a liquid crystal technique. *Proceedings of the Fifth International Heat Transfer Conference*, 5, New York: AICHE, 293-297.
- Dixon, G. D. (1977). Cholesteric liquid crystals in nondestructive testing. *Material Evaluation*, 35(6), 51-55.
- Downs, S. J., & James, E. H. (1987, October). *Jet impingement heat transfer: A literature survey*. Paper 87-HT-35, National Heat Transfer Conference, Pittsburgh, Pennsylvania, August 9-12, 1987.
- Ekkad, S. V., Gao, L., & Hebert, R. T. (2002). Effect of jet-to-jet spacing in impingement arrays on heat transfer. ASME Paper No. IMECE2002-32108, ASME International Mechanical Engineering Congress and Exposition, 2002, New Orleans, LA.
- Farina, D. J., Hacker, J. M., Moffat, R., & Eaton, J. K. (1994). Illuminant invariant calibration of thermochromic liquid crystals. *Experimental Thermal and Fluid Science*, 9, 1-12.
- Florschuetz, L., Berry, R., & Metzger, D. (1980). Periodic streamwise variations of heat transfer coefficients for inline and staggered arrays of circular jets with crossflow of spent air. *Journal of Heat Transfer*, 102, 132-137.
- Florschuetz, L., Truman, C., & Metzger, D. (1981). Streamwise flow and heat transfer distributions for jet array impingement with crossflow. *Journal of Heat Transfer*, 103, 337-342.
- Florschuetz, L., Metzger, D., & Su, C. (1984). Heat transfer characteristics for jet array impingement with initial crossflow. *Journal of Heat Transfer*, 106, 34-41.
- Gardon, R., and Akfirat, J. (1966, February). Heat transfer characteristics of impinging two-dimensional air jets. *Journal of Heat Transfer*, 101-108.
- Gardon, R., & Cobonpue, J. (1962). Heat transfer between a flat plate and jets of air impinging on it. *Proceedings of the 2nd International Heat Transfer Conference, International Developments in Heat Transfer*, New York: ASME, 454-460.
- Gillespie, D., Wang, Z., Ireland, P., & Kohler, S. (1996). Full surface local heat transfer coefficient measurements in a model of an integrally cast impingement cooling

- geometry. Paper No. 96-GT-200, IGTI Congress and Exhibition, Birmingham, UK.
- Hippensteele, S. A., Russell, L. M., & Stepka, F. S. (1983). Evaluation of a method for heat transfer measurements and thermal and thermal visualization using a composite of a heater element and liquid crystals. *Journal of Heat Transfer*, *105*, 184-189.
- Hippensteele, S. A., Russell, L. M., & Torres, F. J. (1985). Local heat transfer measurements on a large scale-model turbine blade airfoil using a composite of a heater element and liquid crystals. *ASME Journal of Gas Turbines and Power*, *107*, 953-960.
- Huang, Y., Ekkad, S., & Han, J-C. (1996, November). *Detailed heat transfer coefficient distributions under an array of impinging jets with coolant extraction*. Paper presented at the 1996 International Mechanical Engineering Conference and Exposition, Atlanta, GA.
- Huber, A. M., & Viskanta, R. (1994). Effect of jet-jet spacing on convective heat transfer to confined, impinging arrays of axisymmetric air jets. *International Journal of Heat Mass*, *37*, 2859-2869.
- Ichimiya, K. (1995). Heat transfer and flow characteristics of an oblique turbulent impinging jet within confined walls. *Journal of Heat Transfer*, *117*, 316-322.
- Ireland, P. T., & Jones, T. V. (1985). The measurement of local heat transfer coefficient in blade cooling geometries. Paper No. 28 presented at the AGARD Conference on Heat Transfer and Cooling in Gas Turbine, CP 390, Bergen.
- Ireland, P. T., & Jones, T. V. (1987). The response time of a surface thermometer employing encapsulated thermochromic liquid crystals. *Journal of Physics Scientific Instruments*, *20*, 1195-1199.
- Kercher, D., & Tabakoff, W. (1970). Heat transfer by a square array of round air jets impinging perpendicular to a flat surface including the effect of spent air. *Journal of Engineering for Power*, *92*, 73-82.
- Kline, S., & McClintock, F. A. (1953). Describing uncertainties in single sample experiments. *Mechanical Engineering*, *75*(1), 3-8.
- Lin, Z., Chou, Y., & Huang, Y. (1997). Heat transfer behaviors of a confined slot jet impingement. *International Journal of Heat and Mass Transfer*, *40*, 1095-1107.
- Matsumoto, R., Kikkawa, S., & Senda, M. (1997). Effect of Pin Fin Arrangement on Endwall Heat Transfer. *JSME International Journal, Ser. B*, *40*(1), 142-151.

- Metzger, D., Baltzer, R., & Jenkins, C. (1972). Impingement cooling performance in gas turbine airfoils including effects of leading edge sharpness. *Journal of Engineering for Power*, 92, 219-225.
- Metzger, D., & Bunker, R. (1990). Local heat transfer in internally cooled turbine airfoil leading edge regions: Part II- Impingement cooling with film coolant extraction. *Journal of Turbomachinery*, 112, 459-466.
- Metzger, D., & Korstad, R. (1972). Effects of crossflow on impingement heat transfer. *Journal of Engineering for Power*, 94, 35-41.
- Metzger, D. E., & Larson, D. E. (1986). Use of melting point surface coatings for local convection heat transfer measurements in rectangular channel flows with 90-deg turns. *Journal of Heat Transfer*, 108, 48-54.
- Moffat, R. J. (1982). Contributions to the theory of single-sample uncertainty analysis. *Journal Fluids Engineering*, 104, 250-260.
- Ozisik, M. N. (1980). *Heat conduction*. New York: Wiley.
- Simonich, J. C., & Moffat, R. J. (1984). Liquid crystal visualization of surface heat transfer on a concavely curved turbulent boundary layer. *ASME Journal of Engineering for Gas Turbines and Power*, 106, 619-627.
- Tabakoff, W., & Clevenger, W. (1972). Gas turbine blade heat transfer augmentation by impingement of air jets having various configurations. *Journal of Engineering for Power*, 92, 51-60.
- Taslim, M. E., Li, T., & Spring, S. D. (1995). Experimental study of the effects of bleed holes on heat transfer and pressure drop in trapezoidal passages with tapered turbulators. *Journal of Turbomachinery*, 117, 281-289.
- Taslim, M. E., Li, T., & Spring, S. D. (1998). Measurements of heat transfer coefficients in rib-roughened trailing-edge cavities with crossover jets. Paper no. 98-GT-435 presented at the ASME TurboExpo, Stockholm Sweden.
- Vejrazka, J. (2002). *Experimental study of pulsating round impinging jet*. Unpublished doctoral dissertation, Institute of Chemical Process Fundamentals, Prague, Czech Republic.
- Valencia, A., Fiebig, M., & Mitra, N. K. (1995). Influence of heat conduction on determination of heat transfer coefficient by liquid crystal thermography. *Experimental Heat Transfer*, 8, 271-279.

- Van Treuren, K., Wang, Z., Ireland, P., & Jones, T. (1995). Detailed measurements of local heat transfer coefficient and adiabatic wall temperature beneath an array of impinging jets. *Journal of Turbomachinery*, 116, 369-374.
- Van Treuren, K., Wang, Z., Ireland, P., Jones, T., & Kohlers, S. (1996). *Comparison and prediction of local and average heat transfer coefficients under an array of inline and staggered impinging jets*. Paper No. 96-GT-163, IGTI Congress and Exhibition, Birmingham, UK.
- Vedula, J. R., & Metzger, D. (1991). *A method of simultaneous determination of local effectiveness and heat transfer distributions in three temperature convection situations*. ASME Paper no. 91-GT-345 presented at the ASME TurboExpo, Orlando, Florida.
- Vennemann, D., & Butefisch, K. A. (1973). *The application of temperature-sensitive crystals to aerodynamic investigations*. Deutsch Luft Raumfahrt Forschungsber, Article no. DLR-FB-73-121. Geottingen, Germany: Institut fuer Dyn Verduennter Gase.
- Viskanta, R.. (1993). Heat transfer for impinging isothermal gas and flame jets. *Experimental Thermal and Fluid Science*, 6(1), 113-134.
- Wang, Z., Ireland, P. T., & Jones, T. V. (1995). An advanced method of processing liquid crystal video signals from transient heat transfer experiments. *Journal of Turbomachinery*, 117, 184-189.
- Wang, Z., Ireland, P.T., Jones, T. V., & Davenport, R. (1996). A color image processing system from transient liquid crystal heat transfer experiments. *Journal of Turbomachinery*, 118, 421-427.
- Yu, Y., & Chyu, M. K. (1996). *Influence of leaking gap downstream of the injection holes on film cooling performance*. ASME Paper no. 96-GT-175 presented at the ASME TurboExpo, Birmingham, England.